DISPROPORTIONATION OF POLYSULFIDES FACILITATED BY A BI-FUNCTIONAL CARBON HOST IN LI-S BATTERIES

by

Dantong Qiu

A Dissertation Submitted in

Partial Fulfillment of the

Requirements for the Degree of

Doctor of Philosophy

in Engineering

at

The University of Wisconsin-Milwaukee

August 2024

ABSTRACT

DISPROPORTIONATION OF POLYSULFIDES FACILITATED BY A BI-FUNCTIONAL CARBON HOST IN LI-S BATTERIES

By

Dantong Qiu

The University of Wisconsin-Milwaukee, 2024
Under the Supervision of Professor Deyang Qu

Lithium-sulfur (Li-S) batteries are regarded as one of the promising alternatives to conventional lithium-ion batteries (LIBs) due to their high theoretical energy density (2600 Wh kg^{-1}), abundant resources on Earth, and low cost of sulfur. Nevertheless, several significant challenges persist in the practical application of Li-S batteries, including the insulating nature of sulfur, volume changes of cathodes, and, most critically, the shuttle effect of dissolved long-chain lithium polysulfide (PS) species during cycling. In this thesis, a novel carbon host for sulfur cathode, derived from natural silk and denoted as NC, was developed. This carbon host possesses excellent cycling performance because of its hierarchical porous structure and nitrogen-contained functional groups. In addition, it demonstrated the ability to facilitate the disproportionation reactions of PS, converting PS ions into solid products of elemental sulfur (S_8) and probably lithium disulfide (Li_2S_2). This reduces the residence time of PS ions in the electrolyte. Consequently, Li-S cells with S/NC cathodes display enhanced electrochemical performance in both coin cells and pouch cells, even with high sulfur loading and lean electrolytes.

TABLE OF CONTENTS

LIST OF FIGURES

LIST OF TABLES

LIST OF ABBREVIATIONS

BET	Brunauer-Emmett-Teller
BJH	Barrett-Joyner-Halenda
CE	Coulombic Efficiency
CV	Cyclic Voltammetry
CS_2	Carbon Disulfide
CNTs	Carbon Nanotubes
DME	1,2-dimethoxyethane
DoC	Depth of Charge
DoD	Depth of Discharge
DOL	1,3-dioxolane
EDS	Energy Dispersive X-ray Spectroscopy
E/S	Electrolyte/ Sulfur
ESI-MS	Electrospray Ionization-Mass Spectroscopy
EIS	Electrochemical Impedance Spectroscopy
FESEM	Field Emission Scanning Electron Microscope
HPLC	High-performance Liquid Chromatograph
KB	Ketjenblack

LIB	Lithium-ion Battery
Li-S	Lithium-Sulfur
LiTFSI	Lithium bis(trifluoromethane)sulfonimide
LiPS	Lithium Polysulfides
NC	Nitrogen-doped Carbon Derived from Silk
NMP	N-methyl-2-pyrrolidone
PVDF	Polyvinylidene Fluoride
PS	Polysulfides
SEI	Solid Electrolyte Interphase
SPAN	Sulfurized Polyacrylonitrile
TGA	Thermogravimetric Analysis
UV-Vis	Ultraviolet-Visible
XPS	X-ray Photoelectron Spectroscopy
XRD	X-ray Diffraction

ACKNOWLEDGEMENTS

I would like to express my deepest gratitude to everyone who supported and guided me throughout the completion of this dissertation.

Firstly, I am deeply indebted to my supervisor, Professor Deyang Qu, for his continuous support, patience, and invaluable guidance. His expertise and insights in electrochemistry and battery were crucial to the success of this research. Without his guidance and persistent help this dissertation would not have been possible.

I would also extend my thanks to my committee members, Professor Brian S R Armstrong, Professor Ilya Avdeev, Professor Shama P Mirza, Professor Yin Wang, and Professor Woo Jin Chang for their time, valuable comments, and suggestions on my work.

I would also like to express my appreciation to Dr. Dong Zheng for helping me address the problems I encountered in my experiments and for always offering valuable suggestions. Special thanks to Dr. Xiaoxiao Zhang, a colleague and friend, for her support and willingness to share valuable experiences in both research and life.

My heartfelt thanks go to my colleagues and peers: Dr. Huainan Qu, Dr. Weixiao Ji, Dr. Tianyao Ding, Miao Liu, Dr. Jingyu Si, Caleb Abegglen, Telemachos Agoudemos, Owen James Schneider, Dr. Peng Chen, Dr. Yang Qin, Joshua Estell, Dr. Kalpana Murugesan, Soad Shajid, and Maliha Majumder for their help, advice, and encouragement.

Finally, I would like to express my gratitude to my family and friends for their unwavering support and encouragement, in particular, my mother Jun Yang and my father Xinping Qiu. Their endless love and belief in me have always been my greatest source of strength in overcoming any difficulties and challenges in my life.

CHAPTER 1. BACKGROUND INTRODUCTION

1.1 Development of Lithium-Ion Batteries

Over the past few centuries, mainly since the Industrial Revolution, fossil fuels have been the primary source of storable energy, driving both technological and social development. However, these fossil fuels are finite, and with the rapid expansion of the population and increasing energy demands in daily life, they are facing significant depletion. Furthermore, the extensive use of fossil fuels has led to environmental pollution, including the increased emission of greenhouse gases, responsible for the Earth's rising average surface air temperature.[1] Consequently, renewable energy sources such as solar and wind have been widely adopted to replace traditional fossil fuels and alleviate the above issues. Batteries have been developed as energy storage devices to store this continuously produced renewable energy. Rechargeable batteries, known as secondary batteries, have also become more and more significant in the transportation sector, as they are increasingly used to power vehicles instead of gasoline. Additionally, with the development of portable electric devices, such as cell phones and laptops, these secondary batteries with longer service life have become indispensable daily.

A *battery* is a device that stores energy released from chemical reactions as chemical energy and converts it into electrical energy to power electronic devices. Batteries consist of two electrodes—the cathode and anode—along with an electrolyte facilitating ion transport and a porous separator preventing direct contact between the electrodes. During discharge, electrons flow from the anode to the cathode through an external circuit. At the same time, cations move from the anode to the cathode within the battery through the electrolyte, balancing the electron flow. The reverse process occurs during charging.

The lead-acid battery, which was the first type of rechargeable battery, was invented in 1859 by the French scientist Gaston Plantè.[2] Even today, lead-acid batteries are critical in various applications, such as automobile ignition and backup power systems.[2] Since then, various rechargeable batteries have evolved alongside technological progress and the growing demand for batteries with longer lifespans, smaller sizes, and higher safety standards.[3] Lithium-ion batteries (LIBs) have attracted significant attention due to their high energy-to-weight ratio and long operational life. The lowest atomic weight and the lowest electrochemical potential of lithium among all the metals endow it with a high operating voltage, low weight, and high energy-storage density.[4,5] LIBs were proposed and developed in the 1970s, with the first rechargeable Li-ion battery proposed by Stanley Whittingham in 1976, using TiS_2 and metallic lithium as the cathode and anode, respectively.[6,7] In the early 1980s, $LiCoO_2$ and carbon-based material such as graphite were reported as the cathode and anode materials in Li-ion batteries, offering higher energy density and improved safety.[8,9] Later, in the 1990s, Sony successfully launched commercial LIBs, marking a significant milestone in the battery industry.[10] Over the following two decades, various materials, such as $LiFePO_4$, $LiNi_xMn_yCo_{1-x-y}O_2$ (NMC), silicon, and silicon/graphite composites, have been explored as cathode and anode materials to improve the overall performance of LIBs continuously.[11–13]

LIBs are working based on the reversible intercalation reactions of lithium ions into the layered structures of compounds. Initially, the cell is fully discharged, with lithium ions intercalated within the cathode and tied with electrons. The working principle is depicted in Figure 1-1. During the charging process, oxidation reactions occur at the cathode, releasing electrons into the external circuit. To maintain the charge balance within the cathode, lithium ions are simultaneously released to the electrolyte and insert into the graphitic sheets of

anodes.[14–16] When the cell is discharging, the reverse reactions take place: lithium ions will de-intercalate from the anode and reinsert to the cathode. Thus, LIBs efficiently convert the change in free energy, caused by the migration of lithium ions between the two electrodes, into electrical energy, thereby powering the electric devices.[16]

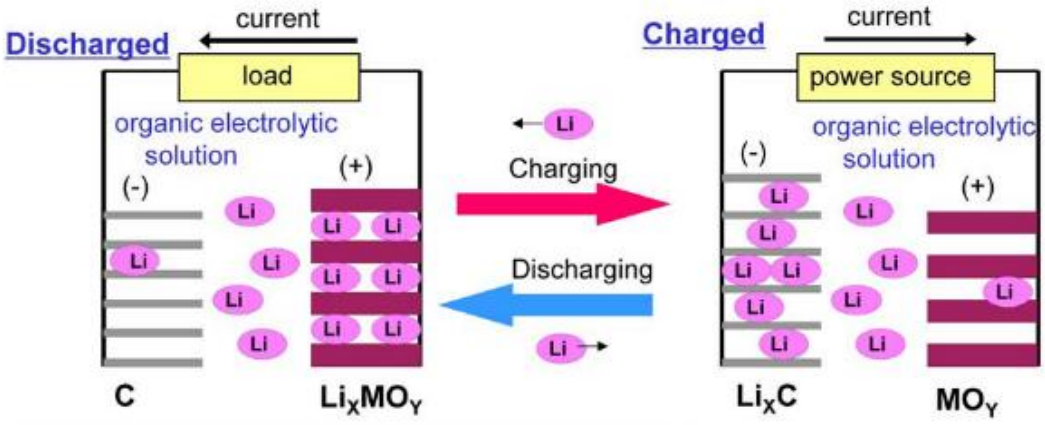

Figure 1- 1. Principle of Li-ion batteries.[15]

Although LIBs continue to dominate the commercial batteries market in decades, their energy density is gradually approaching the theoretical limit and they still fall short of meeting the high energy density demands of society, especially for electric vehicles. In the search for alternatives, lithium-sulfur (Li-S) batteries have been considered as one of the competitive candidates.

1.2 Lithium-Sulfur Batteries

1.2.1 Development and Working Principles

Li-S batteries were first proposed in the early 1960s.[17] However, their development has lagged behind LIBs over the past decades due to challenges such as low practical discharge capacity and rapid capacity decay.[18] However, as the demand for batteries with higher energy densities increases, Li-S batteries started to regain the attractions because of their high theoretical capacity. When used as the cathode material, sulfur offers a remarkable theoretical specific capacity of 1675 mAh g^{-1} and a theoretical energy density of 2600 Wh kg^{-1}, which is the highest among solid elements.[18] This high capacity, combined with the lightweight of sulfur, contributes to the significantly higher energy density of Li-S batteries. The use of metallic lithium as the anode material further enhances the theoretical energy density of the battery. At the cell level, Li-S batteries can achieve a gravimetric energy density of 400-600 Wh kg^{-1}, substantially higher than the 250 Wh kg^{-1} typical of conventional LIBs.[19,20] Therefore, an electric vehicle with fully developed Li-S batteries could achieve a driving range over 650 km on a single charge, using less amount of batteries compared to those that use LIBs as power source. Furthermore, sulfur cathodes offer lower manufacturing costs than current cathodes of commercial LIBs, which rely on expensive transition metals like cobalt, due to sulfur's abundant resources and low cost.

Cyclic octasulfur (S_8) is the most stable form of sulfur among all its solid allotropes in nature.[21] Traditional Li-S batteries consist of sulfur as the cathode, metallic lithium as the anode, separator in between to keep them apart but allow Li ions passing through, and organic electrolyte. The batteries work based on the redox reactions between lithium and cyclo-S_8. Since sulfur is in the charged state, the battery needs to be discharged first after assembly.[22] A typical charge/discharge curve of the Li-S battery is displayed in Figure 1-2, features two distinct discharge plateaus, which corresponding to two phase-transitions: first from solid to liquid, and subsequently back to solid. These multistep redox reactions contribute to the high theoretical specific capacity of Li-S batteries.[23] During discharge, the lithium anode undergoes oxidation, releasing electrons to form lithium ions, which then move to the cathode side through electrolyte. While at the cathode, sulfur accepts electrons from the external circuit and reacts with lithium ion. The sulfur will first be reduced to Li_2S_8 and then Li_2S_n ($3 \leq n \leq 8$), which corresponding to the region I and II in the plot.[21] These intermediates, known as high-order or long-chain lithium polysulfides (PS), are soluble in the ether-based electrolyte used in Li-S batteries, and therefore, the first discharge plateau at 2.3 V (vs Li/Li^+) corresponds to the transition from solid (S_8) to liquid (Li_2S_n, $3 \leq n \leq 8$).[24] This process contributes around 25% of the theoretical specific capacity, which is 418 mAh g^{-1} of sulfur cathode. [25] The high-order PS are further reduced to Li_2S_2/Li_2S and finally to Li_2S, corresponding to regions III and IV in the charge/discharge profile.[21] This process is represented by the second plateau at 2.1 V (vs Li/Li^+), reflecting the phase transition from liquid to solid, as the final discharge products are insoluble in the ether-based electrolyte.[24] As displayed in Figure 1-2, the lower plateau contributes to the remaining theoretical capacity of 1255 mAh g^{-1}. The multi-electron-transfer reactions of the sulfur cathodes

give Li-S batteries a high theoretical capacity. The reactions that occur during discharging are[25,26]:

$$\text{Anode: } 16\text{Li} \rightarrow 16\text{Li}^{+} + 16\text{e}^{-1}$$

$$\text{Cathode: } \text{S}_8 + 16\text{Li}^{+} + 16\text{e}^{-} \rightarrow 8\text{Li}_2\text{S}$$

During the charging process, the reactions occur in reverse. Li_2S deposited on the cathode side releases lithium ions and is oxidized back to Li_2S_2 and high-order lithium polysulfides, eventually converting back to S_8.[18] These reactions at both positive and negative electrodes can be described by the following equations:

$$\text{Anode: } 16\text{Li}^{+} + 16\text{e}^{-1} \rightarrow 16\text{Li}$$

$$\text{Cathode: } 8\text{Li}_2\text{S} \rightarrow \text{S}_8 + 16\text{Li}^{+} + 16\text{e}^{-}$$

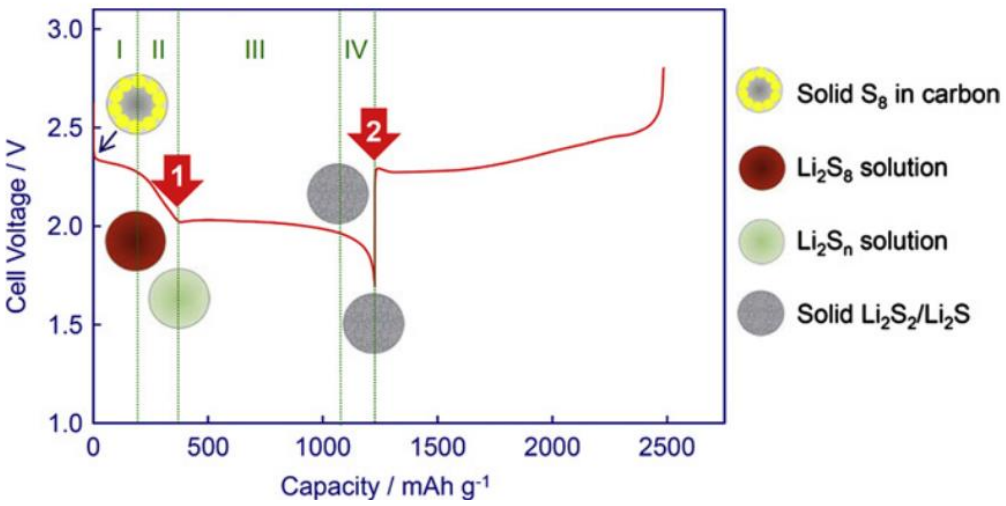

Figure 1- 2. Typical charge/discharge curve of Li-S batteries.[21]

Conventional Li-S batteries consist of a sulfur cathode, a metallic lithium anode, a porous separator, and organic electrolytes. While carbonate-based electrolytes are widely used in current commercial Li-ion batteries because of their high ionic conductivity, wide electrochemical window, and high volatilization temperature, they are not suitable for Li-S batteries.[27] This is because sulfur cathodes are chemically incompatible with carbonate solvent.[27] In Li-S battery systems, electrochemically active PS species act as nucleophile, while the carbonate solvents are electrophilic.[28] As a result, an irreversible nucleophilic-electrophilic substitution reaction occurs, leading to the battery failure during the very first discharge. [29] To ensure proper cycling performance in batteries, ether-based electrolytes are used in Li-S batteries because of their good compatibility with sulfur cathodes. 1,2-dimethoxyethane (DME) is characterized by its low viscosity and high dielectric constant, while 1,3-dioxolane (DOL) exhibits relatively low solubility for lithium polysulfides.[30] Owing to these advantages, both of these ether solvents are commonly chosen as electrolyte solvents in Li-S batteries, providing the necessary chemical environment for effective battery operation.

1.2.2 Challenges of Li-S Batteries

Despite the high energy density offered by Li-S batteries, their practical applications have yet to be realized because of several existing problems that lead to low delivered capacity and poor cycling stability. The first issue is the insulating nature of elemental sulfur and the discharge products, Li_2S_2/Li_2S.[25] S and Li_2S exhibit very low conductivities of 5×10^{-30} and 3.6×10^{-7} S cm^{-1}, respectively.[31] Additionally, they also display a low ionic conductivity, resulting in a slow transportation of lithium ion within the cathode. These high resistances severely hinder the efficient flow of electrons and ions in the sulfur cathodes, limiting the redox kinetics, leading to poor utilization of active material and reduced battery efficiency.[18,32] Moreover, the insoluble

and insulating Li_2S_2/Li_2S that precipitates on the surface of sulfur cathode and lithium anode forms an inert layer, increase the polarization of the cell, impeding further reduction of sulfur, and ultimately limiting the discharge capacity output.[33] To address these issues, conductive additives are introduced into the cathode composition. These additives help create a conductive network within the cathode, facilitating electron transfer and improving the overall performance of the battery.

Another major challenge that Li-S batteries are facing is the dissolution and shuttle of the intermediate discharge products, long-chain lithium PS, in the ether-based electrolyte during cycling, which is known as the shuttle effect. Although sulfur cathodes exhibit better stability and reversibility in ether-based electrolyte than in carbonate-based electrolyte, the dissolution of long-chain PS species in them is still a significant problem and cannot be overlooked. Due to the concentration gradient in the electrolyte, these highly soluble intermediates can pass through the separator and freely migrate between the cathode and anode.[26] Once they reach at the anode, part of the dissolved PS will be electrochemically and chemically reduced to insoluble Li_2S_2/Li_2S_2 because of the strong reducing property of metallic lithium.[21,34,35] They will precipitate on the lithium anode and cannot return to the sulfur cathodes. For those that have not been reduced, they will return to the cathode under the electric field force during the charging process.[31] In the long term, the shuttle effect leads to the loss of active material, corrosion of the lithium anode, and poor cycle life.[36] To reduce the influence of shuttle effect, lithium nitrate ($LiNO_3$) is commonly used as an additive in the electrolytes for Li-S batteries. Nitrate ions reduce on the surface of lithium anode, forming solid electrolyte interface (SEI), which is composed of Li_xNO_y and Li_xSO_y species.[23,37] This SEI layer protects lithium metal anode from reacting with long-chain lithium PS. However, the deep discharging of the batteries should be

avoided when $LiNO_3$ is included in the electrolyte. At lower potentials, $LiNO_3$ undergoes irreversible reduction at cathode followed by a reaction with electrolyte components and the precipitation of the reduction products on the cathode surface, resulting in a permanent slowdown in the cathode reaction kinetics.[38,39] In addition to using $LiNO_3$, other strategies to reduce the shuttle effect and enhance the cycling performance of Li-S batteries are being widely studied, such as optimizing the cathode design and improving the anode protection.

The third challenge facing Li-S batteries is the significant volume variation of sulfur cathodes during cycling. Sulfur cathodes can undergo up to 80% volume expansion and contraction during charging and discharging, primarily due to the density difference between S_8 (2.07 g cm^{-3}) and Li_2S (1.66 g cm^{-3}).[31,40] After repeated lithium deposition and dissolution process, the cathodes will be pulverized and gradually lose their electrical contacts with conductive substrates.[33] Over the long term, this can lead to the structural disintegration of sulfur cathodes, resulting in capacity decay. Furthermore, the failure of the cathodes may also pose safety risks to Li-S batteries.[33]

1.3 Sulfur Cathodes

Among the issues described above, the poor cycling stability of Li-S batteries can primarily be attributed to the dissolution of the intermediate long-chain lithium polysulfides and resulting side reactions. However, the dissolution of polysulfide species in the solvent is crucial for Li-S cells to achieve high specific capacity. Without it, the reduction of elemental sulfur would occur only at the interface of carbon and sulfur, leaving the bulk of sulfur inaccessible and resulting in low utilization of active material.[21] Cathodes are critical to the performance of Li-S batteries. Therefore, significant efforts have been devoted to exploring ways to reduce the

migration of these high-order lithium PS in the system to prevent the occurrence of harmful side reactions.[21]

1.3.1 Physical Entrapment of PS

Encapsulating sulfur within the conductive host materials is a widely adopted method to improve the overall electrochemical performance of Li-S batteries. These host materials provide more pathways for electron transfer and feature porous structures that can physically trap some of the PS species within the cathodes, and therefore mitigate the influence of shuttle effect. Carbon is one of the most widely used substrates for sulfur cathodes because of their excellent electrical conductivity, large specific surface area, and good mechanical stability.[41]

At first, carbon was merely utilized as a conductive additive in sulfur cathode by mixing it with sulfur to prepare the macro composite electrodes, which required the addition of a significant amount of carbon.[35] However, this approach results in a compromise, sacrificing the overall energy density. In 1989, Peled and colleagues proposed a more efficient method by loading sulfur into carbon host materials, forming a sulfur/carbon composite.[42] Since then, various carbon materials have been explored as substrates for sulfur cathodes. To maximize the utilization of active materials, it is essential to ensure good contact between sulfur and carbon. One of the most effective and commonly used methods for infusing sulfur into the carbon matrix is the "melt diffusion" technique. This simple and efficient process involves mixing sulfur powder with carbon materials and then heating the resulting mixture at 155 ºC. At this temperature, sulfur is in the liquid form and exhibits the lowest viscosity, which allows it to easily diffuse into the porous structures of the carbon matrix or adhere to its surface through capillary forces.[43] Another commonly used method to prepare the S/carbon composite is the

solution method, which involves dissolving sulfur in a solvent such as carbon disulfide (CS_2) and dimethyl sulfoxide (DMSO) and then infiltrating this solution into carbon.[21]

Carbon nanotubes (CNTs) have attracted significant attention in studying of Li-S batteries because of their high aspect ratio, outstanding mechanical durability, stable chemical properties, and high electrical conductivity.[44] As one-dimensional carbon materials, CNTs can form an interwoven conductive network within sulfur cathodes, facilitating electron transport and enhancing the cell's rate capability. CNTs were first applied in Li-S cells as merely conductive additives through simple mechanical mixing with active materials.[45] However, this approach often resulted in poor contact between sulfur and CNTs, leading to suboptimal discharge capacity. Then, researchers coated sulfur onto the outer surface of the CNTs through the capillary effect by heating the mixture of CNTs and sulfur at 155 ºC to enhance the contact between sulfur and CNTs.[46] This method enhanced the interaction between sulfur and CNTs, resulting in a cathode that delivered a reversible specific capacity of 670 mAh g^{-1} after 60 cycles, indicating a better cycle property than the cathode consisting of simple mixture of sulfur and CNTs. Xu and colleagues made further advancements, integrating porous spherical carbon (PSC) with CNTs to enhance the electrochemical performance of sulfur cathodes.[47] This combination synergistically mitigated the shuttle effect and reduced the electrical resistance of the cathode. The resulting PSC-CNT-S composite maintained a high reversible capacity of 700 mAh g^{-1} at a high current density of 2.8 mA cm^{-2} after 200 cycles, showcasing superior battery performance. Later, developments have seen CNTs more effectively utilized as host materials for sulfur cathodes, particularly in the flexible, self-supporting electrodes.[44] For example, a novel flexible electrode for Li-S batteries, S-CNT, was synthesized through a modified template-directed chemical vapor deposition utilizing a sulphate-containing AAO template.[46] The binder-free membrane electrode

was prepared employing an ethanol evaporation-induced assembly technique. Impressively, the cell exhibited stable cycling performance over 100 cycles, along with a significantly enhanced rate capability.

Graphene-based, two-dimensional carbon materials are also a category of carbon host widely used in Li-S batteries due to their superior conductivity and ease of functionalization.[25] Therefore, coating sulfur onto the surface of graphene or graphene oxide can significantly enhance the charge transfer kinetics within the electrode.[48,49] However, this method cannot suppress the transport of polysulfide species in the electrolyte during the cycling. The strategy of filling the porous graphene matrix with sulfur has been reported to solve this problem.[50] Li et al. synthesized a graphene oxide (rGO) coated thermally exfoliated graphene nanosheet-sulfur (TG-S) stack-up nanocomposite as the cathode material. During the cycling process, the stack-up TG and the rGO coating exhibit an excellent ability to encapsulate sulfur and confine the dissolved PS species. The resulting cell with the cathode reached a reversible capacity of 667 mAh g^{-1} after 200 cycles.

Carbon materials with appropriate porous structures are also well-suited for physically blocking the shuttle effect of PS species in Li-S batteries. These structures should be capable of encapsulating a high sulfur content while impeding the diffusion of the dissolved PS. Porous carbons, typically amorphous with a low degree of graphitization, feature a hierarchical porous structure composed of pores with varying sizes. Micropores have diameters smaller than 2 nm, mesopores range between 2 nm and 50 nm, and macropores have diameters larger than 50.[32] The physical confinement is a mechanism employed by porous carbon effectively mitigates the diffusion of long-chain PS, typically larger than 0.8 nm in diameter.[51] Therefore, the high specific surface areas and high conductivity make porous carbons ideal candidates for host

materials. Specifically, carbons with micropores and mesopores are preferable for their more effective mitigation of the shuttle effect. Wang et al. first reported a sulfur-coated mesoporous carbon composite as cathode materials for sulfur cathodes.[52] The mesoporous carbon demonstrated strong adsorption capabilities for dissolved PS species in electrolytes, resulting in much-improved capacity and cycling stability compared to pure sulfur cathodes. Due to its high specific surface areas and large pore volumes, the highly ordered mesoporous carbon CMK-3 has been regarded as an appropriate host material for sulfur cathodes. The mesoporous structure of CMK-3 not only ensures the complete occurrence of redox reactions but also facilitates the physical entrapment of long-chain lithium polysulfides during the cycling process, significantly improve the capacity ability of the Li-S cells.[53] Inspired by that, other ordered mesoporous carbons were developed for sulfur cathodes subsequently. Schuster et al. developed a composite of sulfur with bimodal mesoporous carbon (BMC), which exhibited a high reversible specific capacity of 1200 mAh g^{-1} and good cycle stability, benefiting from the high surface area of 2445 $m^2 g^{-1}$ and large inner pore volume of 2.32 $cm^3 g^{-1}$.[54] C@S composites, based on mesoporous hollow carbon capsules, were prepared as cathodes for Li-S cells, offering an extended cycling life and improved rate capability.[55] This improvement was attributed to the effective confinement of lithium polysulfides within the void space of the hollow carbon capsules and the good electron transportation within the materials.

In addition to carbon materials, polymers are another category of materials that are widely applied in the study of Li-S batteries, especially as binders of electrodes. Poly (vinylidene fluoride) (PVDF), a conventional binder, provides strong adhesion to the mixture of active material and conductive additive, exhibits relative stability in the ether-based electrolyte used in the Li-S battery system.[56] However, PVDF does not bind long-chain lithium polysulfides, nor

does it suppress the occurrence of PS shuttle during the charge/discharge process.[57] To address these limitations, researchers have explored a hydrophilic binder with strong polarity and viscosity, which has shown excellent ability in anchoring polysulfide species.[58] In addition, they are also widely used in Li-S batteries as physical barriers to block the migrations of soluble lithium polysulfides, thereby enhancing the utilization of active materials in subsequent cycles, and eventually improving the reversibility of the battery. For example, a sulfonated poly (ether ketone)/Nafion (SPEEK/Nafion)-modified separator has been employed in the Li-S cells to mitigate the shuttle effect.[59] The thin composite coating layer on the cathode side of the separator serves as a selective barrier, allowing only Li ions to pass through while blocking PS species. This approach effectively reduces the shuttle effect, and the cell has demonstrated stable cycling performance with a capacity of 600 mAh g^{-1} over 300 cycles.

1.3.2 Chemical Adsorption of PS

Although porous carbon materials can greatly improve electrical conductivity and partially mitigate the shuttle effect, the conjugate nonpolar carbon planes cannot strongly anchor polar lithium polysulfide molecules.[60] Therefore, introducing more polar sites to the nonpolar carbon materials has been proposed to provide stronger chemical binding with polysulfide species. One effective method to achieve this is by doping the carbon surface with heteroatoms, such as nitrogen (N), sulfur (S), oxygen (O), boron (B), chloride (Cl), and fluorine (F). These heteroatoms enhance the interaction between the carbon host and long-chain PS, forming chemical bonds that help impede the shuttle effect. Carbon materials such as graphene and CNT, which possess abundant edges and boundaries, are favorable for heteroatoms doping because they can easily incorporate into the carbon lattice.[61] Numerous studies have reported on novel materials featuring heteroatom doping.[62–65] To further investigate their impact on the

electrochemical performance of Li-S cells, Hou and colleagues performed density function theory calculations on nanocarbon doped with various heteroatoms.[61] Their findings indicated that N and O atoms have larger binding energies with intermediate products compared to other examined dopants, like B, Cl, F, and S atoms. The introduction of N and O atoms enhances the chemical adsorption of soluble long-chain lithium PS with cathode materials, eventually reducing the loss of active materials in the cathode and relieving the corrosion of lithium anode. Further investigations into the effect of nitrogen and oxygen doping were conducted by introducing them in N330, a commercial carbon black, through treatment with NH_3 and CO_2.[66] Although the composites displayed similar cycling stability, N330 with nitrogen doping (N-N330) demonstrated a higher initial specific capacity of 1490 mAh g^{-1} compared to the oxygen-doped carbon (O-N330). The difference is attributed to unexpected reactions between sulfur and surface oxygen species, which produce the S-O groups and cause the loss of active materials during cycling. In contrast, nitrogen on the carbon surface facilitates the interaction with intermediate products to limit their migration more effectively to the anode. It also promotes a more uniform distribution of the discharge products within the carbon matrix, resulting in improved electrochemical performance.

The doping process can sometimes be complex due to various factors. To simplify the synthesis process and reduce manufacturing costs, researchers have proposed using biomaterials that are naturally rich in heteroatoms like oxygen and nitrogen as precursors for carbon host materials. For example, Wu et al. selected bagasse, a byproduct of sugar production, as a precursor.[67] The resulting carbon from bagasse possesses a unique tri-modal porous structure and contains oxygen and nitrogen atoms, which are inherently present in bagasse, on its surface. These co-doping sites provide an intrinsic affinity toward lithium polysulfides through dipole-

dipole electrostatic interactions, effectively mitigating the shuttle effect. In addition, they contribute to the uniform deposition of solid Li_2S on the cathode, leading to better utilization of active materials. The resulting cathode exhibits a high initial specific capacity of 1123 mAh g^{-1} at 0.2 C and a low capacity decay rate of 0.057% per cycle over 800 cycles at 1 C.

Inorganic materials, like metal oxides, nitrides, and sulfides are also favorable for mitigating the shuttle effect because they are inherently rich in oxygen, nitrogen, sulfur atoms compared to carbon materials.[25] Therefore they can form chemical bonds with lithium polysulfides to realize chemical adsorption. In the beginning, metal oxides were used as additives in the cathode to improve the performance of the cell. For example, the addition of 15 wt% of magnesium nickel oxide ($Mg_{0.6}Ni_{0.4}O$) to the sulfur cathode optimized the cell's performance. The cell delivered a much-improved initial specific capacity of 1158 mAh g^{-1} compared to the cell without additive, which only delivered a capacity of 741 mAh g^{-1}. TiO_2 has also been used as an additive in sulfur cathodes.[68] Among several TiO_2 with different morphologies, α-TiO_2 displayed the highest initial specific capacity of 1201 mAh g^{-1} and better cycle stability. These results can be attributed to the higher binding energy of sulfur-containing species to α-TiO_2 than other TiO_2.[60]

Although the composites of sulfur and inorganic materials can provide stronger chemical adsorptions for PS by forming chemical bonds with them, their lower conductivity and limited sulfur loading capacity result in relatively low output capacity and rate capability. Therefore, many researchers have shifted their interests towards making composites that can utilize the concept of both physical and chemical adsorption to better immobilize long-chain lithium PS within the cathode side. One such innovation is the silicon/silica@carbon-sulfur (Si/SiO_2@C-S) carbon sphere composite, which has demonstrated remarkable performance. This composite not

only showed a high initial specific capacity of 1215 mAh g^{-1} at 0.1 C with a low capacity decay of 0.063 % per cycle over 500 cycles but also a high capacity of 825 mAh g^{-1} at 2 C, indicating the good rate capability of the cell.[69] These excellent electrochemical performance of the obtained Si/SiO_2@C-S cathodes can primarily be attributed to the synergetic effect of micro-mesoporous graphitic carbon and the Si/SiO_2 network. The porous carbon enhances the loading of active materials and acts as a physical shield for the polysulfide species. At the same time, the cross-linked structure can chemically bind the polysulfides and suppress their migrations in the electrolyte.

The sluggish redox kinetics is also a challenge that impacts the overall performance of Li-S batteries. This issue arises from the insulating nature of sulfur and its final discharge product (Li_2S), as well as the complex reaction pathways from polysulfide species to Li_2S_2/Li_2S and the dissolution of intermediate discharge products, which increase the viscosity of electrolyte. Such slow redox reactions result in low sulfur utilization and compromised capacity. Realizing rapid conversions between soluble polysulfides and insoluble Li_2S_2/Li_2S is crucial for mitigating the shuttle effect, as it decreases the maintaining time of lithium polysulfides in the electrolyte, thereby preventing their migration, reducing active materials loss and ultimately enhances the overall performance of the Li-S cell.[70] Moreover, the faster conversions promote a more uniform distribution of Li_2S on the electrode, potentially lowering internal resistance and enhancing the charge-discharge rate. The catalytic role of certain polar electrode host materials in facilitating these redox reactions between polysulfides and final discharge products is notable.[71] Unlike traditional catalysts, the surface state of catalytic materials used in Li-S batteries evolves during the reaction, yet they effectively promote conversions and aid the active material to accept ions or electrons.[72] Transition metal compounds, such as metal oxides, metal sulfides, and metal

nitrides, are ideal for catalytic materials used in cathodes because their polar surfaces are suitable for chemical reactions with sulfur species.[72] Although metal-free materials, like phosphorene and N-doped carbons, are less commonly utilized as catalysts, reports indicate they also exhibit catalytic effects and significantly lower the polarization of electrodes, facilitate redox reactions, and reduce the shuttle of polysulfides during the cycling process.[73,74]

1.3.3 Short-chain Sulfur Cathodes

Given that the shuttle effect arises from the dissolution and migration of long-chain PS in the ether-based electrolyte, a viable approach, in addition to anchoring these intermediates at the cathode side to prevent their transport, involves substituting the ether solvent used in electrolyte to inhibit polysulfide dissolution. Although carbonate solvents typically undergo undesirable nucleophilic-electrophilic substitution reactions with lithium PS, they are helpful in suppressing the shuttle effect when used correctly.[29] To incorporate carbonate solvent in Li-S batteries effectively, it is crucial to prevent direct contact between soluble PS and the carbonate solvent. One promising approach is to anchor short-chain sulfur onto the cathode through covalent bonding, which helps stabilize sulfur and prevent its dissolution. The structure and transformation of sulfur at different temperatures is depicted in Figure 1-3.[75] Sulfur begins to melt at 120 ºC, reaching its minimum viscosity at 155 ºC. As the temperature increases to 159 ºC, the S-S bond in S_8 ring start to break, leading to the formation of sulfur diradicals and the production of "polymeric sulfur" with high molecular weights.[76] At a higher temperature of 444 ºC, short-chain sulfur vapor with different lengths form. However, when the temperatures cool down to room temperature, these short-chain sulfur species will transfer back to the most stable structure of S_8 ring.

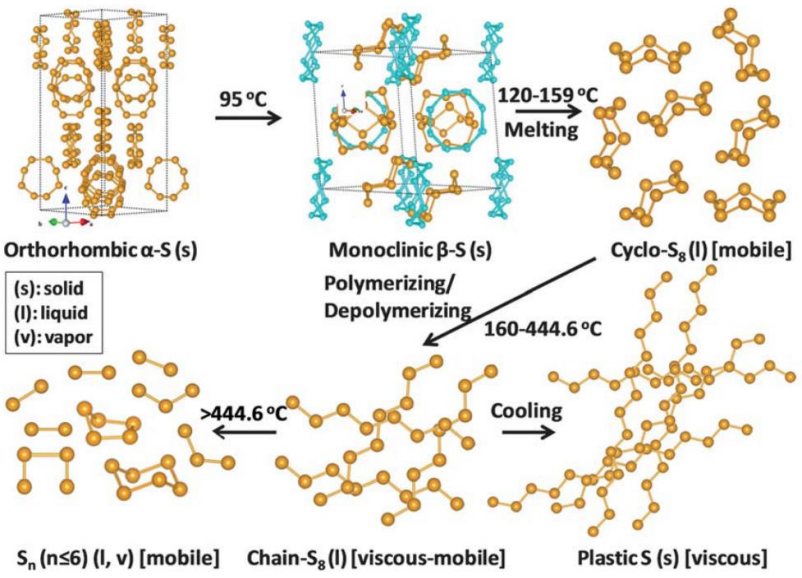

Figure 1- 3. Structure and transformation of sulfur at different heating temperatures.[75]

Microporous carbon materials have been reported as reservoirs for trapping short-chain sulfur species. For example, Xu et al. confined S_2 within a carbon featuring a sub-nanometer porous structure, revealing a new sulfur chemistry for the short-chain sulfur cathode in the carbonate-based electrolyte.[77] Different with Li-S cell using S_8 as active material in ether-based electrolytes, which need to experience a solid-liquid-solid conversion process, cells using short-chain sulfur species in carbonate solvents display a single plateau in charge/discharge curve, corresponding to a solid-to-solid conversion.[29] in this configuration, a new type of thiocarbonate-like solid electrolyte interphase (SEI) forms on the anode, acting as a barrier that prevents contact between sulfide species and the electrolyte.[77] This thin SEI layer, which forms on the exterior of the C/S cathode during the initial discharge process, results from the reactions between the carbonate solvent and some stable exterior S_8 that are produced during the composite's synthesis. The SEI-coated S/microporous carbon cathode displayed exceptional cycling stability over 4000 cycles with a low capacity decay rate of 0.0014% per cycle.

Copolymerizing sulfur with conductive polymers is another strategy for utilizing short-chain sulfur and modifying the structure of active materials in Li-S batteries. Polyacrylonitrile (PAN) is one of the commonly used conductive polymers for this purpose. Because sulfur acts as a dehydrogenating agent, sulfurized polyacrylonitrile (SPAN) can be synthesized through subliming a mixture of sulfur and PAN at 280-300 ºC.[78] The resulting SPAN cathode displays a single discharge plateau located at 1.8 V in the charge/discharge curves, which is speculated attributed to the strong interaction between the polymer and sulfur, indicating the successfully prevent of the dissolution of intermediate polysulfide products. With the advance of the research, more and more studies have focused on the potential of SPAN as a cathode material for Li-S batteries. For example, Yu et al. investigated the effects of heating temperatures on the properties

and electrochemical performance of SPAN.[79] Their results demonstrated that the SPAN cathode materials can achieve optimal cycling performance when synthesized at temperatures range in 450-500 ºC. The structural properties and reaction mechanisms of SPAN cathodes were further investigated using solid-state nuclear magnetic resonance (NMR), electron paramagnetic resonance (EPR), and simulations. These investigations revealed that during the initial discharge, the cleavage of S-S bonds generates thiyl radicals, which contribute to the subsequent formation of a conjugated structure.[79] Lithium ions interact with the electronegative sites around sulfur and nitrogen atoms, preventing the formation of lithium PS, which is evidenced by exhibiting combability with carbonate-based electrolyte. This effectively suppresses the shuttle effect, enabling the Li-S cell with a SPAN cathode to achieve an excellent capacity retention of 96.8% after 2000 cycles.

1.4 Practical Application of Li-S Batteries

In research that primarily focused on optimizing cathode materials for Li-S batteries, coin cells are commonly employed for testing, and specific sulfur content in the cathode is applied to evaluate the electrochemical performance of these cells. However, energy density emerges as a more critical parameter for the practical application of Li-S batteries. While increasing the sulfur content in the cathode can significantly enhance the electrode's capacity, simply adding more sulfur can decrease the utilization of active materials due to the insulating nature of sulfur. Therefore, optimizing electrode design and achieving a balance between the content and utilization of active materials is essential for advancing the practical application development of Li-S batteries. Beyond achieving high utilization of active materials and maximizing output voltage, both the areal sulfur loading and the ratio of active materials to inactive materials are

critical factors in achieving the high energy density required for the effective implementation of the Li-S battery technology.[24]

In coin cell testing, thin film with low sulfur loading and high electrolyte/sulfur (E/S) ratios (> 15 μL mg^{-1}) are usually employed to study cathode materials.[80] However, in practical applications, where cylindrical or pouch cells are the standard formats, applying the same conditions to these large-scale batteries often results in poor electrochemical performance. The areal sulfur loading is typically the parameter used to describe the sulfur content in a pouch cell, and higher areal loading generally leads to greater energy density for the entire cell.[81] Therefore, it is one of the most critical factors influencing the practical viability of Li-S batteries. For Li-S batteries to compete with current commercial Li-ion batteries, the areal capacity of the sulfur cathode should ideally reach 4-8 mAh cm^{-2}.[82] In addition, the electrolyte, though an inactive component, constitutes a significant proportion of the total mass of the pouch cell and can significantly influence the overall performance of Li-S batteries.[24] An excessive amount of electrolyte can impact the actual energy density output. In contrast, too little electrolyte may limit electrode infiltration and affect sulfur utilization in the cathode. Shi et al. explored the effect of the E/S ratio on the electrochemical performance of a 2 Ah multi-layer pouch cell with an integrated S/Ketjenblack (KB) cathode.[83] Different E/S ratio was applied, including 6, 4, 3, and 2.5 μL mg^{-1}. Although lowering the E/S ratio increased the cell's energy density, it also led to rapid declines in cycling performance. This accelerated degradation of Li-S pouch cells with lean electrolyte can be attributed to inhomogeneous reactions at the lithium anode and limited electrolyte diffusion in the thick cathode. These issues lead to lithium metal corrosion, electrolyte consumption, and uneven sulfur reactions within the cathodes. In addition, the viscosity of the electrolyte tends to increase with cycling in lean electrolyte systems, which slows the kinetics of

electrochemical reactions, heightens cell polarization, and affecting the rate performance.[82] Therefore, balancing sulfur content with the volume of electrolyte is critical. Consequently, the E/S ratio emerges as another key parameter in the design of high energy density Li-S pouch cell.

Optimizing the cathode material design is one of the most effective strategies for achieving high-performance Li-S cells with high sulfur content and low E/S ratio. For example, a three-dimensional (3D) hollow carbon fiber foam has been proposed as a conductive host and free-standing current collector for cathodes with high areal sulfur loading.[84] The cross-linked structure not only provides efficient transport pathways for electrons but also enhances sulfur utilization even under a low E/S ratio of 4 μL mg^{-1}. The excellent electrolyte absorbability of the 3D foam aids in anchoring the polysulfides within the matrix, thereby improving the cycling performance of the cell. The resulting cell displayed a high areal capacity of 6.4 mAh cm^{-2} with a relatively high sulfur loading of 6.2 mg cm^{-2}.

In addition to the areal sulfur loading and E/S ratio, the rapid degradation of the large-scale pouch cell is also related to the lithium anode side. Cheng and colleagues investigated the failure mechanisms of Li-S pouch cells, focusing on a 1500 mAh pouch cell.[85] Compared to coin cycled at the same rate, pouch cells experience a higher current density at the anode due to the larger sulfur content. This increased current density accelerates the growth of lithium dendrites, which consequently forms dead Li powder in the electrolyte. The accumulation of dead lithium significantly increases polarization, ultimately terminating the cycling of the pouch cell.

In recent years, the performance of Li-S pouch cells, characterized by high areal sulfur loading and lean electrolyte, has gradually improved due to the electrode design optimization.[86–

[88] However, despite these developments, Li-S batteries remain in the early stages of commercialization compared to current LIBs. Several companies like Sion Power, Oxis Energy, and PolyPlus have developed prototype Li-S cells, yet these cells have been limited to specific applications, like unmanned aircraft, and have not yet been mass-produced. Commercial Li-S battery products are still absent from the market. One of the primary barriers to commercialization is the unstable cycling performance of Li-S batteries, which is crucial for achieving high energy density battery and competing with conventional commercial LIBs. This instability is particularly pronounced in large-scale cells with high areal sulfur loading and lean electrolyte. Furthermore, the complex synthetic process of those effective novel host materials reported in the literature makes them unsuitable for large-scale production. Another significant challenge is achieving high-rate capability, an important characteristic of high-power electric equipment. Moreover, safety issues induced by the dendrite growth on lithium metal anode also pose a barrier to large-scale production of Li-S batteries. Therefore, bridging the gap between practical production and academic research is essential to facilitate the widespread application of Li-S batteries across various sectors.[89]

1.5 Objectives and Scope of the Research

The research presented in this thesis aims to develop novel host materials to enhance the electrochemical performance of Li-S batteries. A bio-inspired carbon was synthesized using the degummed silk as the precursor through a facile carbonization process. This newly obtained material features a hierarchical porous structure along with natural nitrogen atoms, which eliminates the need for extra heteroatoms doping process, from the original components of the precursor. These characteristics make the prepared nitrogen-doped carbon (NC) a candidate as the carbon host material for sulfur cathode to improve the electrochemical performance of Li-S

batteries. The synthesis process, structure characterizations, and electrochemical analysis were explained in Chapter 2.

Chapter 3 investigated the specific mechanisms by which NC improves electrochemical performance. It was found that NC can facilitate the disproportionation reactions of polysulfide anions, converting long-chain polysulfides anions into elemental sulfur and Li_2S_2 after their formation at the sulfur cathode. Enhancing these reactions helps to reduce the remaining time of polysulfides in the electrolyte, therefore mitigating the shuttle effect and improving the cycling performance of the Li-S battery.

Large-scale pouch cells were also assembled to test the feasibility of the novel S/NC electrodes in practical applications. Chapter 4 discusses the influence of different sulfur loadings and electrolyte/sulfur ratios on the pouch cells' performance. In addition, except for the cathode, the morphological changes of the Li anode and their effects on the long-term cycling of Li-S cells were also investigated, considering various factors that impact the entire cell.

CHAPTER 2. SYNTHESIS AND CHARACTERIZATION OF NOVEL CARBON HOST FOR SULFUR CATHODES

2.1 Introduction

LIBs are the state-of-the-art energy storage technologies today. Unfortunately, further improvements of LIBs using traditional insertion electrodes are gradually reaching their limit. An energy density around 300 Wh kg^{-1} at present is hardly able to meet the ever-growing energy storage demands for electric vehicles.[86,90,91] Therefore, alternative battery systems have been explored. Li-S batteries are one of the potential candidates for the next generation energy storage systems. The Li-S batteries possess a high theoretical specific capacity of 1675 mAh g^{-1} and a high energy density of 2600 Wh kg^{-1} due to a multiple-electrons conversion reaction. Sulfur is a low cost and abundant material on the earth.[21] Although Li-S batteries have been studied for decades, their poor cycling life, is still a major issue hindering the implementation of their practical applications. The poor cycle life can be attributed to the insulating nature and large volume change of the sulfur cathode, as well as the shuttle effect that occurs during cycling. The shuttle effect is caused by the diffusion of dissolved high-order lithium PS to the lithium metal and the backward diffusion of the formed low-order ones in a conventional ether-based electrolyte, [27,92] Moreover, some insoluble low-order lithium PS were formed and deposited on the surface of the lithium anode, which could lead to the loss of active materials of the sulfur cathode and affect the cyclability of Li-S batteries.[61]

Enormous efforts have been invested in recent years to circumvent the shuttle-effect issue and improve the overall electrochemical performance of Li-S batteries. Two main approaches to block off the propagation of soluble high-order lithium PS in the electrolyte included physical confinements and chemical binding.[91] Encapsulation of the PS within the hierarchically porous

carbon host was an effective way to mitigate the shuttle effect. The micro and mesopore structures of the carbon could act as a host to restrain the migration of soluble lithium PS and alleviate the volume variations of a sulfur electrode during cycling.[93,94] In addition, the conductive carbon matrix also provided an essential electrical conductivity network for a sulfur electrode, which could greatly improve the utilization of the active materials.[53,95–97] In order to achieve the chemical adsorption of PS at the cathode side, several novel materials have been proposed as potential hosts for the sulfur composite cathode. For instance, Y. Yen et al. utilized a type of the porous molecular crystal with unique adsorption characteristics as the lean-electrolyte cathode.[98] In addition to exploring new materials, an alternative approach commonly employed to enhance the overall performance of Li-S batteries is to introduce heteroatoms, such as nitrogen and boron, into the host materials. This serves to chemically anchor the high-order lithium PS and catalyze the conversion reaction during the cycling process.[99] Wang and co-workers demonstrated that nitrogen could modify the electronic structure of the oxygen in adjacent function groups and strengthen the chemical binding between the sulfur and oxygen-containing groups on a carbon matrix. The Li-S battery made with N-doped carbon demonstrated a better cycle stability.[100] Moreover, abundant defect sites induced by the nitrogen can also lead to a uniform distribution of the discharge products within the carbon host, which consequently enhanced the utilization of the sulfur.[66,101]

Biomass has aroused great interest as a precursor for the carbon matrix because of its low cost, abundant resources, and environmental friendliness. The utilization of biomass precursors for the production of carbon materials results in a diversity of morphologies. Porous structures have been identified as capable of physically obstructing the diffusion of polysulfide ions. Moreover, post-carbonization heteroatom doping has been observed to enhance the carbon

surface with multiple functional groups, which exhibit a strong propensity for chemical interaction with polysulfide ions. This results in effective immobilization and entrapment of the polysulfide anions, thereby improving the overall performance of the carbon material in lithium-sulfur batteries.[102] Hence, biomass-derived carbons have been widely applied to studies of Li-S batteries.[103,104] Manthiram and co-workers developed a cotton-based carbon for a sulfur cathode through a facile carbonization process using cotton as the precursor.[105] The product retained the porous and 3D interconnected structures of the cotton, which accommodated a high sulfur loading, improved the active material's utilization, and stabilized the Li-S battery's cyclability.[105] Another porous carbon, which possessed a scale-like microstructure, was developed using kapok fiber as a raw material.[106] The unique structure of the obtained carbon provided an efficient electric contact to the sulfur and effectively obstructed the diffusion of the dissolved polysulfides during the discharge process.[106]

Herein we synthesized a novel bi-functional carbon as the carbon host for sulfur cathodes by using a degummed silk as a precursor through a facile carbonization process.[107] Natural silks produced by silkworms are protein polymers enriched in nitrogen element and are very easy to obtain because of their abundant resources on the earth. Therefore, silks are expected to be an ideal raw material to produce the nitrogen-doped carbon (NC) host through a facile carbonization process without any additional doping process.[92,108] The obtained NC not only possesses a high surface area with optimized mesopore structures, but also exhibited activity to facilitate the disproportionation of polysulfide to short-chain polysulfide and elemental sulfur. The content of nitrogen doped in the carbon usually changes with the pyrolysis temperature.[109] We prepared NC at various carbonization temperatures to examine its influence on the composition and the structure of the carbon as well as the sulfur cathode properties.

2.2 Experiment

Synthesis of hierarchical porous and NC from cocoons.

The bombyx mori cocoon, produced by silkworm, was originally from the southern part of China. The sericin, the gum-like protein that coats the silk fibroin fibers, was first removed through an alkali degumming method. The alkalis can form bonds with sericin and form caustic soda, and then dissolve in the water during the hydrolysis process.[110] It is a degumming technique that widely applied in both laboratory and industry because of the high efficiency. Here, the sodium carbonate (Na_2CO_3) was selected as the alkali. The process includes boiling the cocoon in the Na_2CO_3 solution to remove the glue-like sericin protein. Then, 2 grams of the degummed natural silk were dissolved in the mixture of calcium chloride ($CaCl_2$), de-ionized water (H_2O), and ethanol (CH_3CH_2OH) in the ratio of 8:2:1 at 90 ºC overnight. The regenerated carbon precursor was finally acquired by further drying the solution at 140 ºC for 12 h. The obtained precursor was first heated at 300 ºC for 1 hour under an Ar atmosphere with a heating rate of 2 ºC min^{-1} for a pre-carbonization. Then, to investigate the effect of carbonization temperatures on the structures and nitrogen content of the carbon, the precursor was further annealed at 750, 800, 900, and 950 ºC under the Ar atmosphere separately. The product was added into a 1 M HCl solution and stirred overnight to remove the residual $CaCl_2$ trapped in the carbon. The $CaCl_2$ was wrapped over the silk fibroin as a template after the regeneration step. Finally, the obtained powder was washed thoroughly with deionized water and dried at 70 ºC overnight. Carbons acquired at different carbonization temperatures were named NC750, NC800, NC900 and NC950. During the carbonization process, the wrapped $CaCl_2$ also acted as a template, which helped to induce porous structures to the carbon.

Preparation of S/NC composite

The S/NC composite was prepared through a melt-diffusion method. The NC was evacuated in a three-necked round-bottom flask overnight to remove air within the pore structures of the carbon. Appropriate amount of sulfur was dissolved in the carbon tetrachloride (CCl_4). The solution was then inhaled into the flask due to the negative pressure inside the flask. The resulting mixture solution was stirred vigorously overnight for a thorough infiltration of sulfur into the NC host materials, and then evaporated under vacuum to fully remove the CCl_4 solvent. Finally, the obtained mixture of the sulfur-containing NC was sealed in a glass tube under vacuum and heated at 155 ^{o}C for 12 h to synthesize the S/NC composite. At 155 ^{o}C, the viscosity of sulfur is the lowest, which allows more sulfur to penetrate the smaller porous structures of the host materials. Sulfur was incorporated with NC in different weight ratios of 6:4 and 8:2. The schematic of the synthesis process of NCs are depicted in Figure 2-1.

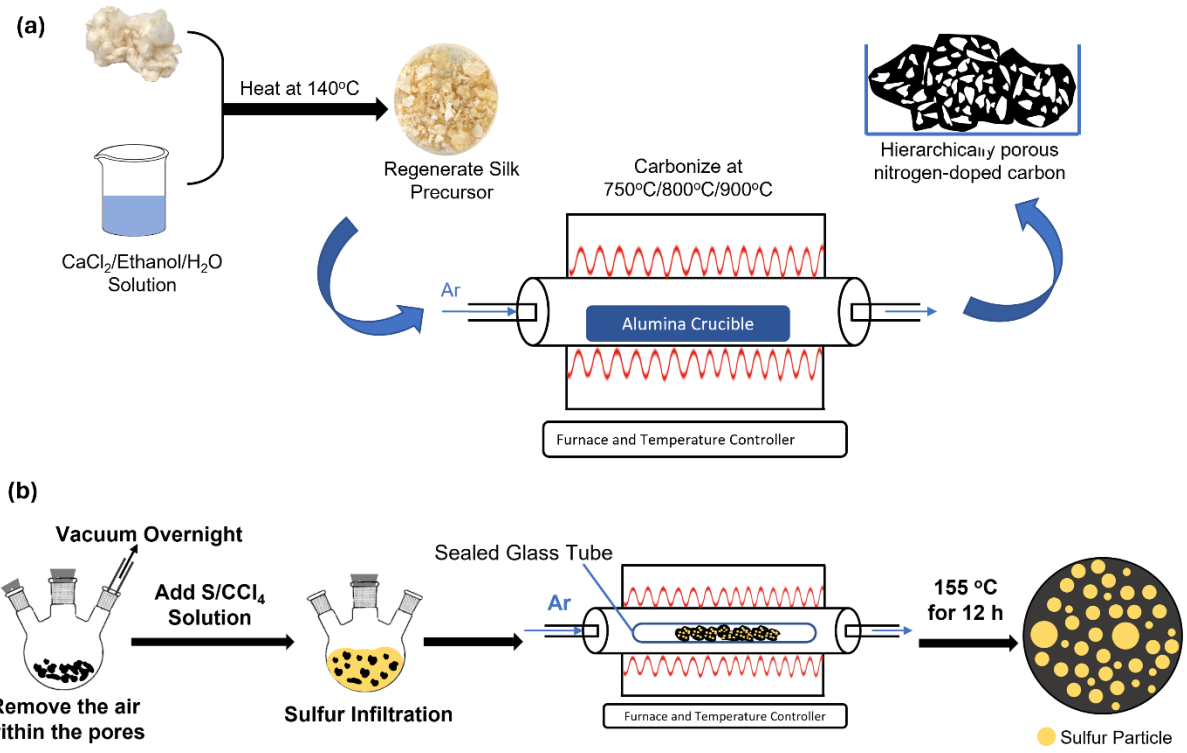

Figure 2- 1. Schematic illustration of (a) the synthesis of NC and (b) the preparation of S/NC composite.

Structural characterization

The morphologies of the samples were characterized using a Hitachi S-4800 field emission scanning electron microscope (FESEM) with energy dispersive X-ray spectroscopy (EDS). FESEM, an advanced type of SEM, utilizes a field emission source to generate the electron beam. Different from the conventional SEM, which employs a thermionic emission source, FESEM uses a very sharp, single-crystal tungsten emitter to produce the electron beam. It can provide high-resolution images of the surface of materials. While EDS is a powerful analytical technique used in conjunction with SEM. It works based on the interaction between the electron beam from the SEM and the test sample. EDS allows for the qualitative and quantitative analysis of the elemental composition of the sample.

The porous structures, including the specific surface area, pore volume, pore size, and pore size distribution of the NC samples were then characterized using nitrogen adsorption-desorption isotherm technique on an ASAP2020 physical adsorption analyzer. It works based on the principle of measuring the amount of nitrogen gas adsorbed and desorbed by the tested sample materials at different relative pressures, P/P_0 (P_0, saturation vapor pressure of nitrogen at the analysis temperature). The adsorption/desorption isotherm curves are categorized into six types by IUPAC (International Union of Pure and Applied Chemistry).[111] Therefore, the information of pore structures and adsorption mechanisms can be obtained from the resulting isotherm curves. The specific surface areas of the NCs obtained at different carbonization temperatures were calculated with the multi-points Brunauer-Emmett-Teller (BET) method. BET theory is a mathematical model that can explain the physical adsorption of gas molecules on a solid surface and calculate the specific surface area of materials.[112] The pore diameters, volumes and distributions were determined by the Barrett-Joyner-Halenda (BJH) theory.

To determine the surface chemistry of the NC samples, X-ray photoelectron spectra (XPS) were conducted on a Perkin-Elmer PHI 5400 ESCA system. XPS is a surface-sensitive analytical technique used to study the chemical composition and electronic state of the surface region of solid materials. It can also provide information on the binding states of the elements. XPS is working based on the photoelectric effect. During the measurement, the sample material is irradiated with a beam of X-rays, causing the photoelectrons emit from the surface of the sample surface and the kinetic energy of emitted electrons is measured.[113,114]

X-ray diffraction (XRD) profiles were collected by a Bruker D8 DISCOVERY diffractometer with Cu Kα radiation. XRD is a technique that examines the crystalline structures of materials without destroying the sample. It provides information on structures, phases, preferred crystal orientations, and structural parameters. XRD works based on the principle of X-ray diffraction by crystalline materials according to Bragg's law. During the measurement of XRD, samples are exposed to X-rays over a range of angles, and the intensity of the diffracted X-rays is recorded at the same time. XRD have been widely used in characterizing different materials, such as minerals, polymers, plastics, and metals.[115]

Raman spectroscopy is a non-destructive analysis technique that offers both the chemical and structural information of the sample according to the interaction of light with the chemical bond. It works based on the principle of Raman scattering, which is inelastic scattering of photons. During the measuring, a high intensity excitation laser shines on the sample and a small amount of the light will be scattered at different wavelengths.[116] In order to further investigate the influence of carbonization temperature on the carbon structures of NCs, the Raman spectrum was collected on a Horiba Raman system with a 532 nm laser excitation on a 1200 gr mm^{-1} grating at room temperature. The magnification of the microscope objective was 10×.

Thermogravimetric analysis (TGA) is an analytic technique for the measurement of thermal stability of materials through measuring the change in weight of sample materials with increasing temperatures under a controlled atmosphere. The amount of sulfur incorporated with the NC host was determined by the on the SDT Q600 thermal analyzer in Ar atmosphere from room temperature to 800 ºC with a heating rate of 5 ºC min^{-1}.

Electrochemical characterization

The electrochemical performance of S/NC cathodes was carried out in CR2032 type coin cells. The cathode slurry was first prepared by mixing 85 wt% active materials, 5 wt% binder, and 10 wt% conductive additives with a N-methyl-2-pyrrolidone (NMP) as solvent. The binder used here is 4 wt% polyvinylidene fluoride (PVDF), a commonly used binder to produce electrode for lithium batteries because of its excellent electrochemical stability, wettability with electrolyte and ability to binding active materials and current collector. The binder solution was prepared by dissolving solid PVDF powder into the NMP solvent. The conductive additives that are added to the electrode are superC65. The working electrodes were made by casting the cathode slurry onto a carbon-coated aluminum foil using a doctor blade and dried at 70 ºC overnight to remove extra solvent.

The prepared electrodes were first punched into circle pieces as the cathodes for coin cells. The diameter of the electrodes is ½ in. CR2032 type coin cells with a lithium metal anode and a Celgard 2320 separator were assembled in an Ar-filled glovebox with water and oxygen <0.5 ppm. The electrolyte was composed of 1 M lithium bis(trifluoromethane) sulfonimide (LiTFSI) dissolved in 1,3 dioxolane/1,2-dimethoxyethane (DOL/DME, 1:1 vol%) with 0.4 M lithium nitrate ($LiNO_3$) as an additive. $LiNO_3$ is a commonly used additive for liquid Li-S batteries. It has been reported that it is involved in the formation of a stable SEI on the surface of

lithium anode, which can protect it from reacting with the migrated polysulfide species during cycling process.

Galvanostatic charge/discharge tests, a method of testing the electrochemical performance of cells by applying a constant current, were conducted on an Arbin battery testing system (BT200) in a voltage window of 1.7~2.9 V vs Li^+/Li at ambient temperature to measure the cycling performance of the cells. The tests were conducted at different (1C = 1675 mA g^{-1}) rates. The rate performance of the cells was measured at 0.1, 0.2, 0.5, 1, and 2C for 10 cycles each.

Cyclic voltammetry (CV) is a electrochemical technique to investigate the redox properties of an analyte in solution or of molecular species that is absorbed onto the electrode.[117] During the CV experiment, a potentiostat applies a potential waveform to an electrochemical system and the resulting current that flow through the working electrode will be measured and recorded. The potential is swept linearly with time between the initial potential and final potential. The final voltammogram is obtained through plotting the measured current against the applied potential. To further investigate the electrochemical behaviors of the obtained S/NC cathodes, the CV measurements were conducted by using a two-electrode configuration, with S/NC as working electrode and lithium as a counter and reference electrodes, on a CHI660 potentiostat with a slow scan rate of 0.1 mV s^{-1} and a potential range of 1.7~2.9 V.

The electrochemical impedance spectroscopy (EIS) Impedance measurements is a technique used to analyze the electrochemical properties of materials and interfaces. It works through applying a small, alternating current voltage to an electrochemical cell and measuring the resulting current to obtain an impedance spectrum over a range of frequencies. The spectrum can provide information of the electrochemical reactions that occur at the interface of electrodes

and electrolyte. It is helpful in studying the properties of the battery system, such as kinetics of electrochemical reactions, the resistance of electrolyte, and different stages of complicated mechanisms of the electrochemical system.[118] In this study, the EIS of the cells were conducted using an Autolab PGSTAT30 potentiostat/galvanostat electrochemical system (Metrohm) to investigate the electrochemical process that occurred within the battery. The frequency range was from 0.1 to 10^6 Hz with a perturbation amplitude of 5 mV. Spectra were recorded at the end of selected charge/discharge states.

Color Changing Observation

Two PS mixtures used in this work were 5 mM Li_2S_6 and 25 mM Li_2S_6 in DME/DOL (1:1, vol%). The PS mixtures were obtained by mixing S_8 and Li_2S (molar ratio of 5:8) to form Li_2S_6 stoichiometrically in the mixture of DME/DOL and stirring for 24 h at 60 °C in an Ar-filled glovebox. Five samples were prepared for the experiment. An empty Li_2S_6 mixture was used as the blank group. NC750, NC800, NC900, and NC950 were added into the solution. In addition, the sample with super C65 in the Li_2S_6 solution was also prepared for the comparison. The mixtures were rested in the glovebox for 24 hours and the change of the color was recorded.

2.3 Results and Discussions

2.3.1 Material Characterization

The morphologies of the NCs, prepared at different carbonization temperatures, were examined using FESEM. SEM images of NC750, NC800, NC900, and NC950 at the same magnification are presented in Figure 2-2 (a)-(d). At carbonization temperatures of 750 and 800 ^{o}C, the NC750 and NC800 exhibit aggregated morphologies with distinct porous structures. Notably, NC800 displayed a pronounced honeycomb structure, as clearly observed in Figure 2-2 (b), indicating a better development of porosity. However, with the carbonization temperatures increased to 900 and 950 ^{o}C, there was a noticeable transition towards a more dispersed structure, emerging along with a reduction in pore structures on the NC surface. These changes in the porous structures of NCs can be ascribed to the additional thermal energy absorbed during the carbonization process, leading to the disintegration of the cohesive structures of the carbon.

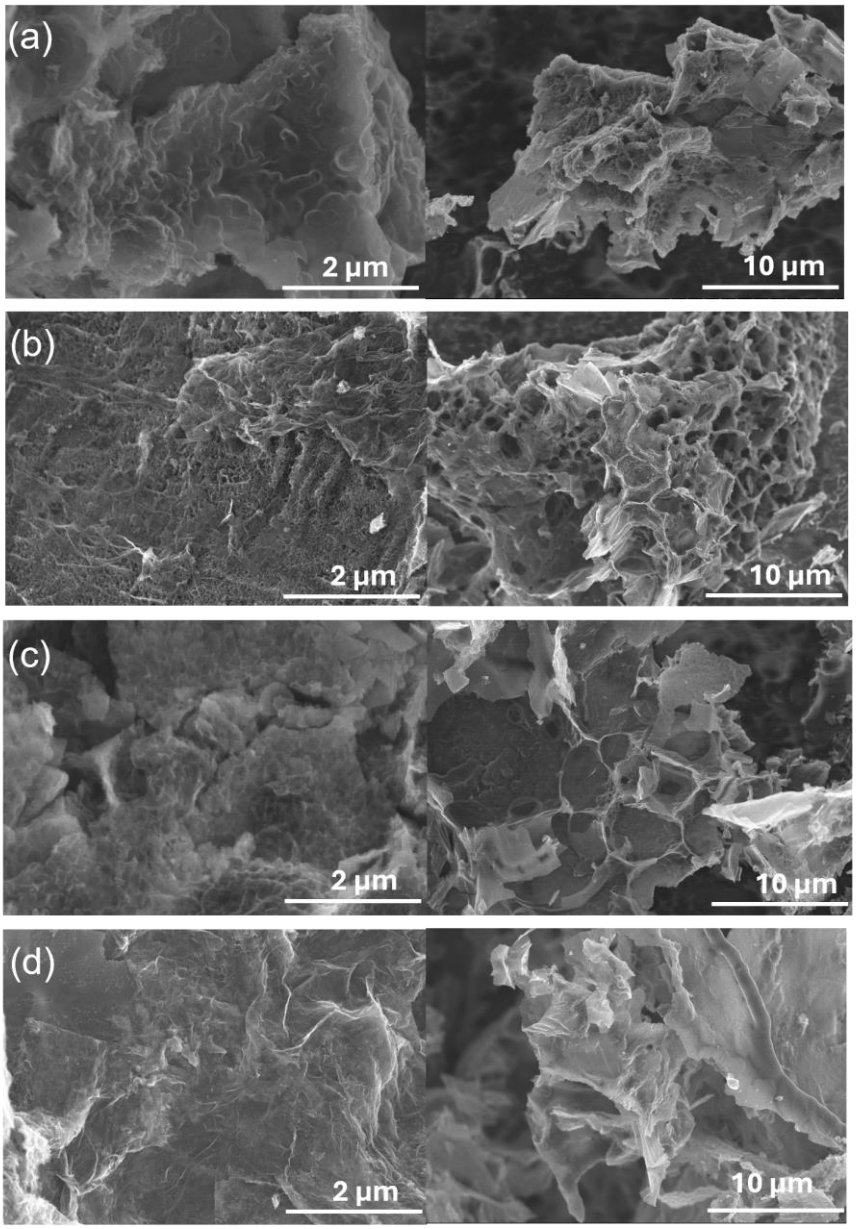

Figure 2- 2. SEM images of (a) NC750, (b) NC800, (c) NC900, and (d) NC950 at different magnification.

The porosity of the synthesized NCs was investigated using N_2 adsorption/desorption isothermal analysis. The isotherm curves for NC800, NC750, NC900, and NC950 are illustrated in Figure 2-3 (a)-(d), respectively. According to the International Union of Pure and Applied Chemistry (IUPAC) categorization, the as-prepared materials exhibited collective isotherm curves of types II and IV.[111] Notably, the presence of an adsorption/desorption hysteresis loop (H3), typically indicative of capillary condensation with mesopores, suggests a hybrid structure of mesopores and macropores. This is because the H3 hysteresis loop attributed to capillary condensation was typically observed in materials with mesopores. It suggested a broad pore size distribution of the shed-like aggregates, which was consistent with that observed from the SEM images. The BJH pore size distribution curves that detailed in Figure 2-2 (e), which shows a vast pore size distribution in the range of 2-60 nm, further underscores the hierarchical porosity of NCs. Despite the fact that all materials displayed comparable pore size distribution characteristics, NC800 has a larger distribution of the pores with an opening larger than 5 nm. The specific surface area, pore volume and average pore size of the NCs are summarized in Table 2-1. Among the NCs carbonized at different temperatures, NC800 has the largest BET specific surface area of 835 $m^2 g^{-1}$ and a total pore volume of 1.74 $cm^3 g^{-1}$. The lower specific surface area and porosity of the sample obtained at 750 ^oC is likely due to the incomplete formation of the pore structures at a relatively low heating temperature, as observed in the SEM images presented in Figure 2-2 (a). After rising the carbonization temperatures to 900 and 950 ^oC, the carbon NC900 and NC950 display a continued decline in porosity. This is because the excess thermal energy that absorbed during the heating process caused the destruction of pore structures. Therefore, according to the above results, NC800, with a greater pore capacity and a balanced pore size, is particularly well-suited for encapsulating polysulfides. This capability to

confine long-chain polysulfides within its mesopores, alongside its ability to better accommodate the volume change of sulfur during the cycling, significantly enhances the potential to hinder the migration of the high-order lithium polysulfides during discharge. Such a feature could consequently improve the stability and cycling performance of Li-S batteries, contributing to their efficiency and longevity.

Table 2- 1. Specific surface area, pore volume, and average pore size of NCs.

Samples	Specific Surface Area ($m^2 g^{-1}$)	Pore Volume ($cm^3 g^{-1}$)	Average Pore Size (nm)
NC750	636.57	1.34	12.5
NC800	835.87	1.74	13.5
NC900	644.74	1.58	10.2
NC950	575.38	1.52	12.2

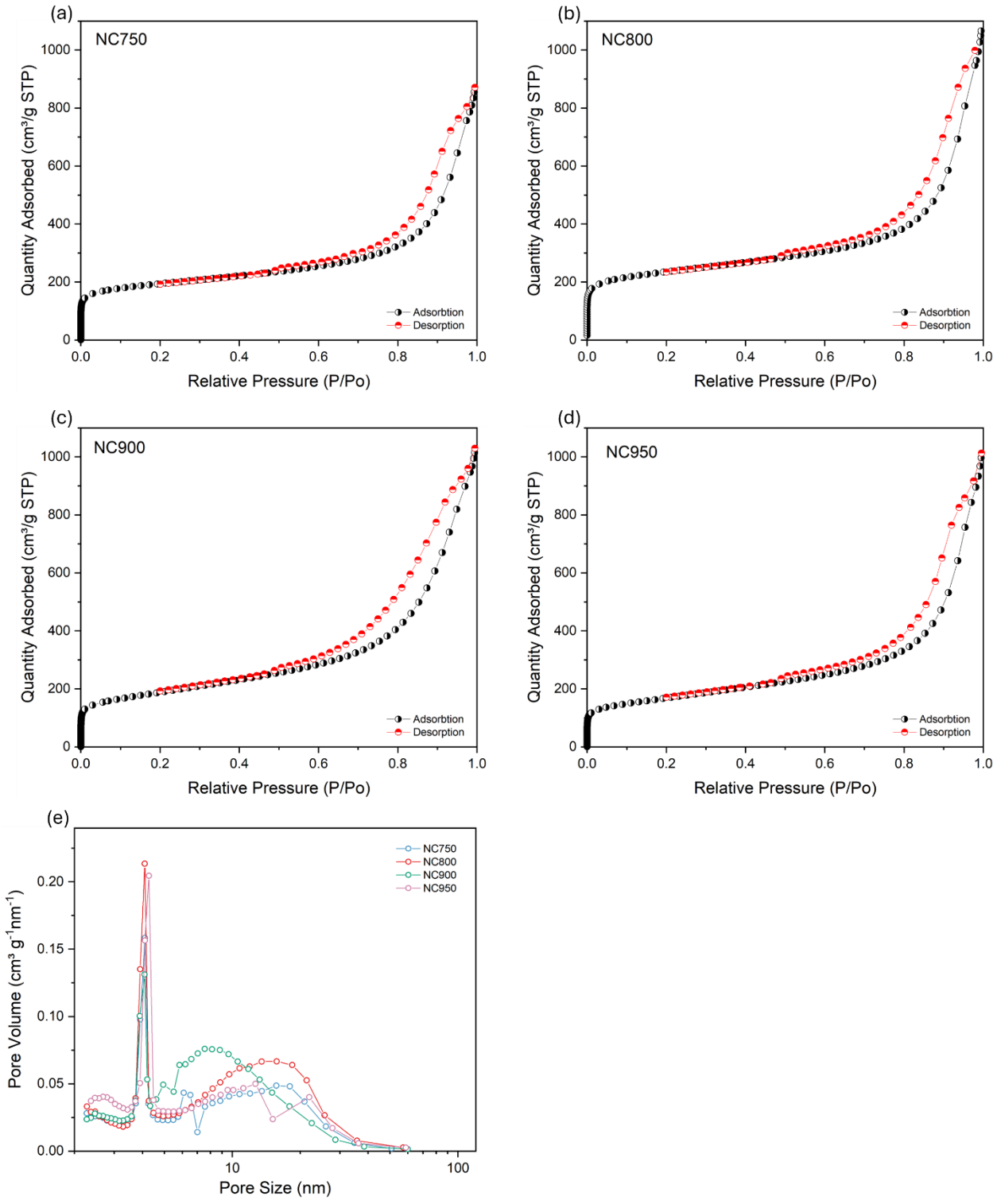

Figure 2- 3. Isotherms of (a) NC750, (b) NC800, (c) NC900, and (d) NC950; (e) pore size distribution.

The XRD was then applied for the investigation of the crystal structures. The XRD patterns of NC750, NC800, NC900, and NC950 are shown in Figure 2-4 (a). The diffraction peaks located at the 2-theta values of about 26º and 44º corresponded to the respective (002) and (101) crystal planes, which are the characteristic peaks of hexagonal graphite. The broad diffraction peaks were ascribed to the amorphous structures of the NCs. In addition, no sharp peaks were observed in any of the samples, which further indicated the disorder nature of the as-prepared NCs. Raman spectra of all the four NC samples are shown in Figure 2-4 (b). The two prominent peaks located at 1336 and 1596 cm^{-1} correspond to the D band and G band, respectively. G band and D band are specific features that appear in the Raman spectrum, particularly for carbon materials. They are related to the vibration mode of carbon atoms. G band measures the graphitization in the carbo materials, while the D band associated with the disorder within carbon materials, which requires a defect in the lattice to scatter light inelastically.[119] The ratio of the intensity of D and G band (I_D/I_G) is a parameter to characterize the degree of disorder or crystallinity of the carbon material. A higher ratio indicates a greater degree of disorder. The value of I_D/I_G of each NC is also displayed inset the spectra. Among all the samples, the NC800 possesses the lowest ratio value, indicating its lower disorder degree compared to other NCs.

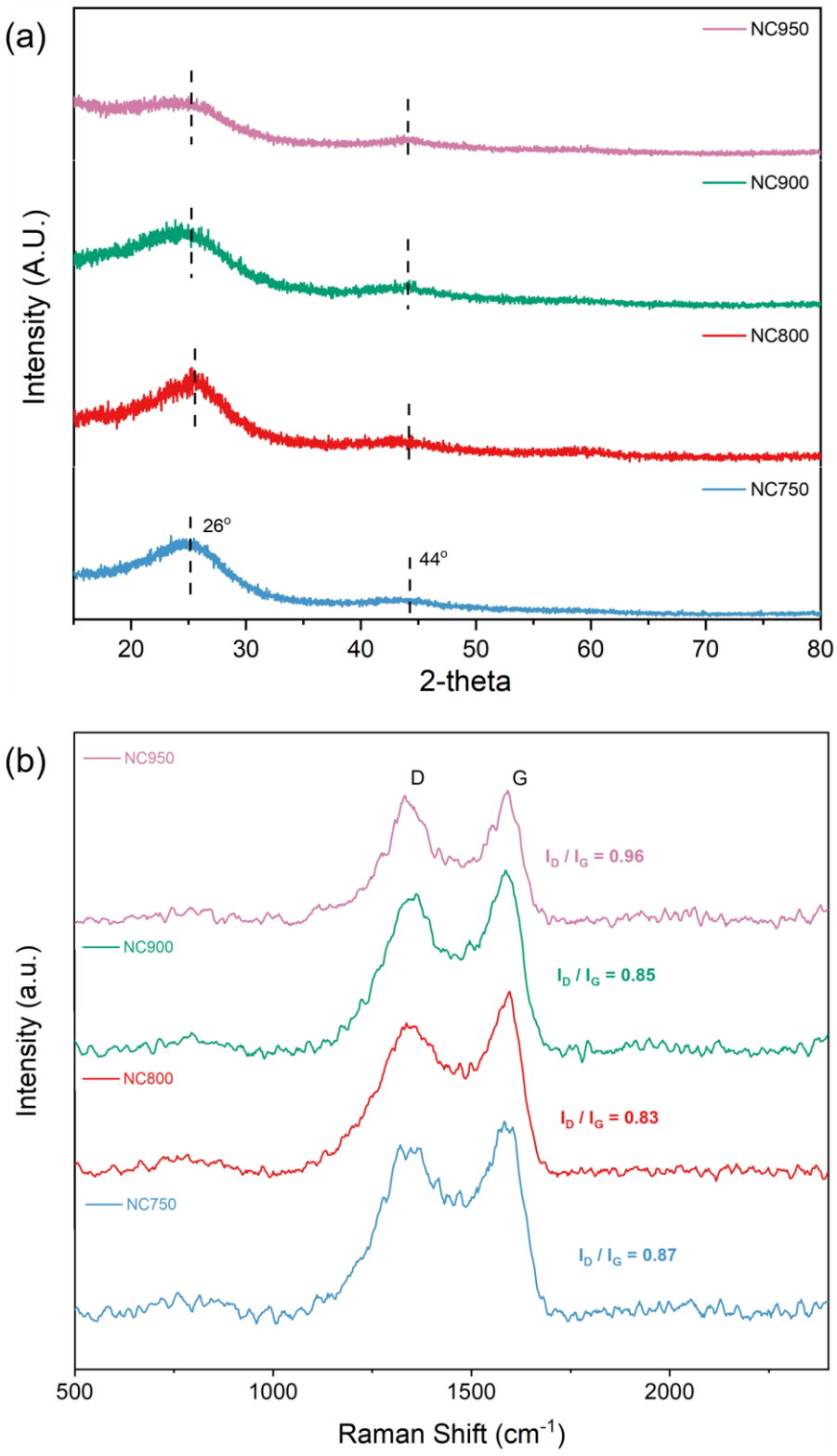

Figure 2- 4. (a) XRD patterns of NC750, NC800, NC900, and NC950; (b) Raman spectrum of NC750, NC800, NC900, and NC950 with I_D/I_G inset.

The XPS survey shown in Figure 2-5 reveals the successful retention of the nitrogen atoms from the raw silk to the NCs. Carbon, nitrogen, and oxygen atoms were assigned independently to the three peaks centered at 286, 399, and 533 eV.[120] The nitrogen concentration (atomic percent) in the NCs measured by XPS and EDS are listed in Table 2-2. The sample carbonized at 800 ºC showed the highest nitrogen content, and nitrogen ratios in the NCs started to decline when the carbonization temperatures increased. The XPS and EDS measurements confirmed the same trend for the change in nitrogen content. The lower nitrogen content of NC750 can be attributed to its unopened pores, as explained before. Some of the nitrogen atoms might remain in those unopened pores and cannot be detected during the XPS and EDS analysis, which can only detect the specific region of the surface of measured sample. The further decline in nitrogen content of NC900 and NC950 was attributed to the elimination of edge nitrogen functionalities triggered by the merging of graphitic domains as the pyrolysis temperature rises. The higher temperatures caused the breakage of weaker N-C bonds and nitrogen volatilization, resulting in lower nitrogen content in NC900 and NC950. The results were consistent with those reported in the literature.[121,122]

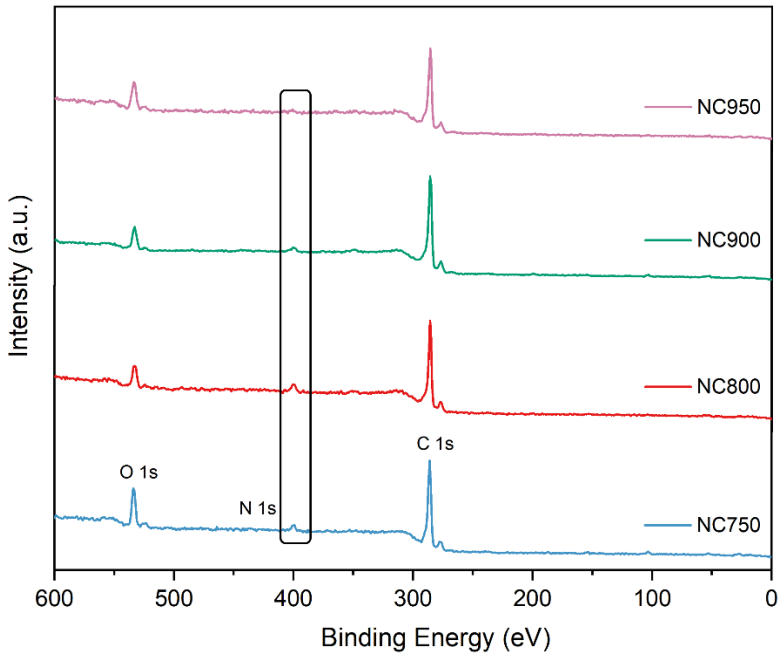

Figure 2- 5. XPS survey of NCs.

Table 2- 2. Nitrogen content of NCs measured by XPS and EDS.

Samples	Nitrogen Content (XPS, at%)	Nitrogen Content (EDS, at%)
NC750	4.9	14.3
NC800	7.4	16.05
NC900	4.3	11.48
NC950	2.6	4.29

Figure 2-6 (a), (c), (e), and (g) display similar Gaussian fits to the C 1s spectrum of NC750, NC800, NC900, and NC950, revealing four peaks denoted as C-C/C=C (284.49 eV), C-O/C-N (285.18 eV), C=O/C=N (286.25 eV), and C=O (288.25 eV), respectively. Figure 2-6 (b), (d), (f), and (h) display the high-resolution XPS spectra of the N 1s peak for the four samples. These spectra can be deconvoluted into three fitted peaks centered at 398.25, 399.87, and 401 eV, corresponding to pyridinic N, pyrrolic N, and quaternary N, respectively. Among all the samples, NC800 possesses the highest ratio of pyrrolic N. Nitrogen atoms with different chemical environments may interact with high-order lithium polysulfides in different ways. The pyridinic N and pyrrolic N show a strong interaction with Li in long-chain PS, while the carbon atoms adjacent to quaternary N can more effectively adsorb S-containing polar species.[123] With the synergetic effect and the highest content of these three types of nitrogen, the NC800 was speculated to be more capable of immobilizing high-order lithium polysulfides and thus mitigating the shuttle effect.

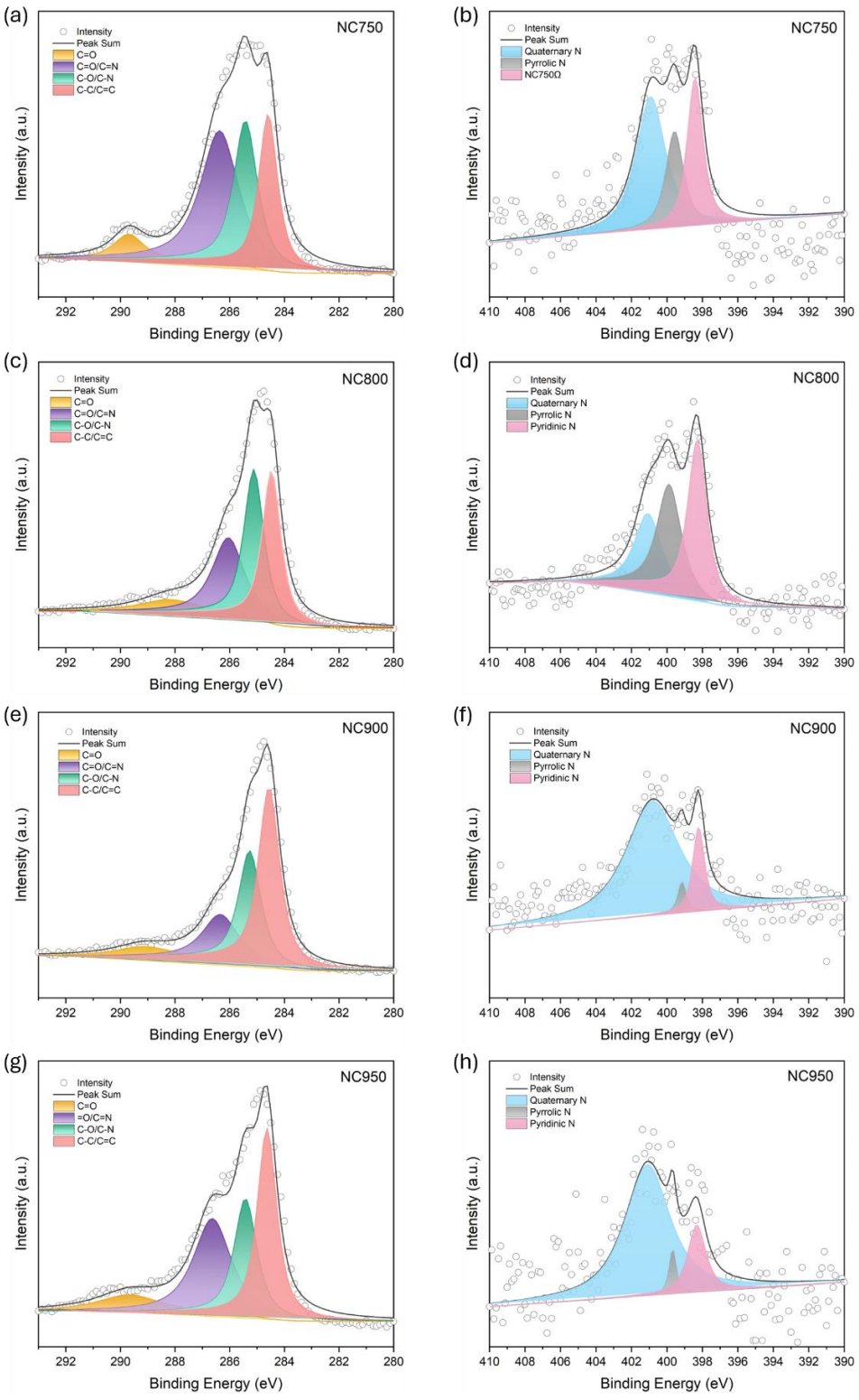

Figure 2- 6. XPS spectra for C1s region and N1s region of (a-b) NC750, (c-d) NC800, (e-f) NC900, and (g-h) NC950.

The synthesis of the S/NC composite was achieved through the melt-diffusion method, involving the heating of the mixture of sulfur and NC host at 155 ºC for 12 hours. This process ensured the complete infusion of sulfur into the porous structures of NC matrix. An initial S/NC ratio of 6:4 was chosen to assess the efficiency of NC hosts. The TGA analysis was carried out in Ar atmosphere, heating at a rate of 10 ºC min^{-1} to examine the thermal behavior of S/NCs and pure sulfur and quantify the specific content of sulfur within the composites. As revealed by the TGA curves in Figure 2-7 (a), the pure sulfur started to lose weight at approximately 215 ºC and is fully sublimed at 350 ºC. However, sulfur integrated within the NC started evaporating at a lower temperature of 150 ºC. This observation demonstrates that the sulfur, when integrated into the S/NC composite, sublimes more readily than in its pure form, suggesting that the sulfur nanoparticles are uniformly distributed and anchored within the NCs.[124] All composites demonstrated a sulfur content of 60 wt%, aligning with the amount that was introduced prior to the heating treatment.

The XRD patterns of the S/NC750, S/NC800, S/NC900, S/NC950, and pure sulfur are presented in Figure 2-7 (b). When comparing the diffraction patterns of S/NCs to that of pure sulfur, the S/NC800 composite exhibits fewer diffraction peaks with lower intensities, indicating a uniform dispersion of sulfur particles throughout the NC matrix. The S/NC750 and S/NC800 composite show lower intensity diffraction peaks than those of S/NC900 and S/NC950, illustrating that their optimized hierarchical mesoporous structures are more effective in accommodating sulfur within the pores rather than on the surface. The high resolution XPS spectrum of the S 2p of S/NC800 composite was depicted in Figure 2-7 (c). The S2p peak centered at 164.25 eV, suggesting the successful loading of sulfur. It can be deconvoluted into three characteristic peaks. The peaks at 164.1 and 165.3 eV were attributed to S $2p_{3/2}$ and $2p_{1/2}$ of

-C-S-C-, respectively. The peak located at 169.01 eV can be explained by the surface oxidation of sulfur or the strong interaction between sulfur and NC800. These results suggest the existence of an interaction between NC and S within the NC host.

The morphologies of the composites were captured through SEM. The SEM images of S/NC750, S/NC800, S/NC900, and S/NC950 are shown in Figure 2-7 (d), (f), (h), and (j). The EDS elemental mappings in Figure 2-7 (e), (g), (i), and (k) show a homogeneous distribution of S within the composite. With the introduction of S, the hierarchical porous structure of NC800 vanished, and it exhibits an even distribution of sulfur compared to other NCs.

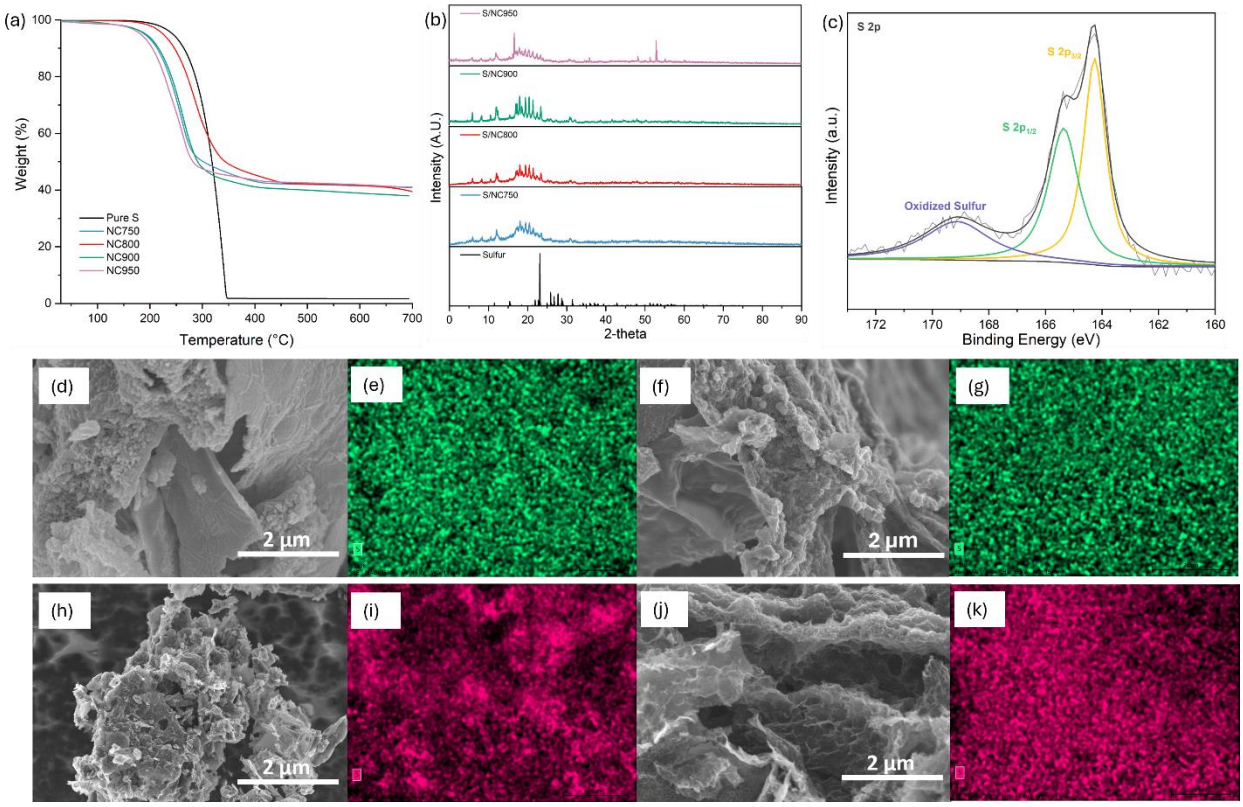

Figure 2- 7. (a) TGA curves of S/NCs sample; (b) XRD patterns of S/NCs, (c) XPS spectra of S 2p region of S/NC800; SEM images and elemental mapping of S of (d-e) S/NC750, (f-g) S/NC800, (h-i) S/NC900, and (j-k) NC950.

2.3.2 Electrochemical Analysis

Comprehensive evaluations of the electrochemical performance of S/NC composites were carried out utilizing coin cells configured with these composites serving as sulfur cathodes. A detailed investigation was initiated through CV analysis to unravel the intrinsic electrochemical behaviors of these cathodes. The cells were scanned at a slow rate of 0.1 mV s^{-1} within a voltage range of 1.7 and 2.9 V. The resultant CV profiles for all four cathodes, as illustrated in Figure 2-8 (a), exhibit the characteristic CV profile of a cathode in Li-S batteries. In the cathodic scan of the first cycle, two distinct reduction peaks were identified at 2.3 and 2.0 V. These peaks are indicative of the sequential electrochemical processes: the initial reduction of cyclic S_8 to form soluble high-order Li_2S_n ($3 \leq n \leq 8$) intermediates, followed by their further transformation into the insoluble Li_2S_2/Li_2S.[125] In the subsequent anodic scan, the partially overlapping oxidation peaks at 2.36 and 2.41 V were associated with the reversible transformation from lithium sulfides to lithium PS and ultimately back to cyclic sulfur. Notably, the peak separation between the cathodic peaks and their corresponding anodic counterparts in the S/NC800 cell was smaller than other S/NC cells. This observation suggests a lower degree of polarization, indicating a higher energy efficiency of the S/NC800 configuration.[126]

The cycling performance of the sulfur cathodes with various NC hosts is depicted in Figure 2-8 (b). The cells were first activated at a low rate of 0.1 C for two cycles and then cycled at the rate of 0.5 C within the voltage range of 1.7 to 2.9 V for 100 cycles. In the first cycle at 0.5 C, the S/NC800 cathode delivered a discharge capacity of 919 mAh g^{-1}, surpassing the capacities of 647, 766, and 697 mAh g^{-1} recorded for the S/NC750, S/NC900, and S/NC 950, respectively. After 100 cycles, the reversible capacities for the S/NC800, S/NC750, S/NC900, and S/NC950 stabilized at 647, 439, 581, and 503 mAh g^{-1}, respectively. Each cell demonstrated satisfactory

capacity retention of around 70%, showcasing the synergistic effect of porous structures and doped nitrogen atoms in the NCs on mitigating the shuttle effect and enhancing the cycling performance. Subsequent evaluations of the rate capabilities of the S/NC cathodes involved cycling the cells at different current densities. Figure 2-8 (d) shows that the S/NC800 displayed superior rate performance relative to the other samples. The S/NC800 delivered an initial discharge capacity of 1410 mAh g^{-1} at 0.1 C. With increases in current rates to 0.2, 0.5, and 1C, the reversible discharge capacities correspondingly reduced to 786, 672, and 563 mAh g^{-1}. Remarkably, even at a high rate of 2C, the S/NC800 maintained the highest specific capacity of 497 mAh g^{-1} among all the samples. Upon reverting the current density to 0.1C, the specific capacity of the S/NC800 cathode was restored to 740 mAh g^{-1}, indicating its robust stability and exceptional performance across a range of operational conditions. Furthermore, the coulombic efficiency of all cells consistently remained close to 100%, further evidencing the effective mitigation of the shuttle effect. This is noteworthy, as the shuttle effect can lead to severe overcharging and diminished coulombic efficiency during cell cycling. Maintaining coulombic efficiency around 100% under all cycling conditions also underscores the synergy between the hierarchical porous structures and nitrogen atoms doping. This combination plays a crucial role in stabilizing the electrochemical reactions, thereby enhancing the overall performance and reliability of the Li-S battery technology.

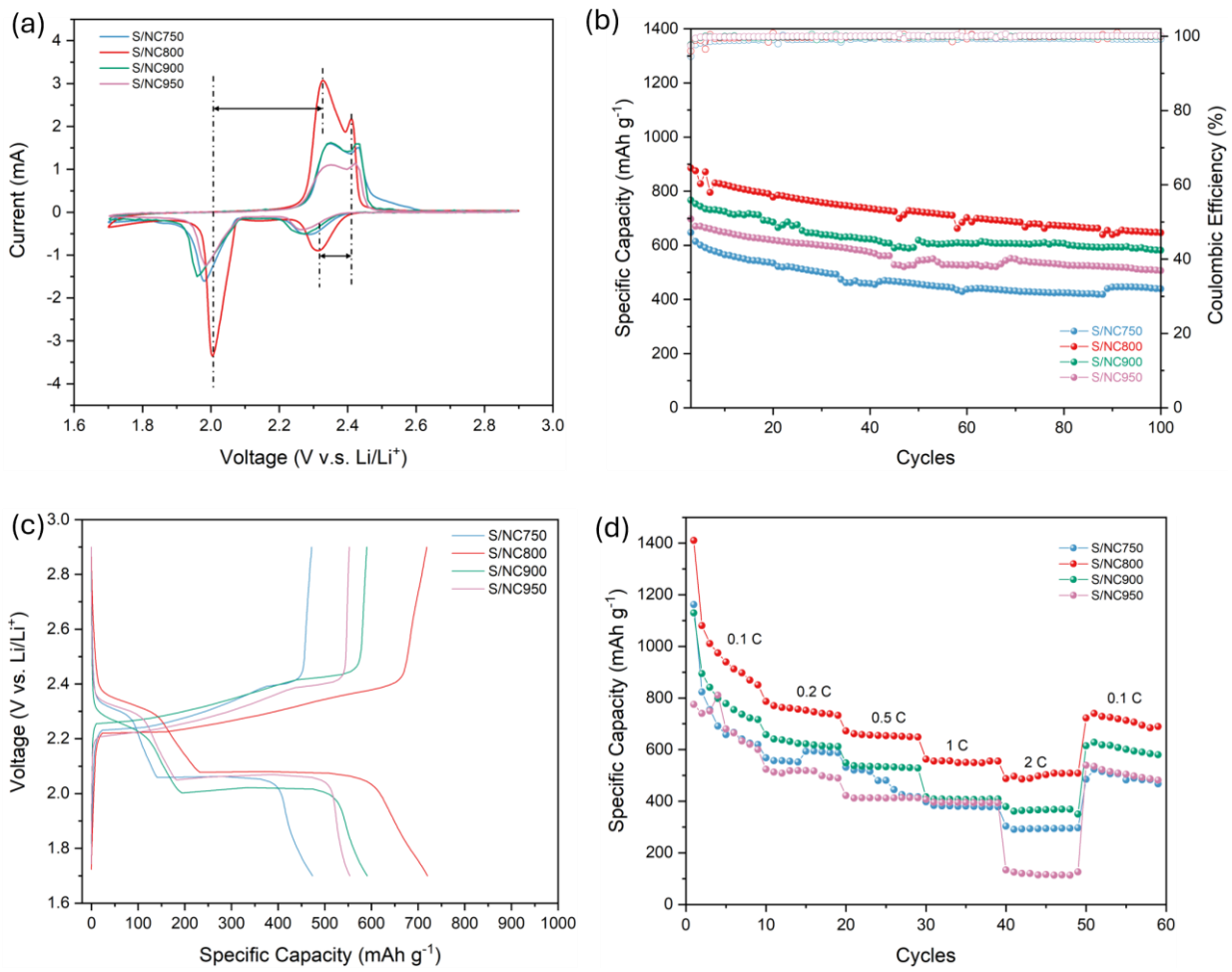

Figure 2- 8. (a) Cyclic voltammetry curves scanned at 0.1 mV s^{-1}, (b) Cycling performance and Coulombic Efficiency at 0.5 C; (c) Corresponding Galvanostatic charge/discharge curves; (d) Rate capabilities at different C-rates of S/NC750, S/NC800, S/NC900, and S/NC950 composite cathodes.

Electrochemical impedance spectroscopy (EIS) was performed on both fresh cells and cells after ten cycles to investigate the charge transfer resistance at the interface between the electrode and electrolyte. The Nyquist plots of the fresh cells, shown in Figure 2-9 (a), reveal a distinctive depressed semicircle in the high frequency region and an inclined line at low frequencies, which are interpreted using the equivalent circuit depicted in the inset of the figure. In the circuit, R_e represents the resistance of the electrolyte, while R_{ct} denotes the charge transfer resistance at the interface between conductive materials and electrolytes.[118] Among the plots of all the cells, the one with the S/NC800 cathode exhibited the lowest R_{ct} value of 24.89 **Ω**, indicating a significantly lower charge transfer resistance than other S/NCs cathodes. This enhanced interface performance is critical for improving the overall electrochemical behavior of the cell, facilitating faster and more efficient ion transfer during cycling. As shown in Figure 2-9 (b), the Nyquist plots of the cycled batteries exhibit two semicircles followed by a sloping line. These two depressed semicircles correspond to different electrochemical processes: the one located in the high-frequency region represents the formation of Li_2S_2/Li_2S film on cathode, and the other one in the middle-frequency region corresponds to the resistance of charge transfer. In the equivalent circuit shown in the inset, these behaviors are denoted as the R_g and R_{ct}, respectively.[118] The values for R_g, R_e, and R_{ct} are listed in Table. 2-2. The battery employing the S/NC800 cathode demonstrates the most favorable resistance values of 22.04 **Ω** and 21.62 **Ω** for R_{ct} and R_g, respectively. These low resistance values indicate improved charge transfer efficiency and the large specific surface area of the NC800 matrix, which facilitates the formation of a thin Li_2S_2/Li_2S film on the cathode. This configuration enhances the overall performance and stability of the battery, particularly in maintaining efficient ion transfer and reducing energy loss during cycling.

The distribution of relaxation of time (DRT) analysis is a method to deconvolute the EIS data, which is a function of frequency, into a time domain function.[127] This technique offers a deeper representation of the complex, overlapping electrochemical behaviors within a system by delineating changes in the relaxation time or the rate constants associated with each process. In the DRT plot, each peak distinctly represents a specific physical or chemical process, thereby providing a clearer insight into the reactions occurring within the system. This enables a more detailed understanding of the underlying electrochemical mechanisms. The corresponding DRT plots are shown in Figure 2-9 (c) and (d) are consistent with the equivalent circuit fittings. Figure 2-9 (c), which presents the DRT of fresh cells, shows that there is only one dominate peak at time of seconds in the cells before discharge. The peak at that time range represented a relation and diffusion process.[128] The cell with S/N800 had the lowest resistance among the four different carbons, which demonstrated the best sulfur distribution within the carbon matrix. This could be simply due to the preferred pore distribution and/or the synergistic effects with a chemical interaction between sulfur and nitrogen functional groups. It is noteworthy that the conductivity of N800 is significantly lower than that of N900 and N950, as listed in Table 2-3. This increasing trend in conductivity with the carbonization temperatures is rational, considering that carbon becomes more graphitized as the increase of heating temperature. Therefore, the low resistance observed at the second time scale is not due to electrical resistance. After 10 cycles, the DRT profile becomes more complex, as shown in Figure 2-9 (d), owing to the multiple sulfur reduction, sulfide dissolution, oxidation and redeposition. The peaks in a microsecond and a millisecond range started to emerge, which could represent the solid electrolyte interphase, double-layer and charge transfer processes at the electrode interface. The S/N800 electrode showed low resistance in all categories, which was speculated to be the consequence of the

possible catalytic effect of NC800 to the sulfur redox reaction and induce a homogeneous distribution of sulfide compounds deposition on the host carbon material. Therefore, the cell with NC800 as the matrix carbon is able to better mitigate the shuttle effect and present a good cycling performance.

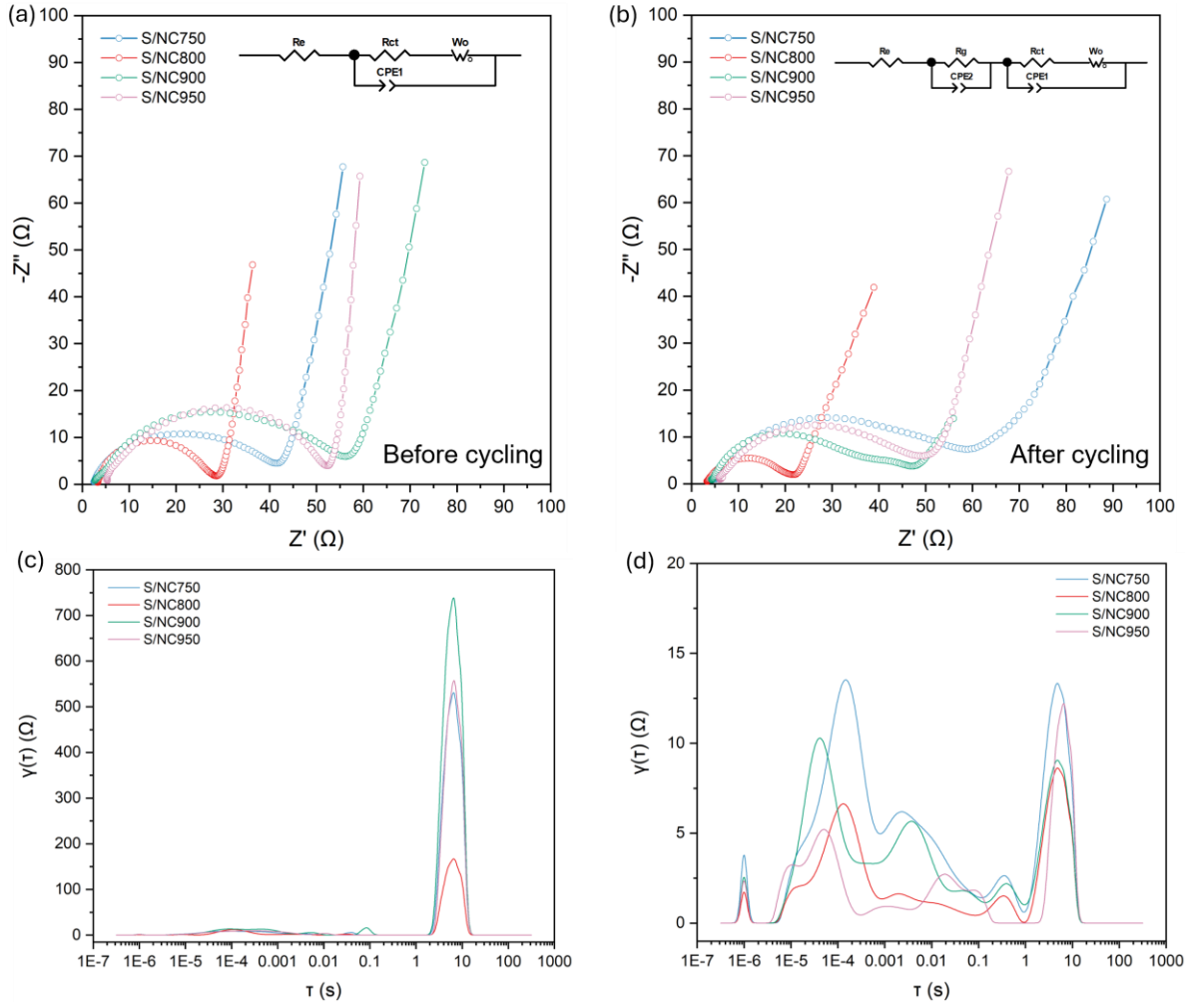

Figure 2- 9. Nyquist plots of batteries with different NCs tested (a) before cycling, and (b) after 10 cycles with corresponding equivalent circuits inset; Corresponding DRT of (c) before cycling, and (d) after 10 cycles

Table 2- 3. R_e, R_g, and R_{ct} values of cells with S/NC750, S/NC800, S/NC900, and S/NC950 cathodes after 10 cycles; conductivities of different NCs.

Sample	R_e (Ω)	R_g (Ω)	R_{ct} (Ω)	Conductivity (mS cm^{-1})
NC750	40.05	52.04	37.81	16
NC800	24.89	21.62	22.04	18
NC900	57.39	40.71	25.32	42
NC950	41.61	41.65	31.17	86

To further demonstrate the hypothesis, the morphologies of the discharge electrodes were captured through SEM to observe the distribution of final discharge products. The results are presented in Figure 2-10 (a)-(d). While the grape-shaped lithium sulfide deposits were observed on the carbon hosts of NC750, NC900, and NC950, a smooth deposition of sulfides was formed on NC800, resembling a "honey-filled honeycomb". The more uniform distribution of Li_2S/Li_2S_2 on S/N800 compared to other NCs indicated a more homogeneous conversion process from S_8 to Li_2S/Li_2S_2 on the surface. These morphological changes may be ascribed to the polarity of the special N-containing functional groups formed on the surface of NCs. It is speculated that NC800 possesses a higher density of N-contained functional groups with higher polarity, evenly distributed on its surface. This results in more nucleation sites for Li_2S/Li_2S_2, which are favorable to the electrochemical performance of the battery.

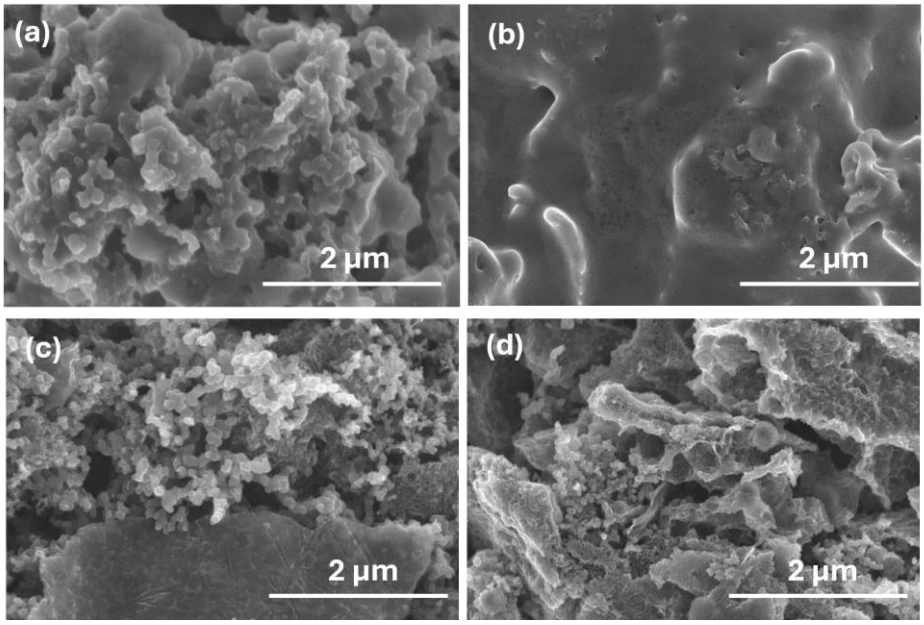

Figure 2- 10. FESEM images of the discharged electrodes with (a) S/NC750, (b) S/NC800, (c) S/NC900, and (d) S/NC950 cathodes.

We conducted a color change experiment to dig deeper into the interactions between NCs and long-chain lithium PS. In this experiment, different carbon hosts were introduced into the polysulfide solutions to observe any resultant color change. The polysulfide mixtures with 5 mM Li_2S_6 were prepared by mixing S_8 and Li_2S in a 1:1 volume ratio of DME/DOL solvent. Equal amounts of different NC samples were added to these mixtures and allowed to rest for 24 h. For comparative purposes, SuperC65 was also tested. As shown in Figure 2-11, the blank solution with 5 mM Li_2S_6 initially displayed a green color due to the low concentration of polysulfides and a relatively high content of S_4^{2-} anions. After resting for 24 h, the color of the baseline mixture remained unchanged, whereas the solutions containing NCs faded to a lighter color, especially the solution with NC750 and NC800, which became almost transparent. This phenomenon can be attributed to the simple physical adsorption of PS in the porous structures of NCs. However, the solution with SuperC65 retained its original green color, similar to the baseline. The lack of functional groups on the SuperC65 surface suggests that minimal physical adsorption occurs, and thus, the PS concentration in the solution remains unchanged. The pronounced color change of NC-added solutions indicates significant interactions between the NCs and the PS in the electrolyte. These interactions likely alter the concentration and distribution of the PS anion species in the mixtures. The results from this experiment highlight that the presence of NCs not only enables the physical adsorption of PS but also facilitates their redox reactions to either elemental sulfur or lithium disulfide and lithium sulfides, which is called a disproportionation reaction. In addition, the almost transparent appearance of the PS solution containing the NC800 sample underscores its superior ability to mitigate the shuttle effect of PS species. This observation aligns with the enhanced electrochemical performance of its sulfur composite cathode compared to the other NC samples.

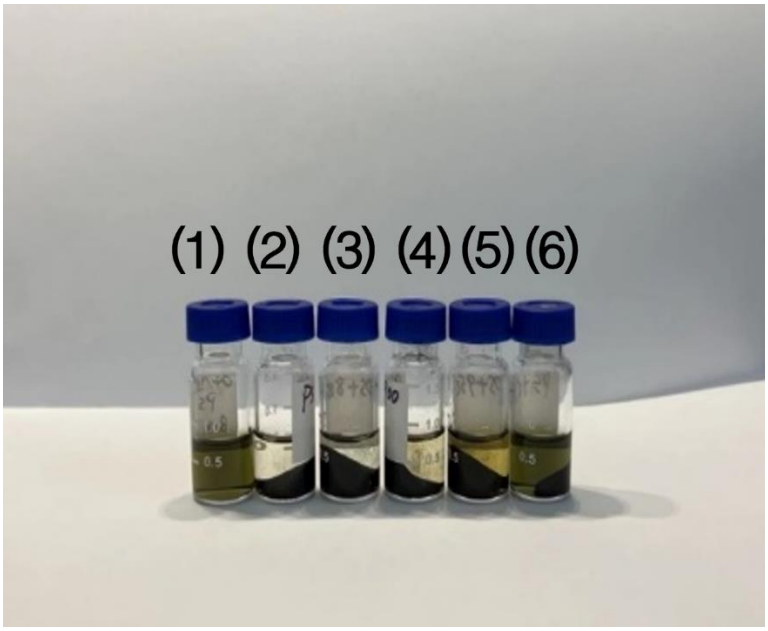

Figure 2- 11. Color changes of 5 mM Li_2S_6 solution solutions with different carbon samples of (1) baseline (without carbon sample), (2) NC750, (3) NC800, (4) NC900, (5) NC950, and (6) SuperC65.

Based on the characterizations above, NC800 demonstrates higher porosity, increased nitrogen content, and enhanced capability to facilitate the redox reactions of PS in the electrolyte compared to other NC samples. These superior properties contribute significantly to the excellent electrochemical performance of its composite with sulfur. Consequently, NC800 was selected as the preferred carbon host for further studies on the cycling performance of sulfur cathodes. To further highlight the superior electrochemical performance of the S/NC800 cathode, KB, an electroactive carbon black, was chosen for comparison. KB is widely utilized in Li-S batteries as a host material for sulfur cathodes due to its high conductivity and specific surface area, which aid in the adsorption of PS species during cycling. The sulfur content in both S/NC800 and S/KB composites was 60 wt%, representing 51 wt% of the total cathode composition. The cells were formed at a low current rate of 0.05 C for two cycles and then cycled at 0.5 C for 200 cycles. As shown in Figure 2-12 (a), the cycling results reveal that both cathodes exhibited an initial specific capacity of around 715 mAh g^{-1} after formation cycles. The S/KB cell experienced a rapid capacity decay over the following decades of cycles and exhibited a capacity retention of 62.7%. In contrast, the S/NC800 cell remained stable over 200 cycles, delivering a superior capacity retention of 84%. The charge/discharge curves of both cells during the formation cycle and the 50^{th} cycle are shown in Figure 2-12 (b). The cell with the S/NC800 cathode exhibits lower polarization, as evidenced by the reduced gap between the discharge and charge plateaus, indicating higher energy efficiency compared to the S/KB cells. This reduced polarization is indicative of a more reversible redox process with less active material during the battery cycling. These findings further substantiate the superior capability of NC800 to mitigate the shuttle effect and enhance the cyclability of Li-S batteries. By effectively reducing polarization, NC800

improves the overall electrochemical stability and efficiency of the battery, which is crucial for achieving long cycle life and high performance in practical applications.

$LiNO_3$ is a commonly used electrolyte additive in Li-S batteries due to its ability to alleviate the shuttle effect by contributing to the formation of a stable passivation layer on the lithium anode, known as the solid electrolyte interphase (SEI). This layer acts as a physical barrier, preventing direct contact between the lithium PS and lithium anode, thereby protecting the anode from corrosion. To further investigate the capability of NC800 in preventing the migration of lithium PS, coin cells with an electrolyte without $LiNO_3$ were examined. For comparative analysis, coin cells with KB as the host material for the sulfur cathode were also tested under the same conditions. The cycling performance and charge/discharge curves of the two cells are displayed in Figure 2-12 (c) and (d). In scenarios where the shuttle effect is present, a significantly large coulombic efficiency (CE), which is greatly over 100%, is observed. Because of the charge status of Li-S batteries after being assembled, the CE here is defined as the ratio of the amount of charge that can be put into the battery during charge to the amount of charge extracted during discharge. The extremely high CE typically results from the shuttle effect of polysulfides, which prevents the active material from being fully recharged, leading to overcharging of the battery. The cell with the S/NC800 cathode exhibited an acceptable CE of 103% compared to the S/KB cell, which exhibited CE of 123%. In addition, the S/NC800 cell demonstrated superior capacity retention compared to the S/KB cell, as depicted in Figure 2-12 (c), further underscoring the enhanced capability of NC800 to impede the transportation of high-order lithium polysulfides.

The extended cycling performance of the S/NC800 composite cathode, which incorporates a high sulfur content, was thoroughly evaluated. The cell was initially activated at a

low current rate of 0.1 C for two cycles and subsequently cycled at 0.2 C for a total of 500 cycles. During the first activation cycle, the composite demonstrated a notable discharge capacity of 1195 mAh g^{-1}, accompanied by a high initial coulombic efficiency of 94%. As illustrated in Figure 2-12(e), even with an increase in the sulfur content of the composite to 80 wt%, which corresponds to 68 wt% of the total cathode mass, the S/NC800 cathode maintained stable cyclability over 500 cycles. The capacity decline observed in the initial 70 cycles can be attributed to the loss of excess sulfur that had crystallized on the external surfaces of the NC800 matrix, a phenomenon likely exacerbated by the high electrolyte content in the coin cell. In the subsequent 400 cycles, the S/NC800 cathode showed minimal capacity decay, with a rate of only 0.0428% per cycle. This outstanding performance underscores the effectiveness of the synergistic integration of hierarchical porous structures and nitrogen doping in NC800. These features significantly enhance the cycling stability and overall performance of the cathode, demonstrating the potential of NC800 as a superior host material for high-loading sulfur cathodes in Li-S batteries.

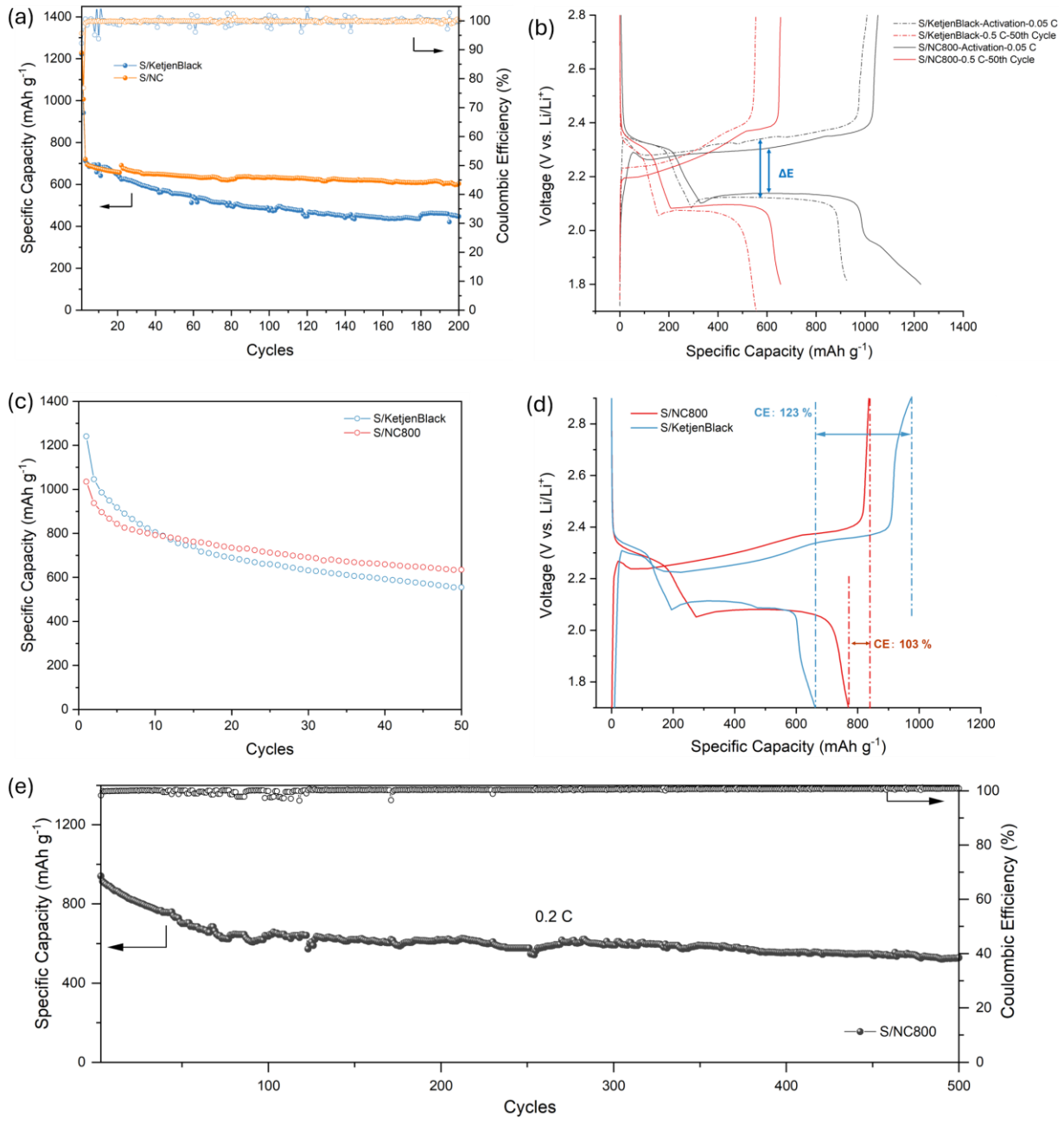

Figure 2- 12. (a) Cycling performance and CE of S/NC800 and S/KB at 0.5 C, and (b) corresponding charge-discharge curves; (c) Cycling performance and (d) corresponding charge-discharge curves of cells without adding $LiNO_3$ additives in electrolyte; (e) Cycling performance of S/NC800 composite with 80wt% sulfur at the C-rate of 0.2 C.

2.4 Conclusions

This study introduces a novel carbon host material for sulfur cathodes of Li-S batteries, developed by carbonizing degummed natural silk at different temperatures. The resultant carbon, designated as NC, exhibits a hierarchical porous structure. In addition, the nitrogen atoms inherently present the amino acids of natural silk are retained within the carbon structure after the carbonization process, simplifying the process by eliminating the need for additional heteroatoms doping. These NCs are adept at encapsulating sulfur and facilitating the disproportionation of dissolved long-chain polysulfide ions into elemental sulfur, lithium disulfide, and lithium sulfide, effectively mitigating the shuttle-effect both physically and chemically during the cycling process of the battery.

Among the different carbonization temperatures tested, the material produced at 800°C, referred to as NC800, features a porous honeycomb structure with the highest porosity and nitrogen content. Its sulfur composite demonstrates superior electrochemical performance relative to other S/NCs cathodes. Notably, it displays a high capacity retention rate of 84% after 200 cycles at 0.5 C. Even with a higher sulfur ratio in the composite, the cell can still deliver a good cyclability over 500 cycles with 0.2 C.

Overall, this research highlights a promising strategy for designing high-performance Li-S batteries with improved cycle life and minimal shuttle effect. By optimizing the unique properties of the carbonized silk-derived material, this approach offers a sustainable and efficient pathway to further enhance the performance of energy storage devices and to systematically understand the fundamental mechanism of Li-S batteries in future.

CHAPTER 3. INVESTIGATION OF THE DISPROPORTIONATION MECHANISMS THROUGH HPLC AND ELECTROCHEMICAL ANALYSIS

3.1 Introduction

The high theoretical capacity of Li-S batteries originates from multiple electron transfers and chemical interactions across different phases. A significant challenge in the performance of Li-S batteries is posed by the intermediates produced during these reactions, specifically the high-order polysulfides. Their high solubility in the commonly used organic ether-based electrolyte enables them to shuttle back and forth between the sulfur cathode and lithium anode, causing the shuttle effect. This shuttling facilitates parasitic reactions that lead to the consumption of active materials, corrosion of the lithium anode, and ultimately, reduced coulombic efficiency of the batteries.[129] To solve these issues, previous efforts focused on restraining dissolved polysulfides within a cathode host matrix to prevent their diffusion to the Li anode, thereby triggering polysulfide shuttle. Unfortunately, the weak Van der Waals forces in physical adsorption proved insufficient to prevent dissolved polysulfides from diffusing into the electrolyte and further to the Li anode. This inadequacy arises from the non-polar carbon surface's inability to bind polar and ionic polysulfide ions, leading to their inevitable dissolution into the electrolyte.

The catalytic acceleration of the conversion of dissolved polysulfides to solid Li_2S_2 during charge/discharge or to S_8 has gained widespread acceptance. Extensive research has been conducted over many years on electrocatalytic sulfur redox reactions, examining both indirect and direct evidence of catalytic involvement in sulfur redox reactions.[130] Introducing a catalyst aims to enhance the slow kinetics involved in the reduction and oxidation processes of polysulfide ions, leading to the formation of Li_2S_2 and S_8, respectively. Accelerating the

conversion of polysulfide ions into solid products serves to minimize the residence time of polysulfide ions in the electrolyte, thereby mitigating the shuttle effect. Therefore, many studies have focused on catalyzing the rapid conversion of polysulfides to expedite the sulfur redox reaction, particularly in facilitating the charge transfer reaction involving non-soluble low-order Li sulfide compounds like Li_2S and Li_2S_2.[130] For instance, homogeneous catalysts such as CoPc have been employed to selectively catalyze the reduction of long-chain polysulfide ions. This is theorized to occur due to the strong adsorption of $Co^{III}Pc$ to the long chain polysulfides at higher potentials.[131]

Initially, catalysts composed of metals and metal oxides, such as Pt, Ni, MnO2, and TiO_2, were identified as effective in accelerating the redox reaction of polysulfides by facilitating charge transfer.[132] Subsequent investigations expanded the scope to include a variety of catalysts, encompassing metal sulfides, metal selenides, metal nitrides, metal phosphides, metal borides, and metal carbides. Additionally, nonmetallic catalysts were explored for their potential role in catalyzing the sulfur redox reaction, and comprehensive reviews have been conducted on these research activities.[133,134] While this approach may enhance the rate capability of a sulfur cathode, its effectiveness in mitigating the shuttle effect is limited. The previous works from our group have proved that the mechanism underlying sulfur redox reactions involves a series of low activation disproportionation steps, leading to a rapid attainment of equilibrium for polysulfides.[135,136] The high solubility of polysulfide ions, coupled with the low activation energy for the chemical equilibrium among polysulfides of varying chain lengths and the reversible nature of the redox reaction of dissolved polysulfide ions, diminishes the positive impact of the limited anchoring site.[137] Additionally, since polysulfide ions exhibit high

solubility, the heterogenous catalytic reaction, especially at high rates, is eventually constrained by diffusion control.

In Chapter 2, a novel carbon host designated as NC800 was synthesized using natural silk as the precursor. This innovative process resulted in a carbon material characterized by a superior hierarchical porous structure and presence of nitrogen-contained functional groups on its surface. When applied in the S/NC800 cathode, this material demonstrated enhanced electrochemical performance compared to other sulfur cathodes that utilize merely porous carbon as their matrix. The remarkable cycling performance of the NC800 is hypothesized to be attributed to the catalyzed disproportionation reactions of polysulfides by the NC host, as suggested by results from the color change experiment. To further substantiate this conclusion, it is crucial to investigate the transformation process of polysulfides within Li-S batteries during cycling. Understanding these transformations in detail will provide critical insights into the mechanistic actions facilitated by the NC800 material.

Despite their significant role in the functionality and degradation of Li-S batteries, the specific mechanisms underlying the sulfur redox reactions within the electrolyte during battery cycling are insufficient. This is because the equilibrium of polysulfide species in the electrolyte is complicated. Their stability depends on their solubility, concentration, and the component of electrolyte. This gap in knowledge hinders the further development of Li-S batteries with more stable performance and higher efficiency. Therefore, further research into these mechanisms is essential for advancing the understanding of Li-S battery technology and improvement of its performance, particularly in terms of mitigating the shuttle effect. Ultraviolet-visible (UV-Vis) spectroscopy is an analytical method that was initially employed to study the change in polysulfides within the electrolyte during battery cycling.[138] This method operates based on

measuring the absorbance or transmittance of light by a simple in the ultraviolet to visible range of the electromagnetic spectrum. Polysulfides are known to exhibit different colors depending on their chain lengths. The color transits gradually from red to green as the chain lengths decrease, corresponding to wavelengths ranging from 600 to 500 nm. Utilizing this principle, the transformation of polysulfide species can be monitored during the discharge and charge process of the Li-S battery. Moreover, it has been demonstrated that the absorption intensity of catholyte solutions, containing the same types of polysulfide species, is linearly related to the natural logarithm of their concentrations.[138] Therefore, UV-Vis spectroscopy can be employed in an operando mode to both qualitatively and quantitatively determine polysulfide species during battery operation.

Although UV-Vis spectroscopy is widely used for real-time analysis of dynamic chemical changes in Li-S batteries, its effectiveness is somewhat limited by the overlap of absorbance peaks of some polysulfide species, making it complicate to distinguish between different polysulfides based solely on the UV-Vis spectra. In addition, the quantification is also hard to realize because of the lack of adequate polysulfide standards. To overcome these issues and enhance analytical precision, it is essential to isolate single polysulfide with different chain lengths. High performance liquid chromatography (HPLC) is a powerful and versatile technique used for separating molecules in a liquid mobile phase by passing them through a solid stationary phase under high pressure. Components are separated based on their interactions with the stationary phase.[139] Particularly, reverse-phase HPLC coupled with electrospray-mass spectroscopy (ESI/MS) has been reported to effectively separate and detect polysulfide species formed during the cycling.[140] However, the separation of polysulfides in the electrolyte poses challenges due to the suitability of reverse-phase HPLC primarily for covalent compounds and

the higher concentration of $TFSI^-$ of salt in electrolyte, which can render polysulfide anions undetectable.[141] An effective solution to these issues involves the derivatization of polysulfide, transforming unstable polysulfides anions into more stable alkyl polysulfides, as shown in equation 3-1. This transformation allows the derivatized polysulfides to be retained and separated on a reverse-phase HPLC column for further analysis. A notable derivatization agent of 4-(dimethylamino) benzoyl chloride, as shown in equation 3-2, as reported by Zheng and co-workers, has demonstrated a good separation of polysulfides on reverse-phase HPLC.[141] When coupled with ESI/MS, this technique enables the unique identification polysulfide species by their retention times on the column. This advanced analytical technique has been applied to further investigate the redox mechanisms at the sulfur cathode and monitor real-time changes in sulfur and polysulfides species within the battery system during cycling.[135,136]

$$2RX + S_n^{2-} \rightarrow RS_nR + 2X^- \quad (3\text{-}1)$$

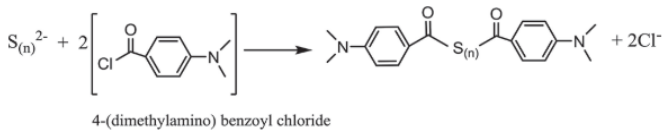

4-(dimethylamino) benzoyl chloride

(3-2)[141]

In this chapter, we explore the interactions between polysulfides and the NC carbon host, assessing these relationships both qualitatively and quantitatively using HPLC method. To provide a comprehensive analysis, the interactions of polysulfides with other materials such as various commercial carbons and metal oxides are also examined, highlighting the distinctive properties of NC. Additionally, to investigate the specific mechanisms of these interactions, electrochemical analysis techniques such as EIS and CV are also applied.

3.2 Experiments

Chemicals

Sulfur (S_8), lithium nitrate ($LiNO_3$), HPLC grade methanol, HPLC grade isopropanol, HPLC grade water, methyl triflate, and lithium metal (from Sigma Aldrich), dimethoxyethane (DME), 1,3-dioxlane (DOL), lithium bis(trifluoromethane) sulfonimide (LiTFSi) (battery grade from FERRO), and PTFE condensed liquid binder (60% from MTI Corporation) were purchased and used without further treatment.

Carbon that was used in the experiment are Vulcan XC72, Bucky Paper, HPG, Carbon Cloth, Carbon Paper, Glassy Carbon, Carbon Nanotube, Graphene C500, Graphene C600, KB600, BP2000, CMK-3, M20, SX-UL, and NC. Inorganic materials are Cu_2S, MnO_2, NiO, SeS_2, SiO_2, MnO, ZnO, SnO_2, Ag_2S, and FeS_2.

Induced disproportionation experiment

PS mixtures used in this work were 5 mM Li_2S_6 and 25 mM Li_2S_6 in DME/DOL (1:1, vol%). S_8 and Li_2S were mixing in the molar ratio of 5: 8 and 7:8 respectively to form Li_2S_6 and Li_2S_8 stoichiometrically in the mixture of DOL/DME. The solutions were stirring for 24 h at 60 °C in an Ar-filled glovebox.

The induced disproportionation tests were conducted by adding 10 mg of different carbon samples into the sample vials (with air-tight caps) with 1.0 mL polysulfide solution. After stirring the polysulfide solutions with different carbon samples for 24 h, a specific amount of the PS solutions was taken and derivatized with methyl triflate in air-tight HPLC sample vials before being taken out of the glovebox for HPLC analysis. The S/NC800 and S/KB pouch cells were disassembled after cycling for 3 cycles and the electrolytes remaining on the separators were

taken out and derivatized with methyl triflate. The obtained samples were also analyzed by using the HPLC technique to determine the distribution of PS in the electrolyte recovered from the cycled pouch cells.

Absorption experiments

The solution of polysulfides used in the absorption tests was 15 mM Li_2S_8 in DME/DOL (1:1, vol). This solution was obtained by mixing S_8 and Li_2S (molar ratio of 7:8 to form Li2S8 stoichiometrically) in the mixture of DME/DOL, and the solution was stirring for 48 h at room temperature in an Ar- filled glovebox. The absorption tests were conducted by mixing 15 mg of each host material with 1.0 mL of the polysulfide solution in an airtight sample vial. After stirring the polysulfide mixtures with different host materials for 24 h at room temperature, a specific amount of the polysulfide solutions was taken and derivatized with methyl triflate in airtight HPLC sample vials before being taken out of the glovebox for the HPLC analysis.

In-situ three-electrode Li-S cell and AC impedance analysis

S/NC and S/SuperC65 electrodes were prepared using identical procedures for comparison. The composites were synthesized by heating a mixture of carbon hosts (NC or SuperC65, sourced from Timcal) and elemental sulfur in a sealed glass tube at 155 ^{o}C for 12 hours. The resulting composites were then used as the active materials for the electrode. To prepare the electrodes, 85 wt% of the active materials was mixed with 5 wt% of the PTFE, which acted as binder, and 10 wt% of conductive agent. This mixture was then rolled into a thin film electrode with a thickness of 100 µm. Finally, the film was cut into a 2 cm × 2cm rectangle with a sulfur loading of 10 mg. The resulting film was then laminated onto an alumina film to serve as the working electrode.

The 3-electrode Li−S cells were assembled in a 25 mL four-necked round-bottom flask. The cathode comprised the previously prepared sulfur/carbon thin film electrodes as working electrodes, while the counter electrode and the reference electrode consisted of lithium metal. A 15 mL electrolyte solution of 1.0 M LiTFSi/DME/DOL (1:1 volume ratio) with 0.2 M $LiNO_3$ was employed to the cell. To mitigate concentration and diffusion polarizations arising from the limitation area of cathodes and the high volume of electrolytes, all cells were stirred and cycled at 0.06 mA (approximately C/200) using a PARSTAT 2273 advanced electrochemical system from Princeton Applied Research.

The fourth neck of the flask was designated as a sampling port for real-time HPLC analysis. AC impedance measurements were conducted using the PARSTAT 2273, covering a frequency range of 0.1 to 100 KHz with an amplitude of 10 mV at open circuit potential, reflecting different cycling statuses.

All procedures, including the electrochemical cycling and sample preparations, were conducted in an argon-filled glovebox with oxygen and moisture contents of less than 0.5 ppm. The catholyte was extracted from the cell at various depths of discharge (DoD) and charge (DoC), then derivatized in an HPLC vial. Subsequently, 75 μL of the electrolyte was extracted from the Li−S cell during operation and added to the DME/methyl triflate solution. The mixture was immediately capped with an airtight cap and vortexed for 5 min. Derivatized electrolyte samples in the sealed HPLC vials were then removed from the glovebox for HPLC analysis.

Derivatization of polysulfides and HPLC analysis

The derivatization of polysulfide solution was obtained by the following process: certain amount of DME and methyl triflate were added into a 2 mL air-tight HPLC sample vial, and the

mixture was vortexed for 1 minute; then 150 μL or 120 μL polysulfide solution was added and vortexed for 2 minutes. Through this derivatization process, the polysulfides (S_n^{2-}) were transferred into $CH_3S_nCH_3$ which were not only stable for HPLC mobile phase condition but also separable according to different chain lengths of sulfur.

A Shimadzu LC-20AD quaternary pump with a Shimadzu SIL-20A autosampler was used to deliver a methanol/water mobile phase through a Shimadzu C18 column (from Shimadzu, C18, 4.6 × 50 mm) at a flow rate of 0.70 mL min^{-1}. The injection volume for the derivatized samples was 5 uL. A binary gradient of mobile phases was used to elute the injected sample out with the following conditions: 25% methanol (75% water) at 0 min; 100% methanol at 10 min; 100% methanol at 25 min; 25% methanol at 26 min. All flow from the HPLC was introduced into the Shimadzu SPD-M20A detector. Full wavelengths ranging from 190 nm to 800 nm were recorded by Shimadzu LabSolutions Lite software, and the chromatograms discussed in this work were replotted from data at 230 nm.

Cycling test at different rate

The cycling test was carried out in CR2032 type coin cells. S/KB and S/SuperC65 cells were used as comparisons. The weight ratios of 7:3 of sulfur and carbon host materials were applied. Electrodes were prepared as the procedures described in Chapter 2. The prepared electrodes were punched into circle with a diameter of ½ in. The cells were assembled in an Ar-filled glovebox with water and oxygen <0.5 ppm. The electrolyte was composed of 1 M lithium LiTFSI dissolved in DOL/DME (1:1 vol%) with 0.4 M $LiNO_3$ as an additive.

Galvanostatic charging/discharging tests, a method of testing the electrochemical performance of cells by applying a constant current, were conducted on an Arbin battery testing system (BT200)

in a voltage window of 1.8~2.9 V vs Li^+/Li at ambient temperature. The tests were conducted at 0.01, 0.05, and 0.5 C (1C = 1675 mA g^{-1}).

3.3 Results and discussion

3.3.1 Adsorption Test and HPLC Analysis

Based on the experimental results of color changes described in Chapter 2, the interactions between the NCs and polysulfides are remarkably different from those between SuperC65 and polysulfides. Unlike the solutions containing SuperC65, which show little to no change in appearance, the introduction of NCs into polysulfide solutions leads to a dramatic change, evidenced by the solutions becoming almost transparent. This significant alteration in the visual appearance of the solutions suggests a change in the distribution and concentration of polysulfides within the system. Since polysulfides anions are known to display distinct colors, the observed transparency indicates active interaction between the NCs and polysulfides. This experimental observation leads to the hypothesis that a disproportionation reaction may be facilitated or catalyzed by the presence of NCs. In such reactions, a single reactant undergoes both oxidation and reduction, producing two different products. Applied to the context of Li-S batteries, it is speculated that the polysulfide anions may be disproportionated by NCs, being oxidized to elemental sulfur and reduced to Li_2S_2/Li_2S. This potential catalytic role of NCs could be critical in stabilizing the electrochemical environment within Li-S batteries, reducing the shuttle effect, and enhancing overall battery efficiency and cycling life.

To further confirm and investigate the mechanisms suggested by the color change experiments, the specific components of the resulting polysulfide mixtures should be clarified.

The mixture solutions were derivatized with a methyl triflate, a common reagent used to transform unstable polysulfide anions of varying chain length into more stable dimethyl polysulfides.[135,141] These derivatized polysulfides were then separated and quantitatively and qualitatively analyzed using HPLC to examine the distribution of polysulfide species within the electrolyte, with the aim to further investigate the reaction of PS induced by the NCs. The corresponding chromatograms of different samples are shown in Figure 3-1 (a). Peaks appearing at 12.1, 13.2, 14.0, 14.7, 15.3, 15.9, and 17.0 min can be attributed to $CH_3S_3CH_3$, $CH_3S_4CH_3$, $CH_3S_5CH_3$, $CH_3S_6CH_3$, $CH_3S_7CH_3$, $CH_3S_8CH_3$, and S_8, respectively. [142] The SuperC65 sample displayed the same patterns as the baseline sample, indicating that SuperC65 did not induce the shift of the chemical equilibrium of the PS species. By comparison, $CH_3S_nCH_3$ (n = 3-8) peaks of the solutions containing NC750, NC800, NC900, and NC950 almost disappeared, while the intensities of elemental sulfur increased drastically, accompanied by changes of the relative ratios of peaks. These results indicate the occurrence of disproportionation of S_n^{2-} induced by the NCs, which transferred most of the dissolved polysulfide anions to S_8. To further analyze the material, the EDS analysis was carried out. The SuperC65 and NC800 in the mixtures were washed with DME to remove any remaining long-chain polysulfides on the carbon before the further EDS measurement. The spectra displayed in Figure 3-1 (e) and (f) show that the sulfur peak appears only in the spectrum of NC800, which could be attributed to the formation of insoluble S_8 and Li_2S_2/Li_2S due to the disproportionation reactions reduced by NC800. Elemental mapping of sulfur, shown in Figure 3-1(g), reveals a uniform distribution of sulfur within NC800. These findings further support the previous conclusion regarding the catalytic activity of NC800.

A similar tendency can also be obtained from the samples with a higher polysulfide concentration of 25 mM Li_2S_6, which are shown in Figure 3-1 (b). Because an insufficient amount of NCs was added to the polysulfides mixture solution, $CH_3S_nCH_3$ (n = 3-8) peaks can still be seen for all NC samples. However, all the NC samples showed higher intensity for S_8 and lower intensity for $CH_3S_nCH_3$ (n = 3-8) peaks compared to the baseline and the mixture with SuperC65. This suggests that all NC can facilitate the disproportionation of PS anions. It is noteworthy that NC800 displayed the lowest intensities for S_8 peak in both sets of measurements. This observation can be attributed to its high porosity, which likely traps more solid S_8 within porous structures, making it undetectable by HPLC. These results can be supported by the HPLC chromatographs of the 10 mM S_8 solutions with different NC samples and SuperC65, as shown in Figure 3-1 (c) and (d). With the same amount of carbon sample added into the solutions, the chromatogram of the one with NC800 displays the lowest peak for S_8, confirming its better ability to physically trap the elemental sulfur.

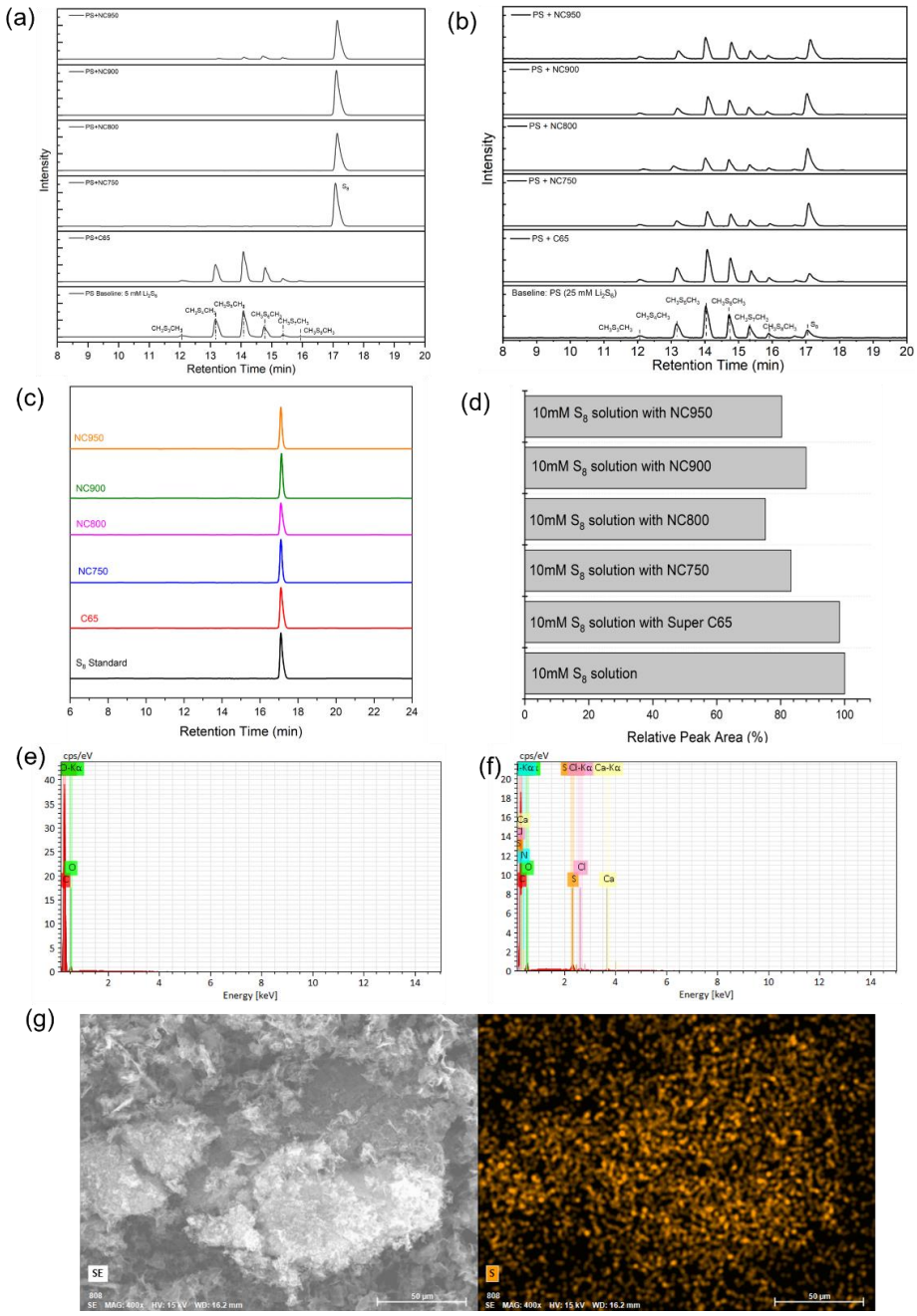

Figure 3-1. HPLC chromatograms of the derivatized (a) 5 mM Li_2S_6 and (b) 25 mM Li_2S_6 solutions with different carbon; (c) S_8 solution with SuperC65, NC750, NC800, NC900, and NC950, and (d) corresponding relative peak areas of each sample; EDS spectrum of washed (e) SuperC65 and (f) NC800 from the resulting polysulfide solutions; (g) SEM image and EDS mapping of S of NC800.

Different with simply physical absorption of polysulfides, the catalytic irreversible chemical reactions that induce by the host materials can not only alter the concentration and distribution of polysulfide in species, but new species could also form accompany with the interactions. Various materials, including carbon materials and inorganic materials, have been reported to have this catalytic function toward the redox reactions of polysulfides and therefore prolong the cycling life of Li-S batteries.[143–146] However, quantitative and qualitative investigation of the interactions of these host materials and polysulfides are still lacked. To compare the catalytic reaction mechanisms between the NC and other materials, including 15 carbon materials and 10 inorganic materials, with polysulfides, we conducted a systematic study based on the HPLC method. All the selected host materials were immersed in the 15 mM Li_2S_8 solution for 24 hours. The resulting solutions were then taken out and their component was tested through HPLC after derivatization.

The resulting chromatographs of various carbon materials are presented in Figure 3-2. The chromatographs of Vulcan XC72, Bucky Paper, HPG, carbon cloth, carbon paper, glassy carbon, and carbon nanofibers, display same patterns with the baseline group, as shown in Figure 3-2 (a). The most abundant peak was assigned to S_5^{2-}. The distributions and intensities of all sulfur contents, encompassing both polysulfides and elemental sulfur, for these seven carbon materials closely matched those found in the original polysulfide solution, with variation in value within a 10% relative range. These observations indicate that there were no significant interactions between these carbon materials and polysulfides in the solution, and the amount of polysulfides absorbed by these carbons was too small to be detected by the HPLC analysis. This lack of interaction and absorption can be attributed to the relatively small specific surface area of these carbon materials and the absence of the functional groups on their surfaces, which are

crucial for enhancing polysulfide adsorption and facilitating the conversions polysulfides as we have proposed previously. The chromatographic analysis of additional carbon materials, including SX-UL, KB600, Graphene C500, Graphene C750, BP2000, CMK-3, M20, and NC, presented in Figure 3-2 (b), reveals substantial interactions with polysulfides, marking a significant deviation from the baseline polysulfide solution. These chromatograms show prominent increases in the intensity of the elemental sulfur peaks, coupled with a corresponding decrease in the peaks of polysulfide anions. This trend is particularly pronounced in the cases of M20 and NC, which the most abundant chromatographic peak is that of S_8, as opposed to the S_5^{2-} peak in the baseline polysulfide solution. The marked increase in elemental sulfur in the chromatograms for those carbon materials suggest that the interactions between polysulfides and these carbon materials may predominantly involve an irreversible disproportionation reaction, with elemental sulfur being one of the reaction products. These reactions emphasize the capability of these carbons to catalyze the transformation of polysulfides into less soluble and more stable forms. The two distinct different behaviors of different types of carbons are further quantified and illustrated in Table 3-1, which lists the normalized chromatographic peak intensities. The values in the table were obtained by normalizing the peak intensity of PS with carbon materials to the peak intensity of baseline. A value of 1 indicates that the abundance of a particular polysulfide or elemental sulfur is equivalent to that in the baseline solution. Values smaller than 1 suggest a reduction in the abundance of these species relative to the baseline, whereas values greater than 1 indicate an increase.

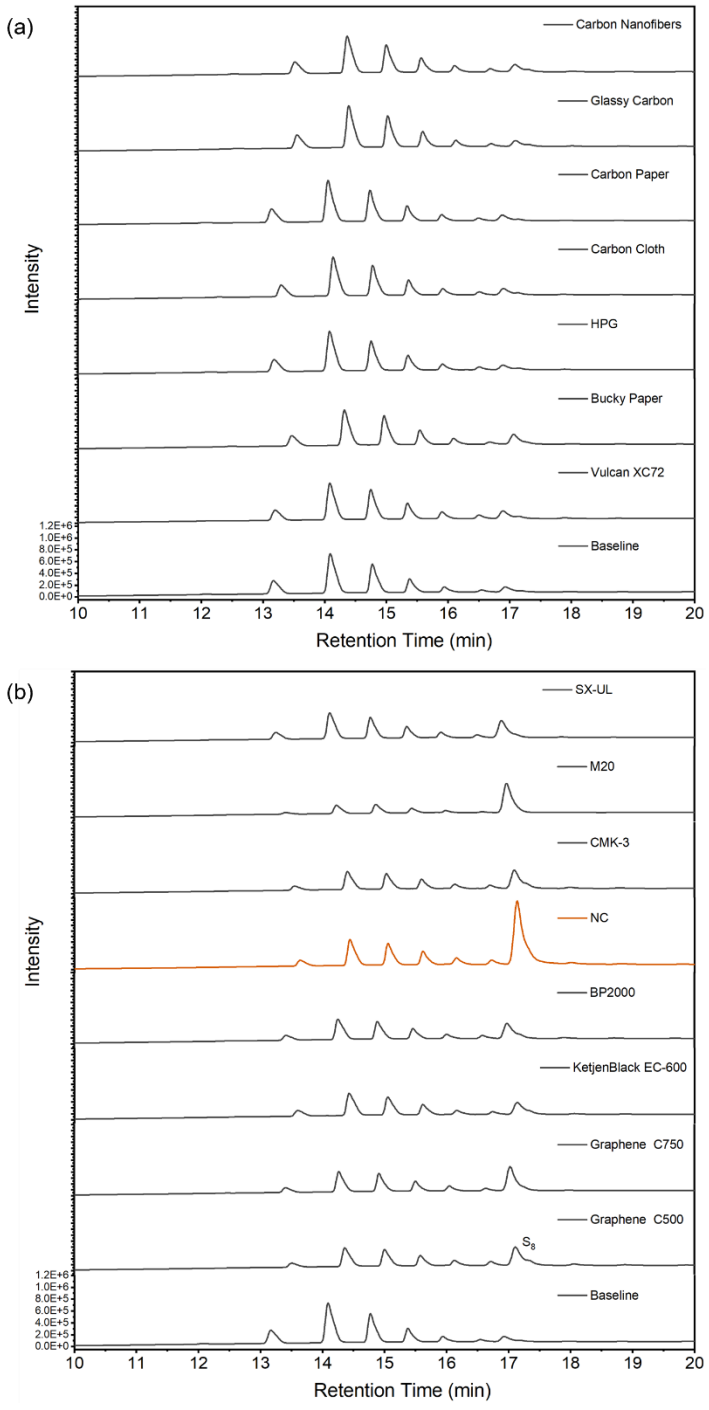

Figure 3-2. HPLC chromatographs of 15 mM polysulfide solution (baseline) and the polysulfide solutions after mixing with (a) Vulcan XC72, Bucky Paper, HPG, carbo cloths, carbon paper, glassy caron, carbon nanofibers, and (b) Graphene C500, Graphene C750, KB600, BP BP2000, NC, CMK-3, M20, and SX-UL.

Table 3-1. Normalized chromatographic peak intensities of carbon materials.

RT(min) / carbon	12.01 S_3^{2-}	13.13 S_4^{2-}	14.06 S_5^{2-}	14.74 S_6^{2-}	15.35 S_7^{2-}	15.91 S_8^{2-}	16.52 S_9^{2-}	16.92 S_8
Baseline	1.0	1.0	1.0	1.0	1.0	1.0	1.0	1.0
Vulcan XC72	0.75	0.76	0.9	1.0	1.1	1.3	1.5	2.1
Bucky Paper	1.0	0.74	0.85	0.98	1.0	1.0	1.03	2.1
HPG	0.96	0.88	0.96	0.99	1.07	1.14	1.31	0.88
Carbon Cloth	1.13	0.98	0.99	1.02	1.05	1.11	1.20	1.04
Carbon Paper	0.88	0.82	0.91	0.98	1.07	1.18	1.4	1.17
Glassy Carbon	1.07	0.94	0.98	1.01	1.05	1.12	1.17	1.03
Carbon Nanotubes	0.95	0.86	0.89	0.92	1.03	1.17	1.41	1.36
Graphene C500	0.25	0.32	0.47	0.59	0.79	1.05	1.82	4.36
Graphene C750	0.51	0.35	0.48	0.60	0.69	0.96	1.11	4.89
KB 600	0.45	0.43	0.58	0.66	0.81	0.88	1.28	2.82
BP2000	0.3	0.37	0.52	0.63	0.78	0.91	1.39	3.47
NC	**0.3**	**0.46**	**0.67**	**0.8**	**1.08**	**1.49**	**2.12**	**14.99**
CMK-3	0.22	0.30	0.44	0.53	0.69	0.84	1.37	3.99
M20	0.36	0.12	0.20	0.30	0.33	0.43	0.44	5.87
SX-UL	0.64	0.50	0.64	0.72	0.84	1.10	1.32	3.76

In addition to carbon materials, various inorganic materials, including both sulfides and oxides were also tested using the same analytical methods to assess their interactions with polysulfides. The HPLC chromatograms of polysulfide solution mixed with these inorganic materials are presented in Figure 3-3. Among the ten inorganic compounds tested, five of them - FeS_2, Ag_2S, SnO_2, ZnO, and MnO – no significant alterations in the chromatographic patterns compared to the original polysulfide solutions. This suggests that these materials do not interact significantly with polysulfides, indicating they lack the necessary properties to catalyze or facilitate significant chemical transformations of polysulfides. On the contrary, the chromatograms of solutions that containing the other five compounds, including SiO_2, SeS_2, NiO, MnO_2, and Cu_2S, revealed prominent alterations in the distribution of polysulfide species and an increase in the intensity of the elemental sulfur peak to varying degrees. These observations suggest that these materials interact more actively with polysulfides, potentially influencing their chemical behavior in several ways. SiO_2 and SeS_2 display great increase in the intensity of the S_8 peak and only a subtle change in the peaks for polysulfide anions. While the chromatographic profiles of these two oxides might visually resemble those of the NC, a closer examination of the normalized peak intensities listed in Table 3-2 reveals a subtle difference. Both SiO_2 and SeS_2 exhibited a slight increase in the intensity of the S_3^{2-} peak, which contrasts with the behavior observed with NC.

An intriguing phenomenon was observed for NiO, MnO_2, and Cu_2S. In the chromatographs of the solution with NiO and MnO_2, only a distinct S_8 peak was observed, and no polysulfide anion peaks were detected. In previous UV-vis studies, MnO_2 was categorized as a strong material for polysulfide adsorption, however, according to the above HPLC results, these transition metal oxides showcase the ability of irreversible oxidized polysulfide into

elemental sulfur instead of merely adsorption.[129] The results obtained by HPLC are consistent with another study on the reaction between polysulfides and MnO_2 in aqueous solution.[147] Another interesting result was obtained from the solution with Cu_2S. Unlike other inorganic materials, it exhibits strong interactions with polysulfides in the solution, as evidenced by the almost undetected peaks in the chromatograph. This result is completely opposite to the one obtained from the UV-vis analysis, which suggested that Cu_2S has weak interactions with polysulfides because of lower absorbance of the Li_2S_6 solution that mixed with Cu_2S of light. UV-vis spectroscopy works by measuring the absorbance of light across the ultraviolet and visible ranges of the electromagnetic spectrum. The absorbance spectrum can provide insights into the concentration and nature of substances in a solution. In the case of Cu_2S, the UV-vis analysis indicated low adsorption of Li_2S_6, implying weak interactions. However, the HPLC chromatograph results suggest a different mechanism than that of MnO_2 and NC, as indicated by the disappearance of the peak for elemental peak. The discrepancy between the results obtained from HPLC and UV-vis analysis can be attributed to the orange precipitates that produced during the derivatization, as shown in Figure 3-4. These precipitates may be attributed to copper/polysulfide complexes. The strong UV absorbance observed in the previous study could also be linked to these compounds. These results further indicate the reliability of HPLC over UV-vis in the qualitative and quantitative studies of interactions between different host materials and polysulfides.

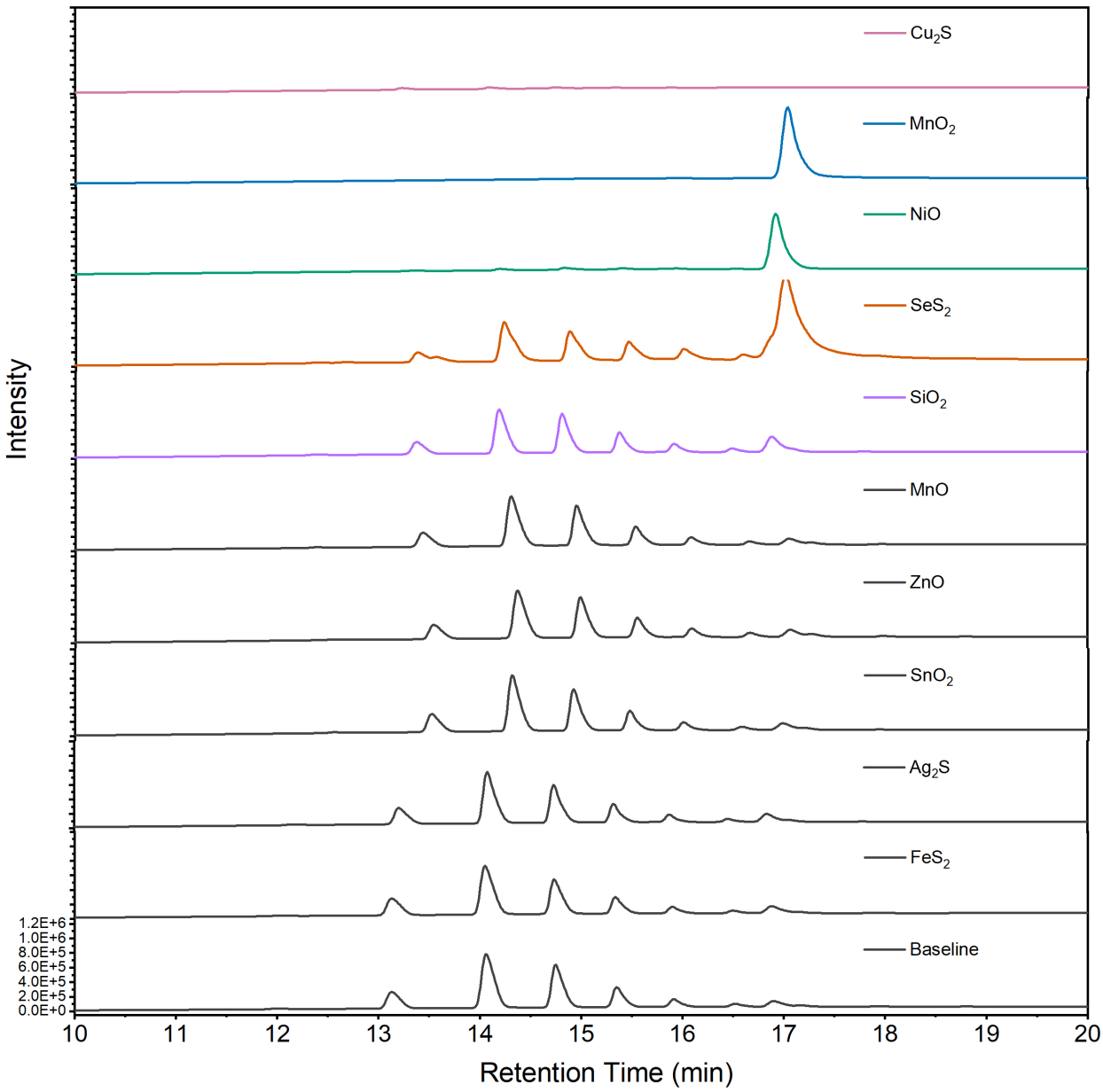

Figure 3-3. HPLC chromatograms of 15 mM polysulfide solution (baseline) and polysulfide solutions after mixing with different sulfides and oxides for 24 h.

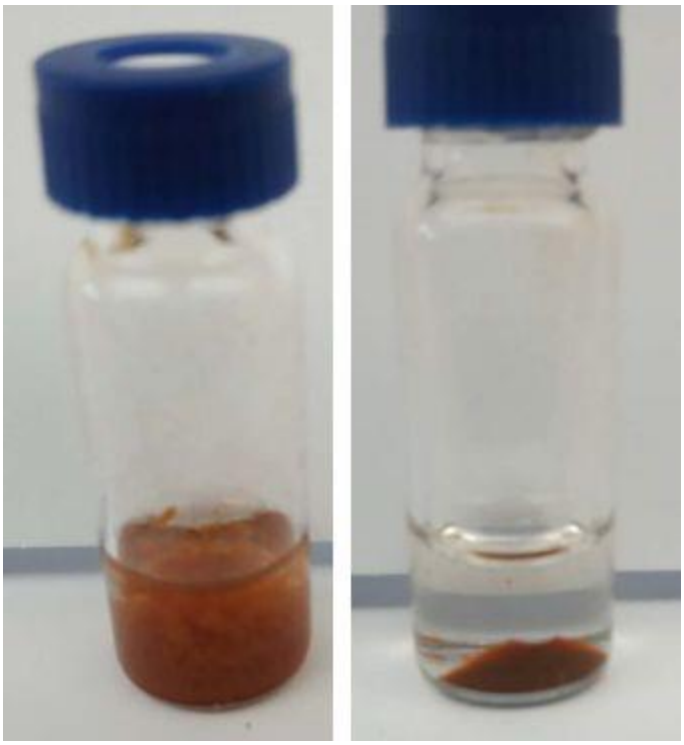

Figure 3-4. The visual observations of the derivatization solution after adding 120 uL solution (without any solid) of polysulfide solution with Cu_2S for one day.

Table 3- 2. Normalized chromatographic peak intensities of inorganic materials.

RT(min) / carbon	12.01 S_3^{2-}	13.13 S_4^{2-}	14.06 S_5^{2-}	14.74 S_6^{2-}	15.35 S_7^{2-}	15.91 S_8^{2-}	16.52 S_9^{2-}	16.92 S_8
Baseline	1.0	1.0	1.0	1.0	1.0	1.0	1.0	1.0
Cu_2S	0.32	0.1	0.03	0.03	0.03	0.03	0.02	0.02
MnO_2	0	0	0	0	0	0	0	12.64
NiO	0	0.03	0.03	0.05	0.06	0.06	0.09	8.85
SeS_2	**2.12**	**0.79**	**0.87**	**0.92**	**1.18**	**1.93**	**1.59**	**22.23**
SiO_2	1.11	0.72	0.82	1.00	1.06	1.14	1.08	2.72
MnO	1.05	0.83	0.96	1.07	1.07	1.13	1.26	0.90
ZnO	0.88	0.83	0.91	1.08	1.13	1.31	1.70	1.04
SnO_2	1.14	1.01	1.04	1.08	1.09	1.16	1.22	1.02
AgS_2	1.07	0.94	0.97	1.00	1.04	1.09	1.13	1.23
FeS_2	1.13	1.0	0.99	0.97	0.98	1.03	1.05	1.15

Based on the experimental evidence shown above, it is worth pointing out that NCs did not act as a catalyst, but rather participated in the sulfur "disproportionation reaction". Evidently, the chemical equilibrium of the PS shifted to the formation of elemental sulfur induced by the NCs. As additional evidence, the degree of the PS reaction depended on the relative amounts of polysulfides and NCs as shown in Figure 3-5 (a) and (b). Although the detailed reaction mechanism was still unclear, the interaction of NCs with PS can be ascribed to their relatively higher nitrogen content on the carbon surface.

This conclusion was further verified by the chromatograms of the derivatized PS mixtures with PWA, which unlike NCs, features only oxygen functional groups on its surface but possesses a similar specific surface area to the NCs. As shown in Figure 3-5 (a) and (b), represented by the green line, the chromatograms of PWA also displayed decreased intensities for $CH_3S_nCH_3$ (n = 3-8) peaks and increased intensity for S_8 peak, though the changes were not as pronounced as those observed in the NCs samples. This suggests that while oxygen functional groups on the carbon surface influence chemical equilibrium of polysulfides, the nitrogen atoms present in the NCs appear to play a more pivotal role in shifting the chemical equilibrium of S_n^{2-} towards elemental sulfur. This finding highlights the unique effectiveness of nitrogen functionalities in enhancing disproportionation of polysulfides, which is key to mitigating the shuttle effect associated with dissolved polysulfides. In addition, due to its relatively low specific surface area and pore volume, NC750 was not able to trap as much sulfur as NC800. Consequently, although NC750 can interact with PS anions chemically and promote the S_n^{2-} transfer into S_8, it still exhibited the lowest specific capacity among all the S/NC cathodes.

HPLC analysis was then employed to determine polysulfide species in the electrolyte during cycling, providing a detailed evaluation of the chemical dynamics within the cells. A

comparative analysis was also conducted using a pouch cell with an S/KB cathode. After three cycles, both pouch cells were disassembled, and the electrolyte was extracted from the separators. This electrolyte was then derivatized using methyl triflate to convert polysulfide anions into more stable dimethyl polysulfides, facilitating a more accurate HPLC analysis. The results of the experiment, as shown in the HPLC chromatographs in Figure 3-5 (c), reveal significant differences in polysulfide components between the two cathode materials. The S/NC800 sample showed a high content of S_8 in the electrolyte and relatively low amount of other high-order polysulfide species. In contrast, the S/KB sample demonstrated a high concentration of various polysulfide chains but lacked any S_8. These findings suggest that NC800 induces the disproportionation reactions of PS to elemental sulfur and Li_2S_2, which reduces the existence time of PS anions in the electrolyte. This alleviation of the shuttle effect results in a lower concentration of PS anions in the electrolyte. The solubility of S_8 in electrolyte is much lower than that of the polysulfide species, hence it can be better absorbed in the porous cathode matrix instead of shuttling to the anode.

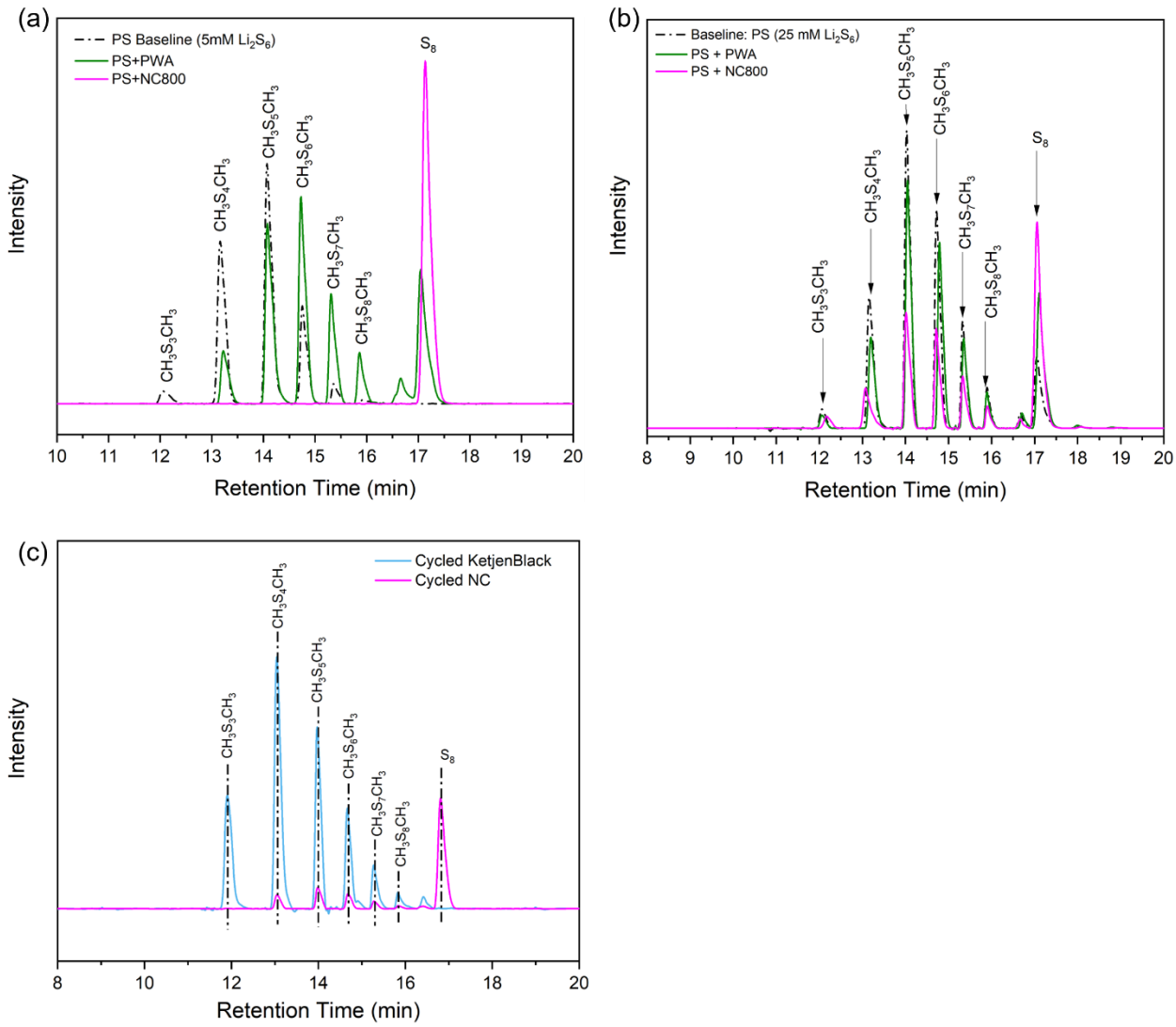

Figure 3-5. HPLC chromatograms of (a) the derivatized 5 mM Li_2S_6 mixtures with NC800 and PWA; (b) the derivatized 25 mM Li_2S_6 solutions with NC800 and PWA; and (c) electrolyte from S/NC800 and S/KB pouch cells after 3 cycles.

3.3.2 Electrochemical Studies of Disproportionation Reactions of NC and Polysulfides

The above HPLC analysis elucidates the properties of NC800 in inducing and facilitating the disproportionation of long-chain PS. Based on these findings, we propose a hypothetical mechanism, which is schematically illustrated in Figure 3-6. We formulated the hypothesis suggesting a pseudo-8-electron redox reaction. Following the initial reduction of S_8 to long-chain lithium PS, high-order polysulfide ions undergo disproportionation into S_8 and solid Li_2S_2. The regenerated S_8 from polysulfide disproportionation undergoes simultaneous re-reduction on-site with the S_8 present in the cathode matrix, while Li_2S_2 undergoes further reduction to Li_2S through a solid-state process. The oxidation (recharge) process is entirely reversible. The comprehensive reaction can be expressed as $S_8 + 8Li^+ + 8e \rightleftharpoons 4Li_2S_2$. Given the minimal presence of soluble polysulfides in the electrolyte and the deposition of solid Li_2S_2/L_2S on-site within the cathode matrix, the polysulfide shuttle can be effectively circumvented.

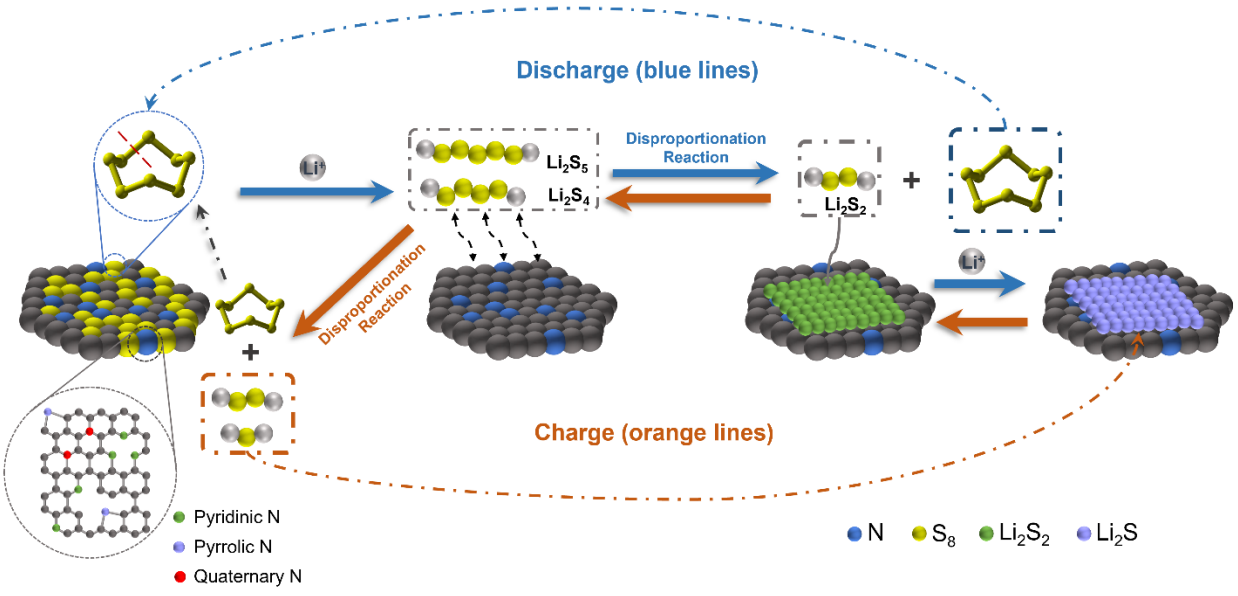

Figure 3-6. Illustration of the catalytic polysulfide disproportionation reaction mechanism

To further investigate the role of NC in mitigating the shuttle effect and to validate the hypothesis, an open system of 3-electrode cell was applied to monitor the changes in dissolved polysulfides and elemental sulfur in the electrolyte in real-time. For comparison, an S/SuperC65 electrode was also prepared. SuperC65 is a conductive additive commonly used to enhance the conductivity of electrode materials. It possesses a relatively low specific surface area of 65 m^2 g^{-1} and lacks functional group on its surface. Moreover, previous HPLC analysis indicated that SuperC65 cannot disproportionate polysulfide anions. By comparing the electrochemical behaviors of the S/NC and S/SuperC65 electrodes in this setup, we aim to better understand the mechanisms through which NC mitigates the shuttle effect and to provide further evidence for our proposed hypothesis.

During the measurement, the cell was discharged and charged to different depths of discharge (DoD) and depths of charge (DoC), respectively. The corresponding charge-discharge curves of two cells are shown in Figure 3-7 (a) and (b). Electrolyte samples were extracted from the fourth neck of the round-bottom flask at different states of discharge and charge for the real-time HPLC analysis to determine the electrolyte composition. The concentration of dissolved S_8 in the electrolyte at different discharge voltages was also labeled in the two discharge and charge curves. It appears that soluble sulfur remains detectable during the second discharge plateau when the NC cathode was used. In contrast, when SuperC65 served as the cathode host material, no soluble elemental sulfur was apparent in the second discharge plateau. These results illustrate that during the discharge process, the disproportionation of PS started to occur and S_8 was produced after the formation of Li_2S_n ($4 \leq n \leq 8$) for NC cathode. This experimental evidence has corroborated the catalytic sulfur reduction reaction mechanism that is depicted in Figure 3-6. The catalytic redox reaction of PS ions closely resembles the reduction O_2 catalyzed by MnO_2,

wherein H_2O_2 decomposes to the O_2 and H_2O. Subsequently, the O_2 undergoes reduced one more time on a gas-diffusion-electrode. The general reaction can be described as a pseudo 4 e^- O_2 reduction.[148]

AC impedance measurements were also conducted at different stages of discharge and charge, with the corresponding Nyquist plots displayed in Figure 3-7 (c), (d), (e), and (f). Both the S/NC and S/SuperC65 cells exhibited broad Nyquist plots consisting of two overlapping depressed semicircles. The semicircle in the high-frequency region is associated with the charge transfer process at the interface of the conductive agent, while the semicircle in the middle-frequency region corresponds to the Li_2S_2/Li_2S film formation on the carbon matrix of cathodes. [118] These Nyquist plots were analyzed using Zview software to gain a better understanding of the changes in impedance parameters at different states of discharge. The plots were further interpreted using the equivalent circuits depicted in Figure 3-7 (g). The fitted values of R_e, R_{ct}, and R_g of two cells at different discharge voltages are summarized in Table 3-3. The electrolyte resistance of both cells gradually increased with the progress of discharge. This increase can be attributed to the rising viscosity of electrolyte caused by the dissolution of PS that formed during the discharge process. However, the S/NC cell displayed a slower increment in R_e compared to the S/SuperC65 cell. This difference is due to fewer long-chain PS dissolving in the electrolyte of S/NC cell, resulting in a lower electrolyte viscosity. An important observation is that the large value of both R_g and R_{ct} of S/NC are induced by the porous structure and high specific surface areas of the NC host. Since the specific surface area of the NC host is relatively higher than that of SuperC65, initial contact between the components may be suboptimal, and the electrode may not be fully wetted by the electrolyte, contributing to high values of R_{ct} and R_g. Therefore, the changing trends of these parameters will be focused on in the following discussion.

The charge transfer resistance of S/C65 cell began to increase at 58% DoD, around 2.08 V. This stage of discharge corresponds to the beginning of the second discharge plateau, representing the initial transformation from Li_2S_n ($4 \leq n \leq 8$) to Li_2S_2. These insulating precipitates started to cover the surface of the cathode, blocking the interface for charge transfer. As discharging continued, the Li_2S_2/Li_2S accumulated, leading to a further increment in R_{ct}.[149] In contrast, the charge transfer resistance of S/NC cell showed a different variation trend. It experienced the first increment in R_{ct} at 26% DoD, corresponding to the slope of the first plateau. At this discharge depth, long-chain polysulfides began to be reduced to Li_2S_2, and S_8 was expected to be continuously produced because of the disproportionation of Li_2S_n ($4 \leq n \leq 8$). These insulating solid precipitates on the cathode surface blocked the charge transfer interface, causing an increase in impedance. The sudden decrease in R_{ct} at 45% DoD may be due to the redistribution of S_8 as the discharge proceeded. The highly porous structure of NC provides more surface area for Li_2S_2 to precipitate compared to C65, resulting in a thinner Li_2S_2 film on the cathode. This thinner film could explain the observed decrease in R_{ct} at subsequent discharge depths.

The resistance R_g in the equivalent circuit is related to the formation of the insulation film on the carbon matrix, which consists of Li_2S_2 and Li_2S. The increasing R_g in the S/SuperC65 can be explained by the gradual accumulation of these insulating discharge products at the cathode during the discharge process. In contrast, the S/NC cell exhibited a downward trend in R_g from the beginning of the discharge at 5% DoD to 26% DoD. During this stage, the reduction of S_8 into the soluble long-chain polysulfides contributed to the reduction of the insulating film on the S/NC cathode. A possible reason for this change is that although the NC facilitates the disproportionation reaction, it cannot convert all the PS in the system. Therefore, while some

insulating S_8 and Li_2S_2 are produced in this discharge stage, their impact on the insulating film formation on the cathode is not as big as the consumption of elemental sulfur. The increase in R_g at 2.06 V (45% DoD) can be ascribed to the beginning formation of Li_2S_2 from Li_2S_n ($4 \leq n \leq 8$) that has not been disproportionated. In the following discharge depth, R_g experienced a decrease after a slight fluctuation. This behavior may result from the simultaneous disproportionation of partial long-chain PS and the transformation of PS into Li_2S_2, causing a redistribution of insulating deposition layer on the cathode surface. This process forms a more uniform Li_2S/ Li_2S_2 film, which is consistent with the SEM image of the cycled S/NC electrode shown in Figure 2-10 (b), contributing to the observed decrement in R_g at subsequent discharge depths.

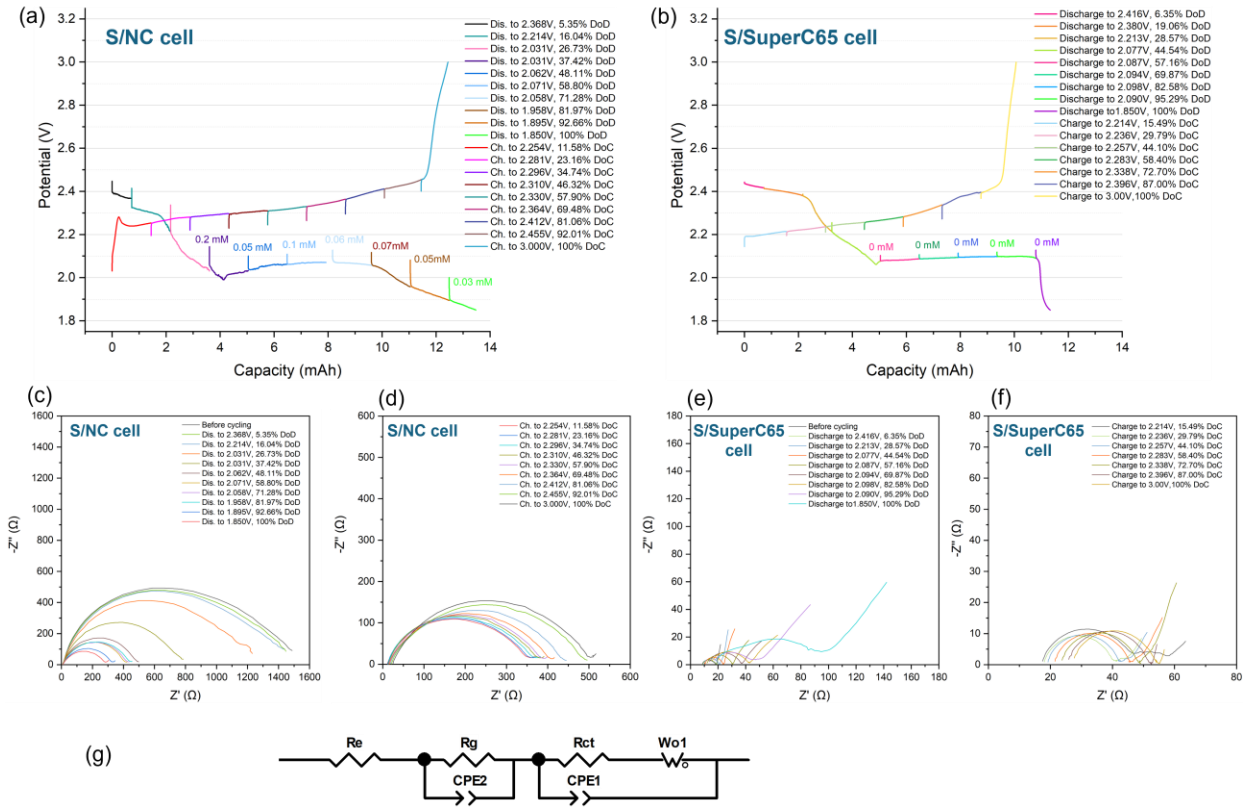

Figure 3-7. Charge-discharge curves of (a) S/NC and (b) S/SuperC65 Cells labeled with the concentration of dissolved S_8 in the electrolyte that measured by HPLC; Nyquist plots of S/NC cell during discharge and charge at different (c) DoD and (d) DoC; Nyquist plots of S/SuperC65 cell during discharge and charge at different (e) DoD and (f) DoC; (g) Equivalent circuits of cells.

Table 3-3. R_e, R_{ct}, and R_g values of S/NC and S/SuperC65 cells at different DoD.

	Re (Ω)		**Rct (Ω)**		**Rg (Ω)**	
	NC	**C65**	**NC**	**C65**	**NC**	**C65**
Before Cycling	6.00	8.52	323.4	3.62	1169	5.47
5% DoD	6.17	9.35	378.2	4.04	1079	5.35
26% DoD	6.44	10.13	864.4	3.23	410.6	6.73
45% DoD	7.36	19.45	3.00	3.75	462.4	18.14
58% DoD	7.73	13.7	3.42	6.91	389	15.21
82% DoD	9.15	15.07	5.27	10.39	418.1	16.5
93% DoD	9.70	15.95	6.49	22.08	302.1	12.52
100% DoD	10.18	17.04	8.642	13.65	254.5	53.02

The process of sulfur reduction entails a sequence of phase transformations occurring both heterogeneously and homogeneously, taking place in both the liquid electrolyte and on the surface of a conductive solid. Uneven deposition of Li2S2/Li2S during a sulfur cathode discharge can result in sizable nonconductive particles. These deposits may obstruct the active catalytic sites, contributing to an elevation in polarization potential. During the further discharge process, the elevated overpotential of the redox reaction ($Li_2S_2 + 2Li^+ + 2e \rightleftarrows 2Li_2S$) leads to a low discharge potential. The presence of aggregated Li_2S has exacerbates this issue during recharge due to its high oxidation overpotential. According to the R_g values of S/NC cell at different discharge depth that showed in Table 3-3 and SEM image of the cycled S/NC cell that displayed in chapter 2 (Figure 2-10 (b)), NC exhibited the capability not only to catalyze polysulfide disproportionation, but also can facilitate a more uniform deposition of Li_2S_2 on the carbon substrate. As shown in Figure 3-7 (a) and (b), unlike the sulfur cathode hosted by SuperC65, the discharge process of the sulfur electrode hosted by NC does not end sharply. This sharp end would indicate a sudden surface passivation. Instead, the discharge voltage of the sulfur electrode hosted by NC exhibited a much slower decrease. Similar instances of electrode passivation were also observed in the case of a Zn anode and an air-cathode of Li-air battery.[150,151]

For a more comprehensive understanding of the kinetics associated with the S/NC electrode, the DRT technique was employed to deconvolve the polarization process into various time constants through converting the impedance data from the previous EIS measurement (Figure 3-7 (c-f)) from frequency domain to time domain. Figure 3-8 compares the DRT profiles for the S/SuperC65 and S/NC electrodes, where the relaxation time (τ) correlates with the rate constants of each process, and the area of the relaxation amplitude (y-axis) indicates polarization

resistances. Notably, the DRT profiles of the S/SuperC65 cell and S/NC cell exhibit significant differences. Several key observations can be made from Figure 3-8. For the SuperC65 electrode, two distinct DRT peaks were observed: one at approximately 5.48 s and another at around 10^{-5} s. It is hypothesized that the peak at 10^{-5} s possess a rapid kinetics and corresponds to the reduction of dissolved polysulfides, while the one with slower kinetics that appeared at 5.48 s is likely associated with the redox reaction of Li_2S_2 and possibly Li_2S. In the case of the S/NC electrode, a prominent peak is observed at 10^{-2} – 10^{-3} s for both discharge and charge, demonstrating significant reversibility. Over the discharge period, two smaller peaks emerged and remained stable during recharge, with one coinciding with the peak observed in the SuperC65 electrode at approximately 5.5 s. Another signal emerged between the primary peak and the peak at 5.5 s, manifesting around 2.03 V during discharge and persisting steadily throughout the charging process. The noticeable contrast observed between the SuperC65 electrode and NC electrode suggests substantial differences in the sulfur redox mechanisms. The largest distinct peak at 10^{-2} s in the S/NC cell is attributed to the redox reaction of sulfur on the carbon electrode, involving a solid-to-liquid conversion, which has slower kinetics than the reduction of dissolved polysulfides. The rationale behind this argument is that given the heterogeneous catalytic polysulfide disproportionation as a chemical reaction, the NC electrode would ideally be enveloped by elemental sulfur deposits even before the discharge begins, maintaining this coverage throughout the entire discharge and recharge cycles. Conversely, the redox reaction on the S/SuperC65 electrode primarily involves dissolved species, leading to faster kinetics. Interestingly, the kinetics of the redox reaction of the sulfur deposit on the NC carbon electrode exhibited improvement after charging, evidenced by an almost one order of magnitude increase in relaxation time. The only plausible explanation could be summarized is that the sulfur

electrochemically deposited on the S/NC electrode displays enhanced kinetics. This enhancement is likely due to the sulfur on the S/NC electrode originating from both electrochemical oxidation and disproportionation processes, rather than solely from the dissolution of PS. This inference is supported by the absence of the most rapid peak typically associated with PS dissolution.

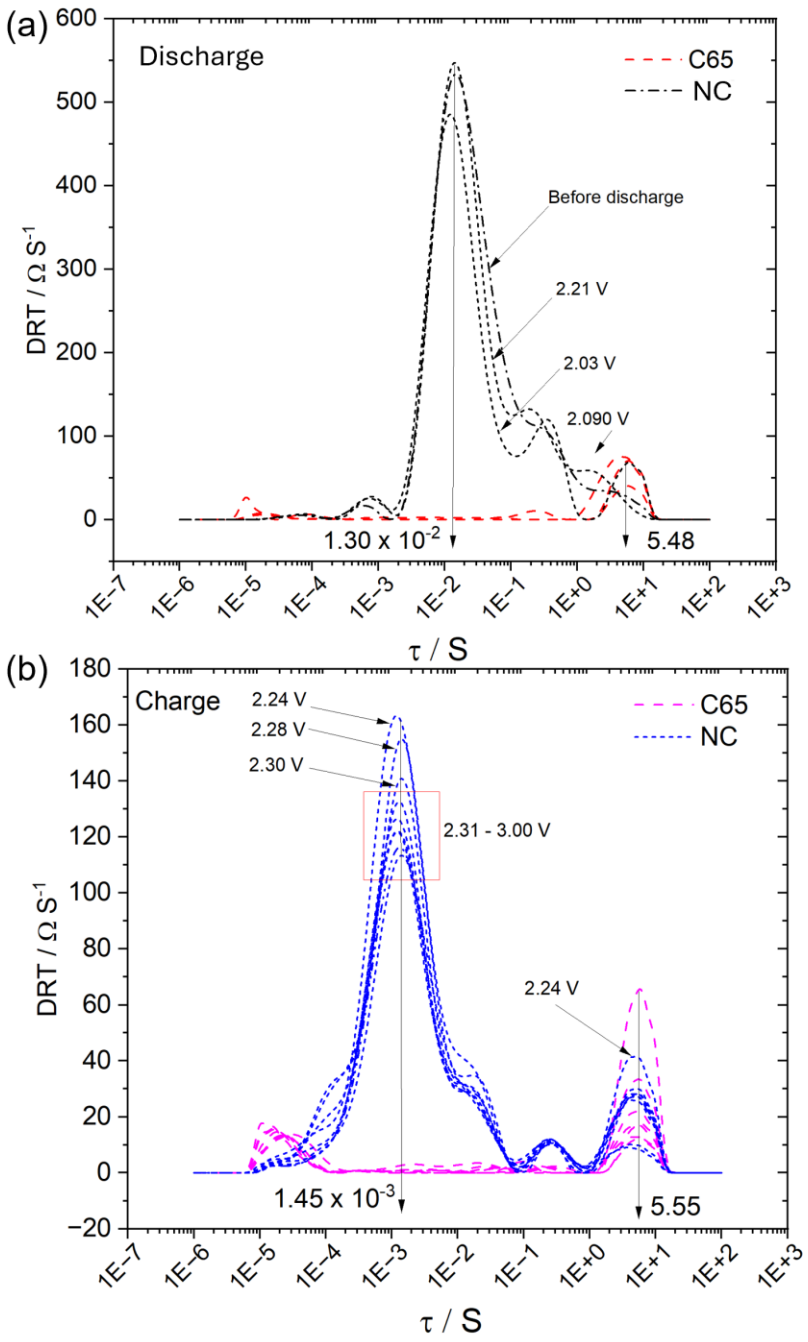

Figure 3-8. DRT plots of S/NC and S/SuperC65 cells obtained during (a) discharging, and (b) charging process.

Based on the experimental results from HPLC and EIS, the initiation and facilitation of the disproportionation reaction of PS by NC host during the discharge and charge process is indeed present. When a long-chain PS ion is adsorbed onto an active site, the S-S bond within the polysulfides weakens due to strong binding with the active site, resulting in the cleavage of the S-S bond. Unlike traditional Langmuir-Hinshelwood (L-H) heterogeneous adsorption-catalysis, which involves charge transfer, the disproportionation of PS ions does not require charge transfer. The resulting PS ions convert into elemental sulfur, which then undergoes further reduction, leading to the precipitation of Li_2S_2 onto the conductive matrix. Given that carbon's activity lies in the chemical disproportionation of PS, it can facilitate the disproportionation of the dissolved PS during both the reduction and oxidation of sulfur redox reactions. Consequently, there is no longer a need for a bifunctional or bidirectional catalyst.

It is evident that the disproportionation reaction of PS ions does occur, as elemental sulfur was identified as the predominant species in the electrolyte in a cycled Li-S cell, as shown in Figure 3-5 (c). However, the kinetics of the disproportionation reaction facilitated by NC may not be quick enough for the complete elimination of polysulfide shuttle effect. The reason is that if the disproportionation reaction were rapid enough to convert all the dissolved PS ions to S_8 and Li_2S_2, then the discharge and recharge curves of a sulfur cathode would exhibit a single discharge plateau, as no polysulfide redox reactions would be involved. However, this is not the case, as evidenced by the two-plateau discharge curve shown previously.

To validate the slow kinetics of the disproportionation reactions of PS, the electrochemical behavior of the S/NC cells was examined at low cycling currents. The cells were cycled at 0.01 C and 0.05 C in coin cells, with S/KB cells tested for comparison. All electrodes were prepared with a sulfur to carbon ratio of 7:3. The charge/discharge curves were normalized

for better observation and are shown in Figure 3-9. Compared to the profiles obtained under a high cycling rate of 0.5 C, the curves of the S/NC cell and the S/KB cell, as exhibited in Figure 3-9 (a), all displayed different patterns. The differences between the two cells were more pronounced at the low cycling rate. The second slope, indicated by the arrow 3 in the figures, contributes a greater portion of the total capacity in the S/NC cell compared to the S/KB cell. This behavior is not only more pronounced in the S/NC cell but also reversible in subsequent cycles, indicating that it is not caused by the decomposition of any inactive species, which typically undergo one-time irreversible decomposition reactions. A small dip and peak appeared in the discharge (from low to high potential) and charge (from high to low potential) curves, respectively, indicated by arrows 1 and 2 in the figure, respectively. The dip at the end of the first plateau of the discharge curve, as indicated by arrow 1, corresponds to the supersaturation of the PS solution within the cell, where the concentration and viscosity of PS reach their highest levels.[152] Also, since Li_2S_2 typically begins to form during the second discharge plateau, this small dip also represents the overpotential required for the nucleation of solid discharge products from the dissolved long-chain LiPS.[153] For the S/NC cell, because of the ability of NC for the facilitation of long-chain PS disproportionation reaction, some PS have already transformed into Li_2S_2. Consequently, the number of dissolved PS produced at this stage is slightly less than that in the S/KB cells, resulting in a smaller dip in the discharge curves of the S/NC cell. The overpotential shown in the charge curves, indicated by arrow 2, reflects the active energy needed for Li_2S to oxidize back to PS.[153] The S/NC cell shows a large overpotential compared to the S/KB cell, not only because of the larger amount of Li_2S produced at the S/NC cathode but also due to the disproportionation reaction that occurs during the charging process when long-chain

PS starts to form, as illustrated in Figure 3-6. This combination of factors requires the S/NC cell to overcome higher activation energy for the oxidation process.

Based on the HPLC results for different carbon materials, it is evident that KB also facilitates the disproportionation reactions of polysulfides (PS), though it is not as effective as NC. As cycling progresses, the sulfur content in the S/KB cathode reduces due to the shuttle effect, leading to a decrease in the production of PS. Consequently, the influence of KB on the disproportionation of PS becomes more pronounced, causing the differences between the charge/discharge profiles of the S/NC and S/KB cells to gradually diminish. However, as illustrated in Figure 3-9(f), the comparison between the cells with carbon host of NC and SuperC65, which did not exhibit the ability of facilitating the disproportionation of PS, still shows noticeable differences in their charge/discharge curves. When cycling at a lower c-rate of 0.01 C, these differences between the S/NC cell and S/KB cell became more obvious. The comparison charge/discharge curves are displayed in Figure 3-9 (f).

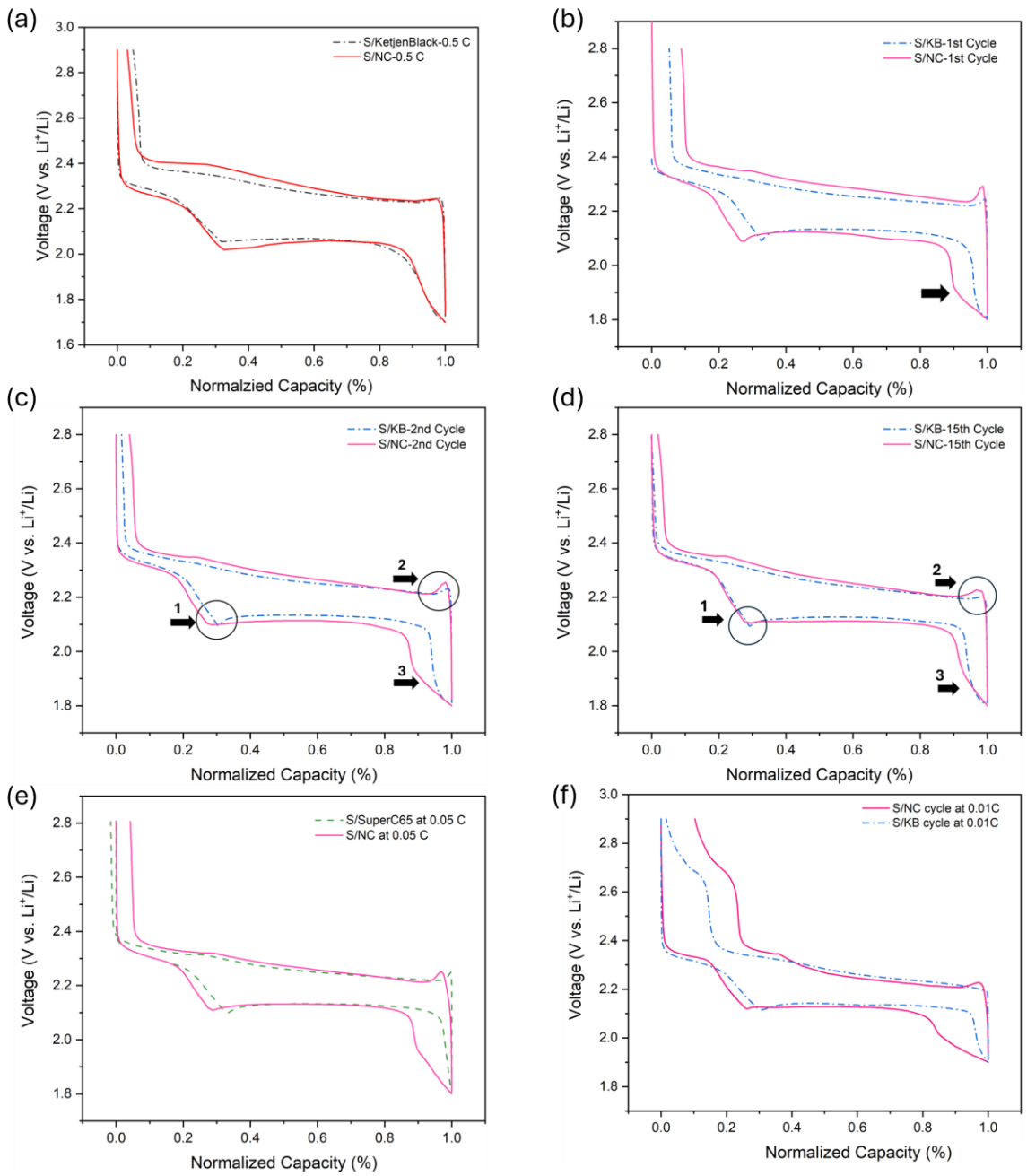

Figure 3- 9. Comparison of normalized charge/discharge curves of S/NC and S/KB cells cycled under (a) 0.5 C, and 0.05 C of (b) 1st cycle, (c) 2nd cycle, and (d) 15th cycle; (e) normalized charge/discharge curves of S/NC and S/SuperC65 at 0.05 C; (f) normalized charge/discharge curves of S/NC and S/KB cells cycled at 0.01 C.

The different patterns observed at low current rates partially confirm that the slow kinetics of the PS disproportionation reaction catalyzed by NC. However, this factor alone does not fully account for the presence of the two discharge plateaus in the discharge curves, previously attributed to the sluggish kinetics of PS disproportionation. This observation suggests that PS are not completely converted into S_8 and Li_2S_2 and continue to be generated during the cycling process. This can be attributed to the limited capacity of NC to disproportionate PS, due to the restricted number of functional groups available on NC.

To further investigate this hypothesis, the HPLC chromatograms of PS solutions at different concentrations were compared in Figure 3-10 (a)-(c). The results showed that after adding NC into the mixtures, the variation in the intensities of PS anion peaks decreases with increasing PS solution concentration. At a low concentration of 5 mM, PS anions are completely disproportionated, only S_8 peak appeared in the chromatogram. However, in PS solutions with higher concentration of 15 mM and 25 mM, while the intensities of S_8 peaks increase significantly, PS anions are still detected. The corresponding mass of NC required to completely disproportionate PS species in the solutions was also calculated and listed in Table 3-4. According to the HPLC chromatograms, each gram of NC can catalyze the disproportionation reactions of at least 0.096 g of S, but less than 0.288 g. For example, for an electrode containing 1.5 mg of sulfur, if the ratio of S to NC is 6:4, then theoretically, 0.096 mg of sulfur can be disproportionated (based on the results from 5 mM PS solution), which represents approximately 6.4 wt% of the total mass of sulfur in the cathode. When the ratios of S to NC increase to 7:3 and 8:2, the weight ratio of sulfur that can be disproportionated decreases to 4.1 and 2.4 wt%, respectively. In addition, it should be noted that these theoretical values are difficult to achieve, and the actual amounts of polysulfide species that can be disproportionated may be lower under

practical cycling conditions. This limitation may not be sufficient to convert the discharge curves of the Li-S battery into a single plateau pattern.

Even though the capacity decay mitigated by the catalysis of NC in each cycle is small, the cumulative effect can lead to significantly enhanced cycling performance of Li-S cells over long cycles. The cycling performance of S/NC and S/KB cells that cycled at 0.5 C and 0.05 C is displayed in Figure 3-10 (d) and (e). When cycled at a relatively high rate of 0.5 C, both the S/NC and S/KB cells exhibited similar capacity decay during the initial 10 cycles, and each of them retained 93% of their initial capacity. However, as cycling proceeded, the S/NC cell gradually demonstrated better cycling stability. The specific capacity retention of each cycle of the S/NC cell is about 99.88% of the previous cycle, slightly higher than the 99.64% observed for the S/KB cells. Consequently, the capacity loss per cycle for the S/NC cell was 0.24% less than that of S/KB cell. The retention rate of the specific capacity of S/NC cell after 120 cycles is 87%, while the S/KB cell showed a lower rate of 65%. When cycled at 0.05 C, the S/KB cell exhibited a capacity retention rate of 62% for the 10^{th} cycle, while the S/NC cell showed a slightly higher rate of 63%. In the subsequent cycles, although the decay rates for both cells were alleviated compared to the initial 20 cycles, their cycling performance varied greatly after 120 cycles. The variation in capacity retention of each cycle ($\frac{specific\ capacity\ of\ (n+1)^{th}\ ccle}{specific\ capacity\ of\ n^{th}\ cycle}$), as depicted in Figure 3-10 (f), indicates that despite the subtle difference in capacity decay per cycle between the two cells, the cumulative effect contributes to a much-improved cycling life for the S/NC cell compared to the S/KB cell. Therefore, although the mass of PS species that can be disproportionated through the catalysis of NC is limited, the presence of these disproportionation reactions plays a critical role in prolonging the cycle life of the Li-S battery.

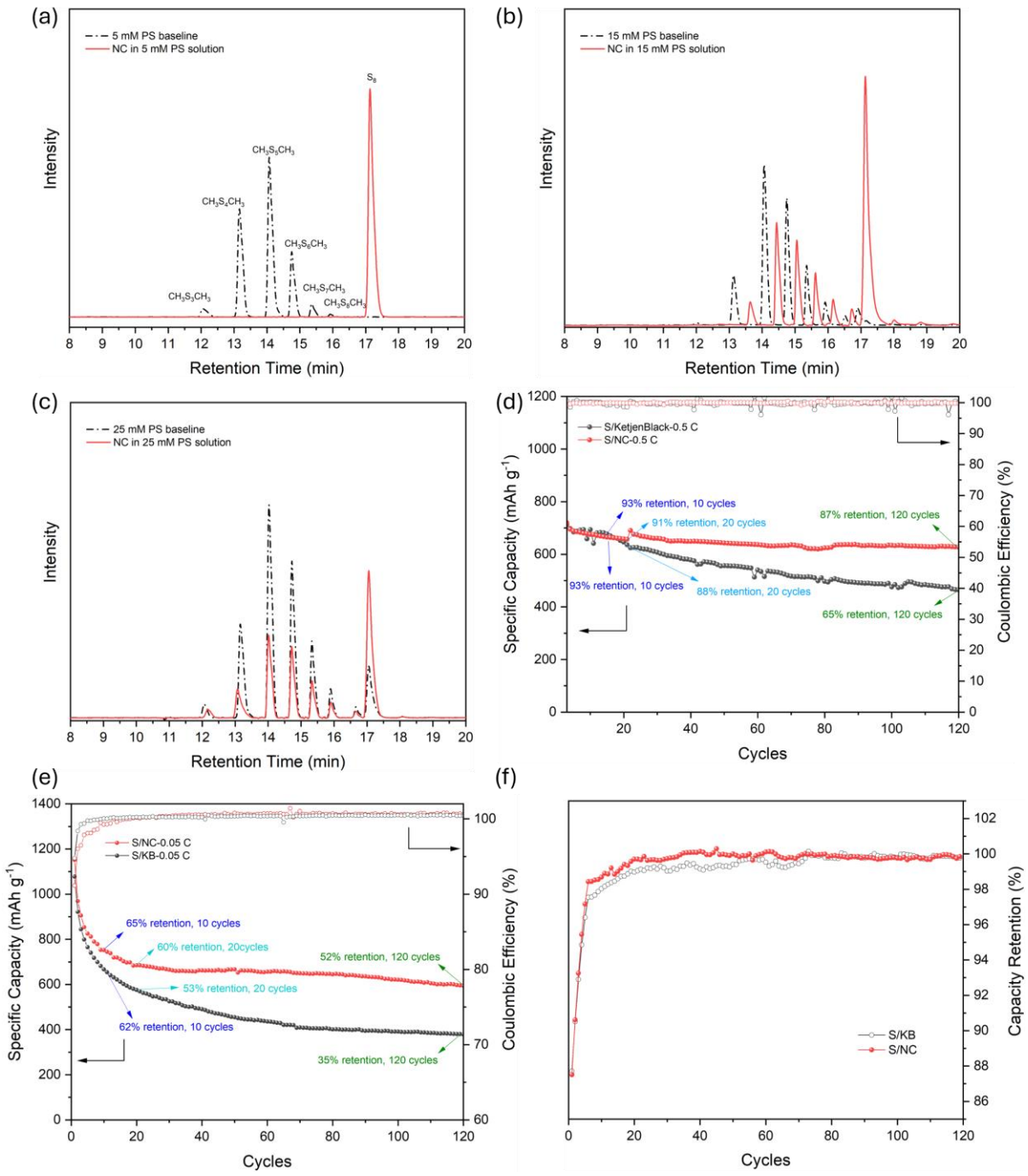

Figure 3-10. HPLC chromatograms of PS solutions with NC at different concentrations: (a) 5mM PS solution, (b) 15mM PS solution, and (c) 25mM PS solution; cycling performance of S/NC and S/KB cells cycling at (d) 0.5, and (e) 0.05 C; (f) capacity retention of each cycle (capacity of this cycle/capacity of the previous cycle).

Table 3-4. The mass of PS anions that can be completely disproportionated by unit mass of NC in PS solutions of different concentrations.

PS solution (mM)	Volume of Li_2S_6 solution (mL)	Mass of NC matrix (mg)	S_8 / NC (weight ratio)
5	1	10	0.096
15	1	10	0.288
25	1	10	0.48

Table 3- 5. Theoretical mass ratio of sulfur that can be disproportionated in S/NC electrodes with 1.5 mg loading of sulfur under different ratios of S and NC.

S/NC ratio	Mass of NC (mg)	Theoretically S can be disproportionated (mg)	Dispro. S / Total S (wt %)
6:4	1	0.096	6.4
7:3	0.64	0.061	4.1
8:2	0.38	0.036	2.4

3.4 Conclusion

In this chapter, we studied the interaction mechanisms between NC and PS in Li-S batteries. Through HPLC, and electrochemical analysis, we gained comprehensive insights into the NC's ability to facilitate the disproportionation reactions of PS. Color change experiments and HPLC analysis, along with the excellent cycling performance of S/NC cells presented in Chapter 1, led us to propose a hypothetical mechanism of pseudo-8-electron redox reaction. After the initial reduction of S_8 to long-chain lithium PS, high-order PS anions undergo disproportionation into S_8 and Li_2S_2. The regenerated S_8 is then simultaneously reduction on-site along with the S_8 present in the cathode matrix, while Li_2S_2 is further reduced to Li_2S as discharging continues. During charging, these reactions are reversible. The presence of these disproportionation reactions enhances the cycling ability of Li-S cells by reducing the presence of soluble PS in the electrolyte and ensuring the deposition of solid Li_2S_2/Li_2S on-site within the cathode matrix, thereby effectively relief the shuttle effect.

A systematic study comparing various carbon materials and inorganic compounds demonstrated that NC possesses a superior ability in facilitating PS disproportionation. Chromatograms of NC samples showed significant decreases in polysulfide peaks and increases in elemental sulfur peaks, indicating effective catalysis. Other carbon materials, including Vulcan XC72 and KB, displayed less pronounced catalytic effects, while some inorganic materials like MnO_2 and Cu_2S showed significant interaction with polysulfides, but through different mechanisms.

Although NC significantly reduces the remaining PS in the electrolyte, this improvement is not prominently reflected in the electrochemical behavior. The discharge curves of Li-S cells using NC still show the characteristic two discharge plateaus observed with conventional sulfur

cathodes. This can be attributed to the slow kinetics of PS disproportionated during cycling. While the contributions of these disproportionation reactions are not sufficient to eliminate the shuttle effect, the cumulative effect over many cycles results in excellent long-term cycling performance.

In conclusion, the findings of this chapter underline the critical role of NC in enhancing the performance of Li-S batteries by mitigating the shuttle effect through facilitating the disproportionation of polysulfides. The ability of NC to catalyze these reactions and facilitate the uniform deposition of solid discharge products offers a promising pathway to improving the efficiency and cycling life of Li-S batteries.

CHAPTER 4. POUCH CELLS MAKING AND TESTING

4.1 Introduction

Li-S batteries are considered as a promising next generation energy storage technology not only because of the abundant sources of sulfur in the Earth's crust but also because of their significantly higher theoretical specific capacity (1675 mAh g^{-1}) and energy density (2600 Wh kg^{-1}) compared to current commercial Li-ion batteries.[85] These advantages make Li-S batteries an attractive option for applications requiring high energy density and cost-effectiveness. However, despite their potential, completely replacing Li-ion batteries with Li-S batteries remains challenging due to the low utilization of insulating sulfur and the shuttle effect that occurs during the cycling process. These issues result in low practical output capacity and poor cycling life of the Li-S batteries. The shuttle effect is a major obstacle. It involves the dissolution and migration of polysulfides between the anode and cathode, leading to the loss of active material and the formation of insulating layers on the electrodes.[154] This not only reduces the overall efficiency and capacity of the battery but also causes rapid capacity fading and shortens the cycle life. Additionally, the insulating nature of sulfur and its reduction products requires the incorporation of conductive additives, which can increase the complexity and cost of the battery design.

In the previous chapter, we proposed NC, obtained through facile carbonization process using natural silk as the precursor, as the host material for sulfur cathodes. The S/NC cathode displays a promising cycling life because of the synergetic effect of the hierarchical porous structures of NC and the disproportionation reactions of polysulfides induced by the functional groups on the surface of the NC. The combination of properties in the NC material addresses

some of the key challenges faced by Li-S batteries, offering a potential pathway to improving their performance and durability.

For an initial material-level study, the S/NC cathode was tested in small-scale coin cells, which are commonly used in the early stage of developing a novel cathode material. While coin cells are valuable for initial testing and evaluation, pouch cells are more desirable for practical applications as they maximize energy density at the cell level owing to their lightweight packaging.[155] However, despite this advantage, certain issues can become more pronounced in larger-scale pouch cells, where there is a greater quantity of active material and reduced amount of electrolyte. In coin cell testing, the amounts of active materials within the cathode are limited, and the electrolyte is usually in excess. This excess can lead to some potential issues, and the results obtained at the coin cell level may not always be reproducible in pouch cells. Therefore, although coin cell testing provides valuable initial insights, further evaluation in pouch cells is necessary to fully understand the performance and practical viability of the S/NC cathode in real-world applications.

Recent studies on Li-S batteries have increasingly focused on boosting the sulfur content within the cathode. Although Li-S batteries inherently offer a much higher theoretical specific energy compared to LIBs, achieving a practical energy density that can compete with current commercial LIBs requires a high sulfur loading. Previous studies suggests that an areal sulfur loading of at least 3 mg cm^{-2} is essential for Li-S batteries to deliver a competitive specific energy and fully utilize the cost advantage of sulfur over expensive commercial materials like cobalt, and nickel.[156] However, increasing sulfur introduces significant challenges, particularly in maintaining cycle life and efficiency. High sulfur content can exacerbate the shuttle effect, leading to fast degradation of the cell. In addition, high sulfur content can intensify lithium

stripping and redeposition on negative electrode due to the higher current applied to the anode, potentially lithium dendrite growth. These dendrites could penetrate the separator, and therefore lead to the failure of the battery.

Another important factor for increasing the practical output specific energy of Li-S batteries is the quantity of electrolyte that is added to the cell. While an excess of electrolyte generally benefits the electrochemical performance of the cell, leading to a high capacity and prolonged cycling life, it decreases the practical energy density that the cell can deliver.[157] The practical energy density of a cell is defined as the ratio of energy capacity to the total weight of the cell. The more weight of inactive components, such as the current collectors, separators, and electrolyte, the lower the practical output specific energy. Therefore, to make Li-S batteries competitive with Li-ion batteries, the proportion of inactive components should be minimized. Adjusting the weight of electrolyte is an effective way to reduce "dead weight" of inactive components in the cell.[156] However, using less electrolyte can also introduce problems. With less amount of electrolyte, the dissolution and deposition of sulfur species in the electrolyte can be affected. Insufficient infiltration of electrolyte within the cathode can also lead to low output capacity due to the limited utilization of active materials. In addition, high sulfur loading can cause more long-chain polysulfides to dissolve in the electrolyte, increasing the internal resistance and polarization of the cell. This can result in the loss of the second plateau typically observed in the discharge profile of Li-S batteries, consequently resulting in a low total capacity.[157] Therefore, balancing the amount of electrolyte and find the appropriate E/S (electrolyte volume/sulfur weight $\mu L\ mg^{-1}$) ratio is also critical for optimizing the performance and practical energy density of the pouch cells of Li-S batteries.

To further investigate the performance of the NC as the host material for sulfur cathodes, pouch cells with S/NC cathodes were prepared and tested. Cathodes with varying areal sulfur loading, ranging from low to high (1-5 mg cm^{-2}), and different E/S ratios were also applied to assess the capabilities of the S/NC cathodes under various conditions.

4.2 Experiment

Pouch Cells Assemble

Pouch cells were assembled using 30 mm × 40 mm rectangle S/NC800 electrodes as cathodes. Lithium foil, with a thickness of 50 μm, was punched into 32 mm × 42 mm rectangular pieces and stacked with cooper foil, which working as the current collector. An aluminum tab and a nickel tab were welded to the cathodes and anode, respectively. For the single layer pouch cell, the separator (Celgard 2325) was cut into 36 mm × 46 mm rectangle.

The assembly process began with carefully stacking the S/NC cathodes, separator, and lithium anode in the correct sequence to ensure proper alignment and contact. The aluminum and nickel tabs were then positioned to extend out of the pouch, allowing for external electrical connections. The stacked components were placed into a pre-cut aluminum laminated film pouch bag, which was partially sealed, leaving a small opening for electrolyte injection. The appropriate amount of electrolyte was carefully injected into the pouch cell. After the injection, the pouch bag was fully sealed under vacuum conditions.

The double-sided coated S/NC electrode was prepared by casting S/NC slurry on both sides of an aluminum foil. The multi-layer pouch cells were assembled using a layer-by-layer strategy, as illustrated Figure 4-1.

The assembled pouch cells were rested overnight before testing to allow a thoroughly wetting of separator and electrodes.

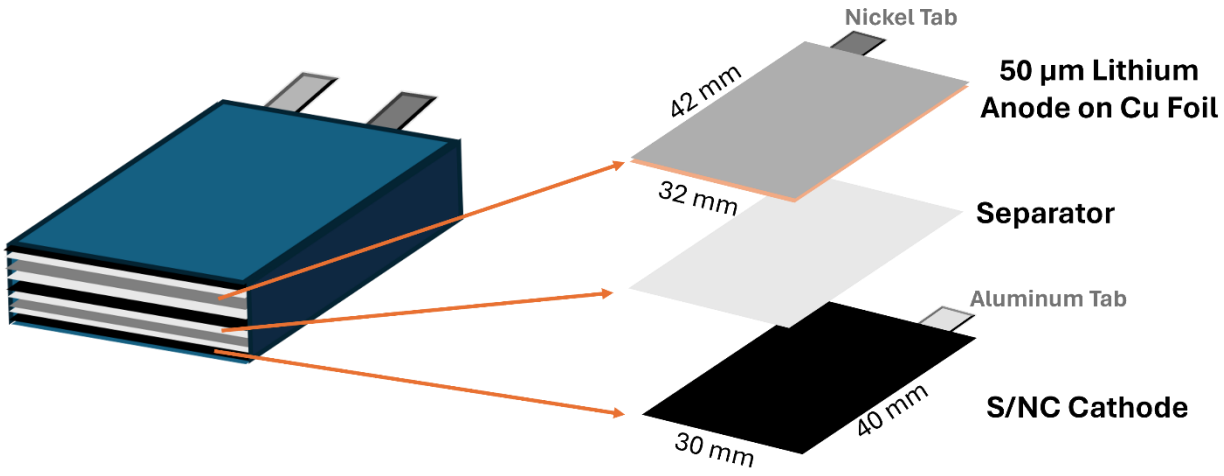

Figure 4-1. The construction of pouch cells.

Electrochemical Analysis

The pouch cell was sandwich between two plates and hand tight. This step was purposed to ensure a uniform and tight contact of the components within the cell. Galvanostatic charging/discharging tests were conducted on an Arbin battery testing system (BT200) in a voltage window of 1.8~2.9 V vs Li^+/Li at ambient temperature. The cycling performance of the cells was conducted at different C (1C = 1675 mA g^{-1}) rates.

Observation of Morphologies Variations of Cycled Lithium Anode

The cycled pouch cells were meticulously disassembled inside an argon-filled glovebox. The S/NC cathodes, separators, and lithium anodes were removed from the pouch cells and sealed in transparent plastic Petri dishes to prevent lithium from reacting with air. Subsequently, these components were transported out of the glovebox for further examination. The

morphologies were observed using the Keyence VHX 2000 microscope, and pictures were taken with the built-in digital camera. All images, including 3D images, were produced using the depth composition method.

4.3 Results and Discussions

The pouch cell was first tested with a relatively low areal sulfur loading of 1 mg cm^{-2} and an excessive electrolyte amount (E/S = 20 μL mg^{-1}). For comparison, a cell with S/KB cathode was also applied under the same conditions. The ratio of sulfur to carbon host materials within the cathodes was 65:35. The cells were activated at 0.05 C for two cycles and then cycled at 0.2 C. The electrochemical performance of the two cells is illustrated in Figure 4-2. The S/NC cell delivered a higher initial specific capacity of 954 mAh g^{-1} at 0.2 C compared to the 715 mAh g^{-1} delivered by the S/KB cell. It is notably that the initial coulombic efficiency of the S/NC cell when starting to cycle at 0.2 C is also higher than that of S/KB cell, as shown in Figure 4-2 (b). The S/NC cell has an initial coulombic efficiency of 99.6 %, while the S/KB cell showed a relatively lower coulombic efficiency of 94% for the first cycle at 0.2 C. This higher efficiency indicates that the migration of PS toward Li anode was effectively mitigated in the S/NC cell during the first discharge/charge process, suggesting that less amount of lithium polysulfides were transporting to anode and more active sulfur remained within the cathode. Over the following 100 cycles, the S/NC maintained a high coulombic efficiency above 99.5%, while the S/KB cell displayed an increased coulombic efficiency, eventually stabilizing around 99%. The S/NC cell was then used as the power source to light up an LED light, as exhibited in Figure 4-2 (a).

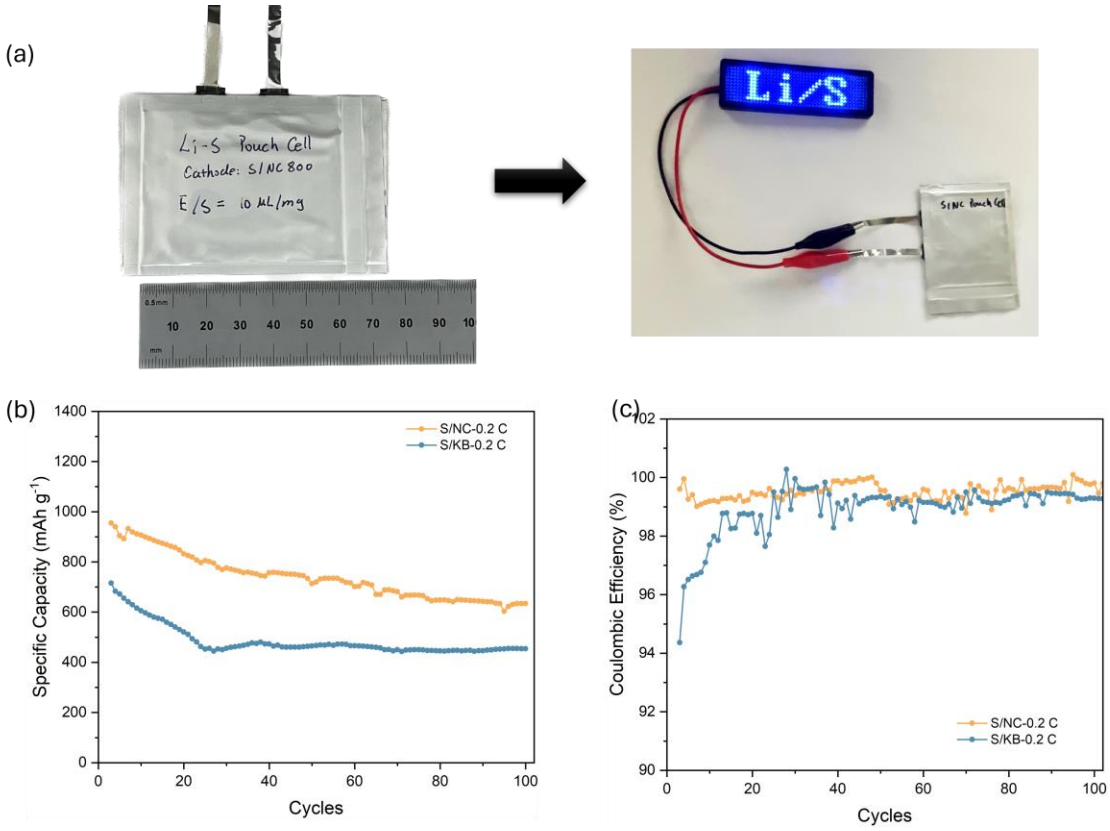

Figure 4-2. (a) LED light powered by the S/NC pouch cell; (b) Cycling and (d) CE comparison of S/NC and S/KB cells with 1mg cm^{-2} of sulfur loading and excess electrolyte at 0.2C.

When testing the feasibility of NC as the carbon host material for sulfur cathodes (as described in Chapter 2), the S/NC electrode was tested in coin cells with a low areal sulfur loading and excessive amount of electrolyte. While excessive electrolyte and low sulfur loading can extend the cycling performance of Li-S cells, these measures may diminish the advantages of high energy densities and low costs of Li-S batteries compared to conventional Li-ion batteries. To maximize the energy density advantages of Li-S batteries and effectively enhance its competitiveness over Li-ion batteries, the quantity of electrolyte, which is the electrochemically inactive component within the pouch cell, should be as low as possible.

The impact of electrolyte quantity on the electrochemical performance of S/NC cathodes was first investigated using coin cells with varying E/S ratios ranging from 5 μL mg^{-1} to 20 μL mg^{-1}. The S/NC composite used to make the electrodes contained 80 wt% sulfur, corresponding to 68 wt% of the overall cathode. All cells were initially activated at a low rate of 0.05 C for two cycles before being cycled at 0.2 C. The cycling comparison over 100 cycles is illustrated in Figure 4-3 (a). Interestingly, the cell with an E/S ratio of 5 μL mg^{-1} displayed the highest specific capacity of 983 mAh g^{-1} when cycling began at 0.2 C. However, it had the lowest specific capacity when started discharging at 0.05 C among the cells, as shown in Figure 4(b). This can be explained by the insufficient infiltration of electrolyte into the porous structures of cathodes prior to cycling, as evidenced by the increasing initial specific capacity at 0.05 C with higher electrolyte amounts. In the following 20 cycles, capacity retention decreased with increasing E/S ratios. However, the cell with an E/S ratio of 8 μL mg^{-1} demonstrated a capacity retention comparable to the 5 μL mg^{-1} cell over the subsequent 80 cycles. As displayed in Table 4-1, both cells displayed a relatively high capacity retention of around 86% over 100 cycles, indicating an optimal balance between electrolyte amount and electrochemical performance. The

charge/discharge profiles in Figure 4-3 (c) and (d) reveal different kinetics in cells with various E/S ratios. With an excessive amount of electrolyte, the lowest polarization and smallest voltage dip in the discharge curve (located at the beginning of the second plateau) indicate the lowest viscosity of the electrolyte. The cell with the lowest E/S ratio of 5 μL mg^{-1} showed the largest viscosity. Interestingly, the polarization of cells with E/S of 8 μL mg^{-1} gradually decreases as the cycling continues.

Table 4- 1. Specific capacities and capacities of S/NC coin cells with different E/S ratios.

	Initial Specific Capacity at 0.05 C (mAh g^{-1})	Initial Specific Capacity at 0.2 C (mAh g^{-1})	Specific Capacity at 100 cycles (mAh g^{-1})	Capacity Retention (%)
E/S=5 (μL mg^{-1})	1220	983	849	85.7
E/S=8 (μL mg^{-1})	1260	960	830	85.86
E/S=10 (μL mg^{-1})	1259	903	754	83.52
E/S=20 (μL mg^{-1})	1273	870	705	80.97

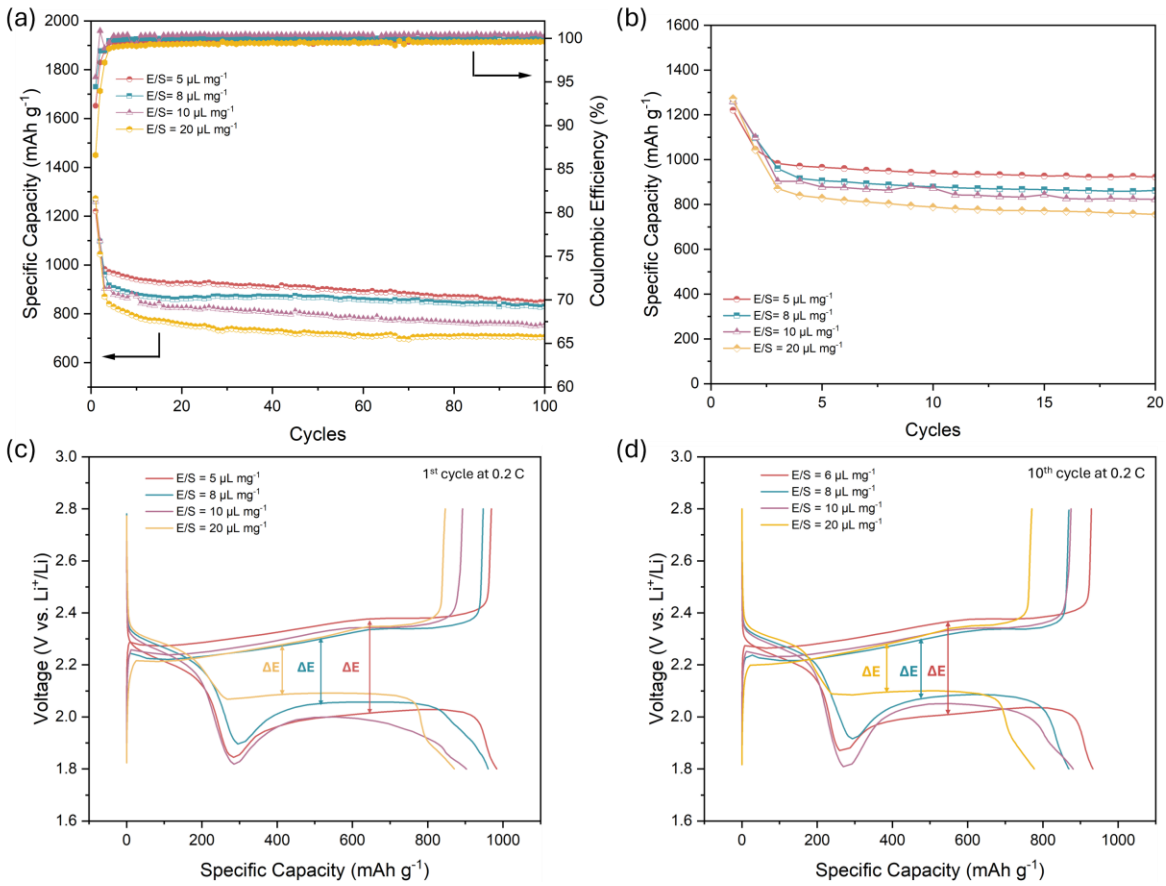

Figure 4-3. Cycling comparison of S/NC coin cells with different E/S ratios for (a) 100 cycles and (b) initial 20 cycles; Corresponding charge/discharge profiles at the (c) 1st and (d) 10th cycle.

Figure 4-4 presents the electrochemical analysis of S/NC pouch cells with varying E/S ratios from 5 to 12 μL mg^{-1}, tested at the S/NC cathodes with areal sulfur loading of 3.5 mg cm^{-2}. The cycling performance, as shown in Figure 4-4 (a), presents a similar trend in initial discharge capacities to those observed in coin cells. Specifically, the discharge capacities at the first cycle at 0.05 C (activation cycle) were 1273, 1336, 1273, and 1343 mAh g^{-1} for cells with E/S ratios of 5, 8, 10, and 12 μL mg^{-1}, respectively, demonstrating excellent sulfur utilization of S/NC cathodes even under lean-electrolyte conditions.

After two cycles of activation cycles, the cells were cycled at 0.1 C. The cell with an E/S ratio of 5μL mg^{-1} achieved the highest capacity of 1083 mAh g^{-1}, followed by 1068, 946, and 979 for cells with 8, 10, and 12 μL mg^{-1} of electrolyte, respectively. Over the subsequent cycles, pouch cells with E/S ratios of 8 and 10 μL mg^{-1} showed the best cyclability, with the highest capacity retention of 81% over 30 cycles and stable CE around 100%. In contrast, cells with the E/S ratio of 5 μL mg^{-1} experienced an unstable cycling over 30 cycles, as exhibited in Figure 4-4 (b), which can be attributed to the impact of sulfide species dissolution and deposition under lean electrolyte condition. In addition, the cell with the highest E/S ratio also showed a fast capacity decay. This phenomenon can be explained by the easier migration of PS species in the flood electrolyte environment. These results differ from those of coin cells, which is likely due to the higher loading of sulfur within the S/NC cathodes in the pouch cell, which resulted in large current applied to Li anode. That caused Li metal to experience a more serious corrosion and consequently lead to the fast failure of the cell.

Figure 4-4 (c) shows the coulombic efficiency of each cell. The cell with an E/S ratio of 10 and 12 μL mg^{-1} exhibited slight overcharging but maintained stable efficiency over 30 cycles, while the cell with 5 μL mg^{-1} of electrolyte showed an increasing tendency in CE. Figure 4-4 (d-

f) displays the charge/discharge profiles at 0.1 C. Unlike the relatively stable charge/discharge curves of cells with E/S ratios of 8-12 μL mg^{-1}, the cell with 5 μL mg^{-1} of electrolyte experienced severe overcharge in subsequent cycling, as depicted by the red line in Figure 4-4 (f). This overcharging can be attributed to the aggravated decomposition of the electrolyte under lean-electrolyte conditions. With less electrolyte, the movement of lithium ions and polysulfides is limited, making it difficult to continue converting insulating active material in subsequent cycles, eventually leading to cell failure.[158] This conclusion is further supported by the increased polarization observed in the cell with an E/S ratio of 5 μL mg^{-1}. Overall, an E/S ratio of 8 μL mg^{-1} provides the highest capacity and best cyclability for the pouch cell, making it the optimal choice for subsequent measurements.

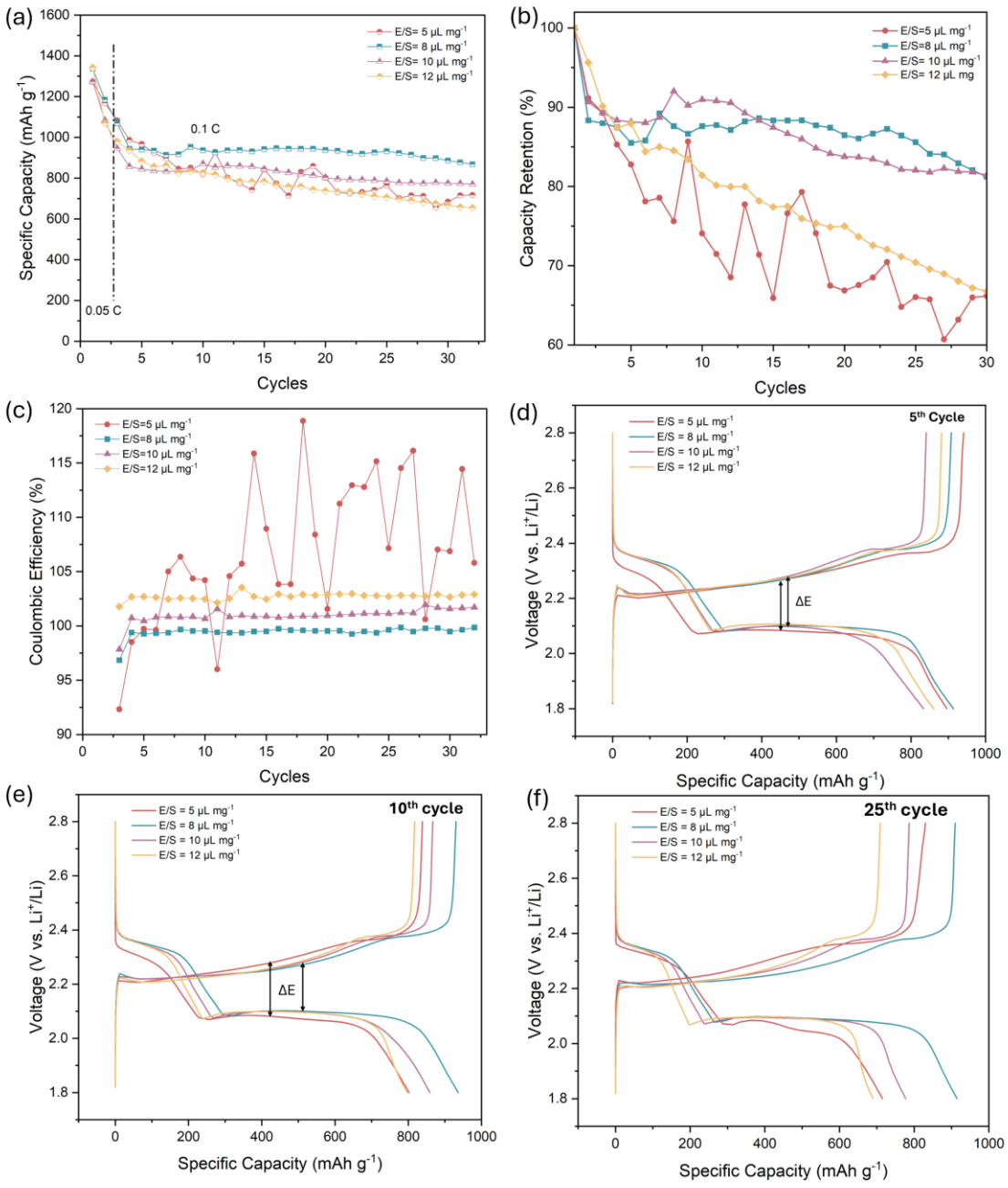

Figure 4-4. Pouch cells at different E/S ratios of 5-12 µL mg^{-1} cycling at 0.1 C: (a) cycling performance, (b) capacity retention, (c) coulombic efficiency, and (d-f) voltage profiles at 5^{th}, 10^{th}, and 25^{th} cycle.

The areal sulfur loading of the sulfur cathode is also a critical factor that impacts the competitiveness of Li-S batteries compared to conventional Li-ion batteries. To achieve a comparable energy density and cost with current commercial Li-ion batteries, the sulfur loading should reach at least 3 mg cm^{-2}.[157] However, increasing sulfur loading within the cathode also significantly affects the capacity and cycling life of the pouch cell. When the weight ratio remains unchanged in the S/NC composite, a higher sulfur loading typically requires an increase in electrode thickness. This can lead to wettability issues and mass transport differences due to the varied spatial distribution of dissolved polysulfides within the thicker cathode, resulting in sluggish kinetics and different reaction dynamics.[159]

To evaluate the performance of S/NC cathodes with high sulfur loading, pouch cells with sulfur loadings ranging from 1 to 5 mg cm^{-2} were assembled and tested with an E/S ratio of 8 μL mg^{-1}. The cycling performance and corresponding CE are displayed in Figure 4-5. At relatively low sulfur loadings of 1 and 2 mg cm^{-2}, the S/NC pouch cells delivered high initial specific capacities of 900 and 1000 mAh g^{-1}, respectively, at 0.2 C (following activation at 0.05 C for two cycles). Even with higher sulfur loadings of 3 and 5 mg cm^{-2}, the cells were able to achieve capacities of 638 and 732 mAh g^{-1} respectively, indicating good wettability and sulfur utilization in the thick S/NC electrode. In subsequent cycles, cells with low area sulfur loadings of 1 and 2 mg cm^{-2} demonstrated excellent cycling performance. They maintained approximately 90% of their initial capacities over 100 cycles, with retained capacities of 1026 and 910 mAh g^{-1}, respectively. Cells with higher sulfur loadings of 3 and 5 mg cm^{-2} also demonstrated good cyclability over 100 cycles, retaining specific capacities of 626 and 437 mAh g^{-1}, respectively. These results highlight the feasibility of achieving high sulfur loadings in S/NC cathodes while maintaining favorable electrochemical performance.

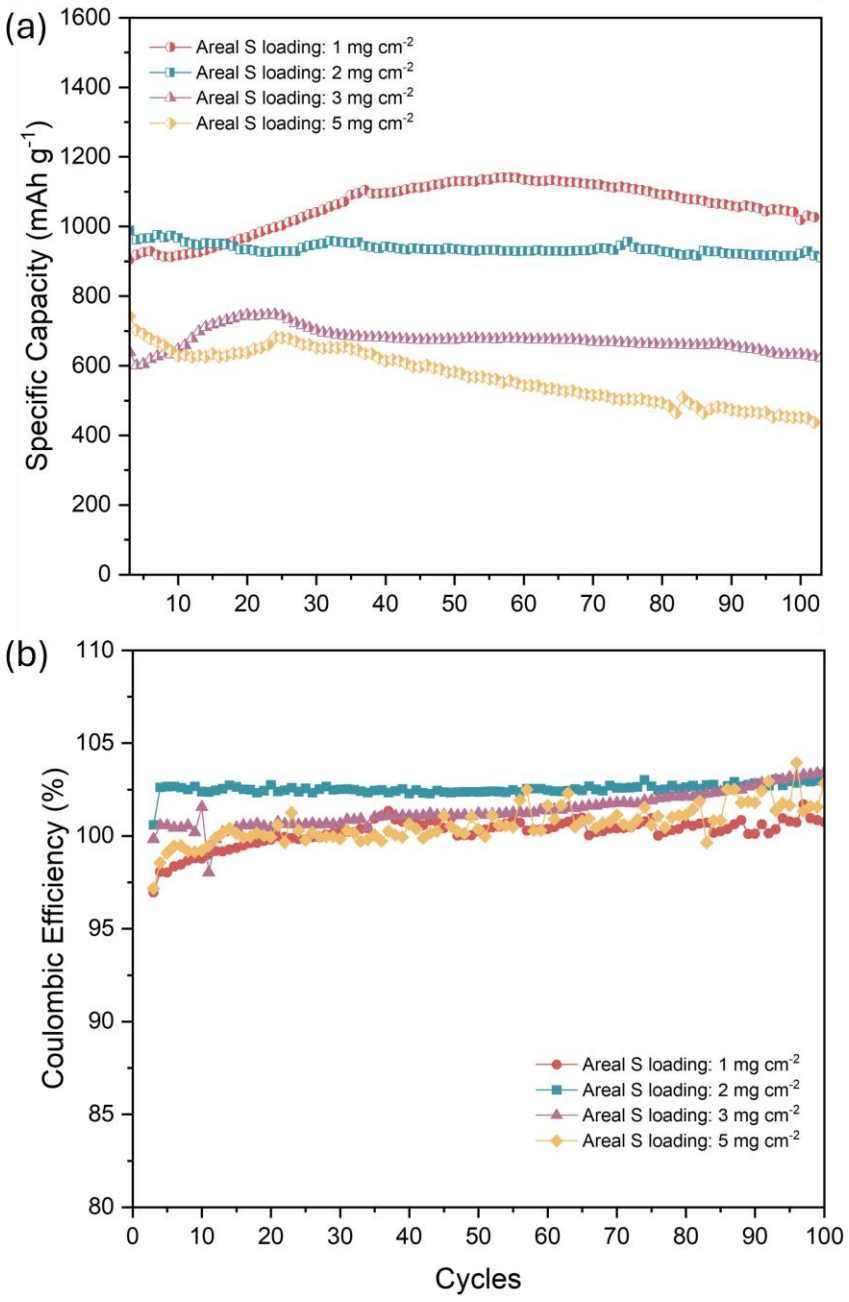

Figure 4- 5. (a) Cycling performance, and (c) coulombic efficiency of S/NC pouch cells with the areal sulfur loading of 1, 2, 3 and 5 mg cm^{-2} (E/S=8 µL mg^{-1}).

The prolonged cycling performance of S/NC pouch cells with areal sulfur loading of 2 mg cm^{-2} is displayed in Figure 4-6 (a). The cell initially exhibited good cycle stability, but significant capacity decay and continuous increase in CE began to appear after 100 cycles. By the 200^{th} cycle, the cell delivered a capacity of 638 mAh g^{-1}. To further investigate the variation of electrochemical behaviors of the cell, the charge/discharge profiles were recorded and shown in Figure 4-6 (b). During the initial 100 cycles, the voltages of the two discharge plateaus remained unchanged at 2.3 and 2.1 V, demonstrating the stable cyclability of the S/NC pouch cell. However, in the subsequent cycles, the voltage of discharge plateau voltages decreased, and the voltage of charge plateau voltage increased, demonstrating gradually increased polarization. This polarization led to severe overcharge and high CE of 107% at the 200^{th} cycle.

Although the NC matrix facilitates the disproportionation reactions of PS and helps mitigate the shuttle effect during cycling, the pouch cells displayed a shorter cycling life than coin cells (as shown in Chapter 2). The cycled pouch cell was disassembled in the glovebox to investigate the cause of rapid capacity fade during prolonged cycling. The cycled Li anode, cathode, and separator are exhibited in Figure 4-6 (d-f). Compared to the shiny fresh Li metal anode, displayed in Figure 4-6 (c), the cycled Li anode was covered with a dull passivation layer, and some of the lithium metal had detached from the copper foil (current collector) and adhered to the separator, as shown in Figure 4-6 (d) and (e). The cycled Li anode was observed under the microscope at ×200 magnification and displayed a powdery and porous morphology, which could be attributed to the growth of lithium dendrites. The corresponding images were recorded and shown in Figure 4-6 (g-h). Except for the dissolution and transportation of lithium polysulfides, the formation of these porous interface on anode is another factor that contribute to the increasing polarization of the cell as the proceed of cycling.[160] The impact of lithium

dendrites is more severe in pouch cells than in coin cells because of the higher current/capacity applied to the anode.[85] With a larger electrode area, pouch cells have higher total sulfur content within the system than coin cells (with same areal sulfur loading), leading to increased current and more severe dendrite growth. The uneven growth of these dendrites is evidenced by the still shiny lithium metal on anode after cycling, as indicated by the red circle in Figure 4-6 (d). The 3D image in Figure 4-6 (k) also shows uneven distribution of the lithium dendrites, indicated by different flat heights on the anode. Additionally, the repeated stripping and deposition of lithium during leads to the repeated SEI formation on the lithium surface and continuous electrolyte consumption, evidenced by the dry separator and S/NC cathode from the cycled pouch cell. The depletion of electrolytes also contributes to the polarization increasing of the cell.[160] This also explains the poor cycle life of cell with low E/S ratio that displayed in Figure 4-4. The detached lithium from current collector could be explained by the fallen off of lithium dendrites, which became dead lithium, from the current collector after wrapped by SEI.[85]

The S/NC pouch cell with a similar areal sulfur loading and the same E/S ratios was taken apart after ten cycles. Its cycling performance and charge/discharge curves are shown in Figure 4-7 (a) and (b). The morphologies of the cycled lithium anode were also studied the microscope. The images in Figure 4-7 (d-h) reveal pronounced lithium dendrite growth even within the initial ten cycles. The formation of these dendrites is uneven, some parts of the lithium metal remain shiny, while other parts are covered by the gray film or have already detached from the copper foil, as indicated by the red circle in Figure 4-7 (e).

When testing in the coin cells, the excessive lithium (200 μm) and electrolyte avoid the occurrence of the problem of the formation of dead lithium and consumption of electrolyte. However, in pouch cells, the amount of electrolyte and the thickness of the lithium anode (50

μm) must be limited to improve the practical energy density of the cell. Not only the S/NC cathode, but the stability of lithium anode is also critical for the long-term cycling life of the cell. Therefore, enhancing the protection of the lithium metal anode is crucial for improving the cycling stability of Li-S pouch cell.

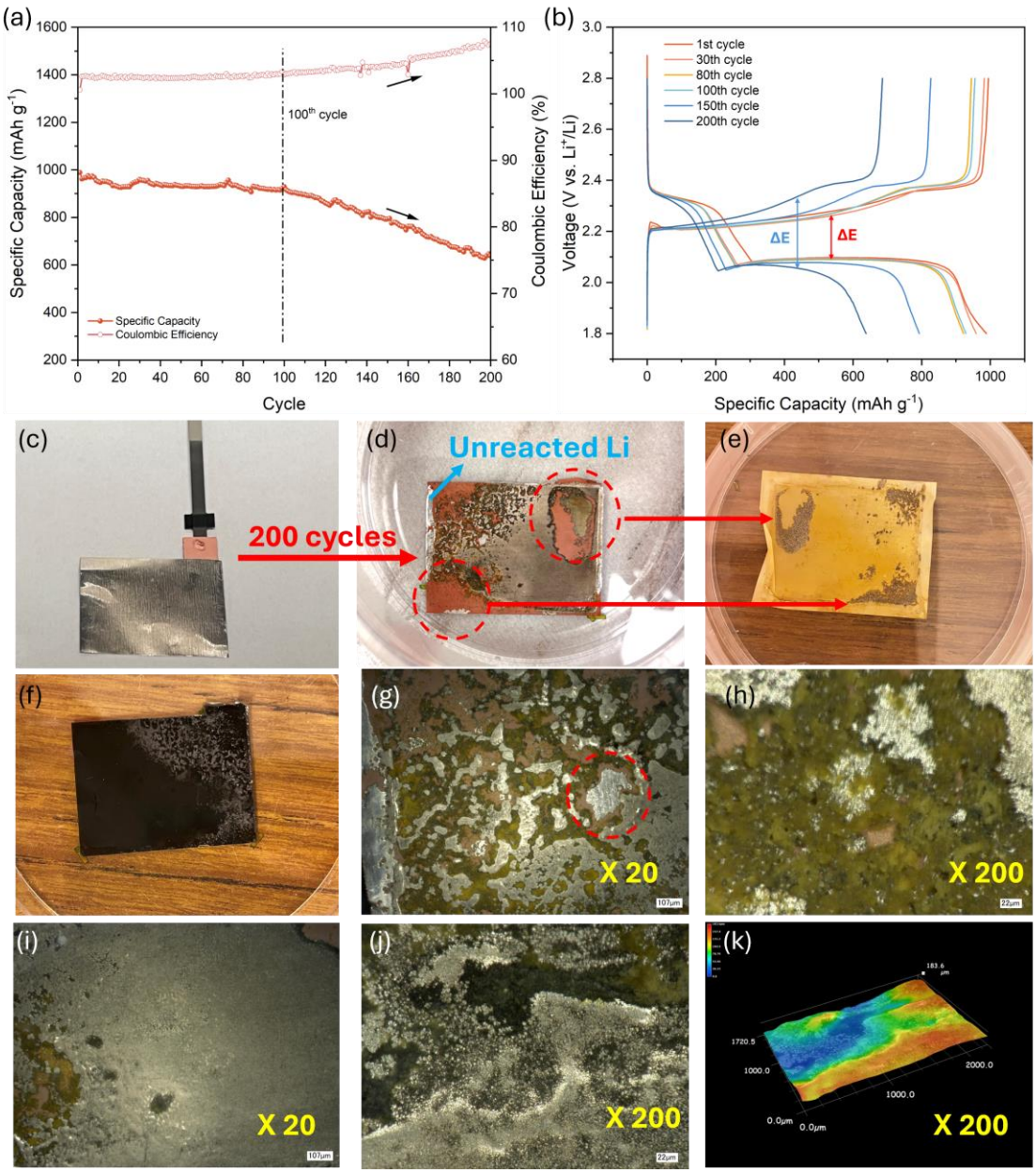

Figure 4-6. Extended (a) cycling performance and (b) charge/discharge profiles of pouch cell with areal sulfur loading of 2.2 mg cm^{-2}; (c) Fresh Li anode; (d) Li anode, (e) separator, and (f) S/NC cathode from pouch cell after 200 cycles; (g-j) Morphologies of the cycled Li anode obtained at different magnifications; (k) 3D image of the cycled Li anode.

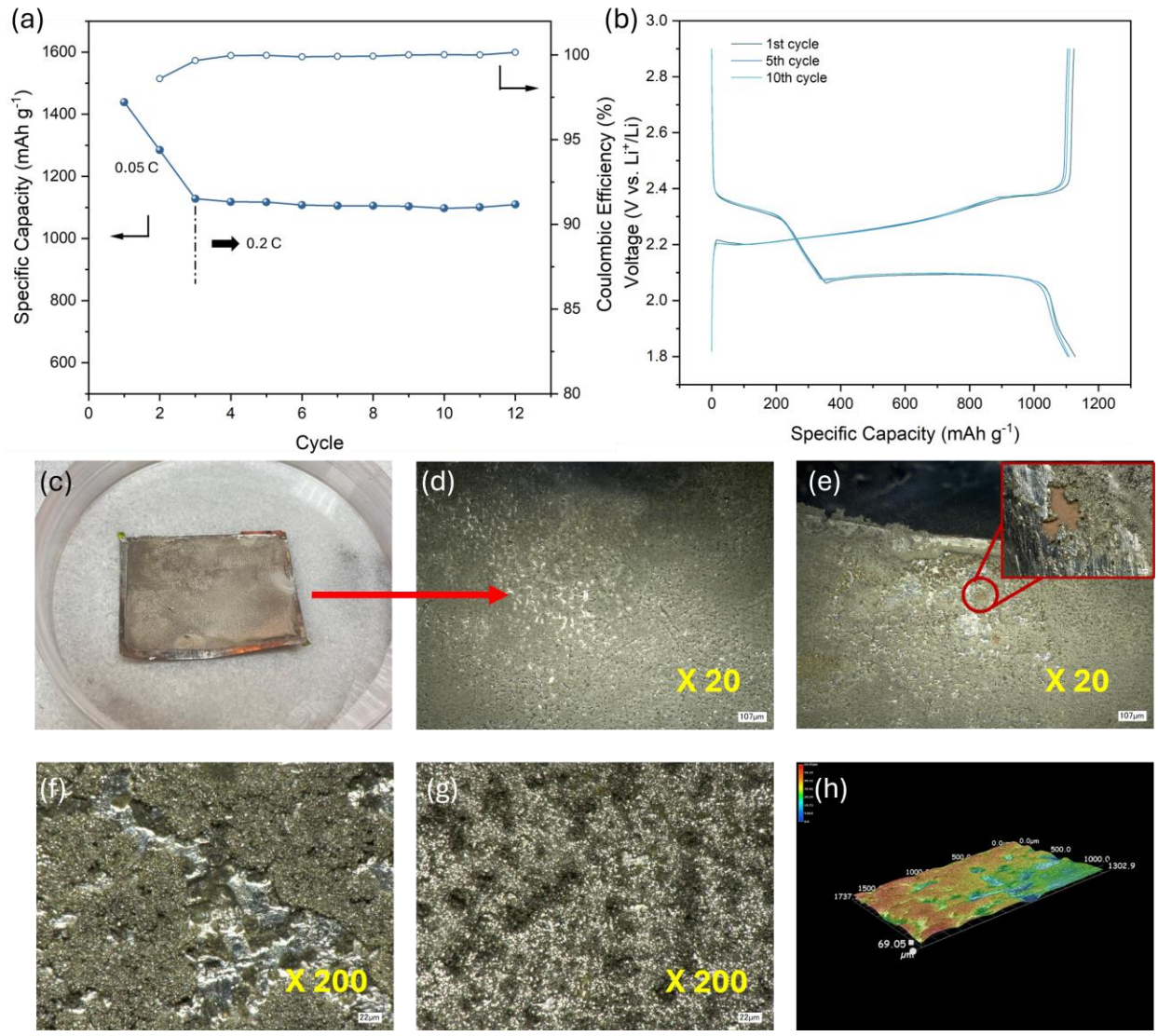

Figure 4-7. (a) Cycling performance and (b) corresponding charge/discharge profiles of S/NC cells (2.6 mg cm^{-2} of areal sulfur loading and E/S = 8 µL mg^{-1}) that activate at 0.05 C and cycling at 0.2 C; (c) Cycled lithium anode after 10 cycles; (d-g) Morphologies of the cycled Li anode obtained at different magnifications; (h) 3D image of the cycled Li anode.

In the practical Li-S pouch cells, more than one layer of sulfur cathode is required to achieve high energy density at the cell level. To maximize the energy density of the cell, which is the amount of energy stored per unit weight or volume, double-side coated sulfur cathodes are required to reduce the weight of inactive materials. Therefore, in addition to S/NC pouch cells with single-side cast electrodes, the performance of one layer double-side coated cathode was also examined at 0.2 C with the results displayed in Figure 4-8 (a). The areal sulfur loading of the applied S/NC cathode is 1.3 mg cm^{-2}, and the cell was tested at the E/S ratio of 8 μL mg^{-1}. The cell initially delivered a specific capacity of 735 mAh g^{-1} when cycling at 0.2 C and then experienced a capacity increase over the first 20 cycles, which could be attributed to the gradual infiltration of electrolyte to the active material within the cathode. After 160 cycles, the high specific capacity of 701 mAh g^{-1} was still preserved, demonstrating its good cycling performance.

The performance of 2-layer double-side coated cathodes is shown in Figure 4-8 (b). The cell was fabricated using the layer-by-layer strategy with two pieces of double-sided coated S/NC cathodes. Each side of the applied S/NC cathode had an area of 30 cm^2, containing a total of 156 mg of sulfur.[85] The cell was assembled by placing the S/NC cathode, separator, and lithium anode layer by layer, as the schematic graph that is shown in Figure 4-1. The two layers cell displayed an initial specific discharge capacity of 931 mAh g^{-1} at 0.2 C. Although it experienced a rapid capacity decay over the following two cycles, it maintained stable cycling performance in subsequent cycles, delivering a capacity of 664 mAh g^{-1} at the 140^{th} cycle. This consistent performance indicates the effectiveness of the S/NC cathodes in maintaining high capacity and stability even in multi-layer pouch cell configurations, making it a promising candidate for practical high-energy-density Li-S batteries.

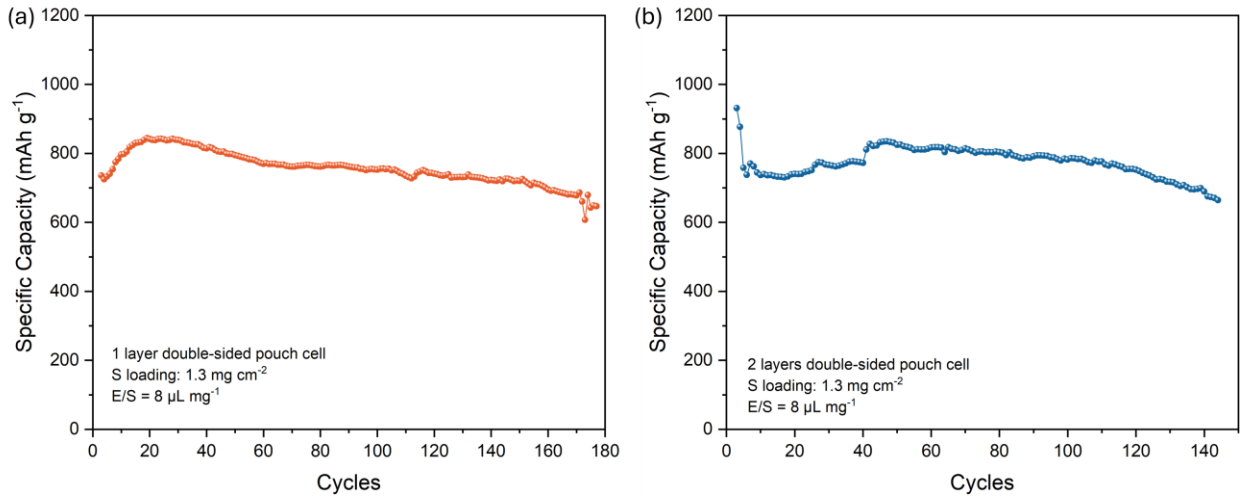

Figure 4- 8. Cycling performance of pouch cells with (a) single layer double-sided coated S/NC cathode, and (b) two layers double-sided coated S/NC cathodes.

3.5 Conclusion

This chapter presents a comprehensive investigation of the performance of pouch cells utilizing the S/NC cathode for Li-S batteries. The initial test that was conducted on the cell with low sulfur content and excessive electrolyte (E/S = 20 μL mg^{-1}) demonstrated the superior performance of S/NC cathodes over S/KB cathodes. This improvement is attributed to the mitigation of the shuttle effect though disproportionation reactions of PS facilitated by the NC host.

The study further explored the viability of S/NC cathodes with lean electrolytes and high sulfur loading. Pouch cells with S/NC cathodes displayed a high specific capacity of 1272 and 716 mAh g^{-1} at the 1^{st} and 30^{th} cycles respectively with a low E/S ratio of 5 μL mg^{-1}, indicating excellent wettability and sulfur utilization of the cathode. The optimal E/S ratio of 8 μL mg^{-1} presented the best cycling stability, with the highest capacity of 868 mAh g^{-1} and a stable CE over 99.5% by 30 cycles, pointing to a balance between the electrolyte quantity and cell performance. This ratio minimized polarization and facilitated electrolyte infiltration for better utilization of sulfur. In the study of the impact of sulfur content on battery performance, the pouch cells with low sulfur loadings of 1 and 2 mg cm^{-2} displayed capacity retention of 90% over 100 cycles, indicating the excellent cycling stability of S/NC cathodes. High sulfur content cells with 3 and 5 mg cm^{-2} of sulfur loadings also achieved high specific capacities and maintained good cycling stability.

The prolonged cycling tests of S/NC pouch cells demonstrated apparent capacity decay and polarization increase with continuous cycling. Examining the morphologies of components from cycled cells revealed the formation of porous and powdery lithium dendrites and electrolyte depletion, which contribute to the increased polarization and decay of the cell. These results

underscore the importance of lithium protection in achieving long-term stability for Li-S pouch cells with lean electrolytes and high sulfur content.

In conclusion, our S/NC cathode shows significant potential in improving the performance of Li-S pouch cells under lean electrolyte and high sulfur loading conditions. The findings presented in this chapter underscore the significance of optimizing not only the sulfur cathodes but also the lithium metal anode is significant for the overall performance of Li-S pouch cell with high energy density. These insights provide a promising way toward developing viable Li-S batteries as a competitive alternative to current Li-ion technologies.

CHAPTER 5. CONLUSIONS AND FUTURE WORKS

Li-S batteries are competitive alternatives to current commercial Li-ion batteries in the marketplace because of their high theoretical energy density and low cost of sulfur. However, the insulating nature of elemental sulfur and the shuttle effect hinder the practical development and application of Li-S batteries.

In this thesis, a novel carbon host material for sulfur cathodes, designated as NC, was presented. The carbon was derived from the carbonization of degummed natural silk. This novel carbon material possesses hierarchically porous structures and inherently doped nitrogen atoms, which help to physically trap and chemically encapsulate dissolved LiPS species at the cathode side and prevent their transportation toward the Li anode. Different carbonization ranging from 750 to 900 ºC was tested. The carbon obtained at 800 ºC shows the optimized porosity and the highest nitrogen content. As a result, its composite with sulfur displays the best electrochemical properties, including excellent cyclability and rate performance, as the cathode for Li-S batteries.

From the results of the color change experiment and HPLC analysis, we found that NC can facilitate the disproportionation reactions of PS species, transforming them into elemental sulfur and Li_2S_2 simultaneously. These disproportionation reactions enhance the cycling ability of Li-S cells by reducing the possibility of soluble PS species shuttling toward the Li anode and ensuring the deposition of solid Li_2S_2/Li_2S on-site within the cathode matrix. However, the role of the disproportionation reaction of PS in each cycle is subtle and insufficient to eliminate the shuttle effect completely. Therefore, the much-improved cycling of S/NC Li-S batteries is the result of a cumulative effect over decades and hundreds of cycles.

The S/NC cathodes show superior electrochemical properties in the coin cells with low sulfur loading and excessive electrolytes, and they also perform well in pouch cells with high sulfur content and limited electrolytes. Although the electrolyte amount in pouch cells should be minimized to realize a high practical energy density, the S/NC pouch cells delivered the highest capacity and best cycle stability with the E/S ratio of 8 $\mu L\ mg^{-1}$, indicating a balance between the electrolyte quantity and cell performance at this E/S ratio.

S/NC pouch cells could retain stable cycling and CE within the initial 100 cycles, depending on the sulfur loading within the cathode. However, most of the cells experienced a rapid capacity decay or even a sudden failure in prolonged cycling. Through the explorations of components of cycled pouch cells, it is found that the impact of lithium dendrite growth is more severe under conditions of low electrolyte and high sulfur loadings. In addition, the repeated striping and deposition of lithium lead to the depletion of electrolytes due to the formation of SEI in long-term cycling. These issues result in increased polarization, the formation of dead Li, and ultimately, battery performance degradation or even failure.

In future studies, the investigation could focus on better utilizing the disproportionation reactions of PS species to extend the cycling life of Li-S batteries to levels comparable to current commercial Li-ion batteries. Furthermore, optimization of the lithium metal anode is necessary to ensure a high energy density Li-S cell with superior cycling life.

REFERENCES

[1] A. Koyamparambath, J. Santillán-Saldivar, B. McLellan, G. Sonnemann, *Resour. Policy* **2022**, *75*, DOI 10.1016/j.resourpol.2021.102465.

[2] B. Scrosati, *J. Solid State Electrochem.* **2011**, *15*, 1623.

[3] M. S. Whittingham, *Proc. IEEE* **2012**, *100*, 1518.

[4] G. Crabtree, E. Kócs, L. Trahey, *MRS Bull.* **2015**, *40*, 1067.

[5] W. van Schalkwijk, B. Scrosati, *Adv. Lithium-Ion Batter.* **2002**, 1.

[6] M. V. Reddy, A. Mauger, C. M. Julien, A. Paolella, K. Zaghib, *Materials (Basel).* **2020**, *13*, 1884.

[7] M. S. Whittingham, *Electr. Energy Storage Intercalation Chem.* **1976**, *192*, 1126.

[8] T. Fujita, K. Toda, *Japanese J. Appl. Physics, Part 1 Regul. Pap. Short Notes Rev. Pap.* **2003**, *42*, 6131.

[9] S. Basu, C. Zeller, P. J. Flanders, C. D. Fuerst, W. D. Johnson, J. E. Fischer, *Mater. Sci. Eng.* **1979**, *38*, 275.

[10] M. Fichtner, K. Edström, E. Ayerbe, M. Berecibar, A. Bhowmik, I. E. Castelli, S. Clark, R. Dominko, M. Erakca, A. A. Franco, A. Grimaud, B. Horstmann, A. Latz, H. Lorrmann, M. Meeus, R. Narayan, F. Pammer, J. Ruhland, H. Stein, T. Vegge, M. Weil, *Adv. Energy Mater.* **2022**, *12*, DOI 10.1002/aenm.202102904.

[11] A. K. Padhi, K. S. Nanjundaswamy, J. B. Goodenough, *J. Electrochem. Soc.* **1997**, *144*, 1188.

[12] C. Delmas, I. Saadoune, *Solid State Ionics* **1992**, *53–56*, 370.

[13] C. K. Chan, H. Peng, G. Liu, K. McIlwrath, X. F. Zhang, R. A. Huggins, Y. Cui, *Nat. Nanotechnol.* **2008**, *3*, 31.

[14] Y. Miao, P. Hynan, A. Von Jouanne, A. Yokochi, *Energies* **2019**, *12*, 1.

[15] T. Horiba, *Proc. IEEE* **2014**, *102*, 939.

[16] A. Van Der Ven, J. Bhattacharya, A. A. Belak, *Acc. Chem. Res.* **2013**, *46*, 1216.

[17] Y. Huang, L. Lin, C. Zhang, L. Liu, Y. Li, Z. Qiao, J. Lin, Q. Wei, L. Wang, Q. Xie, D. L. Peng, *Adv. Sci.* **2022**, *9*, 1.

[18] Y. Chen, T. Wang, H. Tian, D. Su, Q. Zhang, G. Wang, *Adv. Mater.* **2021**, *33*, 1.

[19] V. Etacheri, R. Marom, R. Elazari, G. Salitra, D. Aurbach, *Energy Environ. Sci.* **2011**, *4*, 3243.

[20] C. Barchasz, J. C. Leprêtre, F. Alloin, S. Patoux, *J. Power Sources* **2012**, *199*, 322.

[21] S. S. Zhang, *J. Power Sources* **2013**, *231*, 153.

[22] A. Manthiram, Y. Fu, S. Chung, C. Zu, Y. Su, **2014**.

[23] J. Sun, T. Wang, Y. Gao, Z. Pan, R. Hu, J. Wang, *InfoMat* **2022**, 1.

[24] R. Fang, S. Zhao, Z. Sun, D. W. Wang, H. M. Cheng, F. Li, *Adv. Mater.* **2017**, *29*, 1.

[25] Z. W. Seh, Y. Sun, Q. Zhang, Y. Cui, *Chem. Soc. Rev.* **2016**, *45*, 5605.

[26] A. Manthiram, Y. Fu, S. H. Chung, C. Zu, Y. S. Su, *Chem. Rev.* **2014**, *114*, 11751.

[27] M. He, X. Li, X. Yang, C. Wang, M. L. Zheng, R. Li, P. Zuo, G. Yin, X. Sun, *Adv. Energy Mater.* **2021**, *11*, 2101004.

[28] T. Yim, M. S. Park, J. S. Yu, K. Kim, K. Y. Im, J. H. Kim, G. Jeong, Y. N. Jo, S. G. Woo, K. S. Kang, I. Lee, Y. J. Kim, *Electrochim. Acta* **2013**, *107*, 454.

[29] A. Rafie, J. W. Kim, K. K. Sarode, V. Kalra, *Energy Storage Mater.* **2022**, *50*, 197.

[30] M. He, X. Li, N. G. Holmes, R. Li, J. Wang, G. Yin, P. Zuo, X. Sun, *ACS Appl. Mater. Interfaces* **2021**, *13*, 38296.

[31] X. Yang, X. Li, K. Adair, H. Zhang, X. Sun, *Structural Design of Lithium–Sulfur Batteries: From Fundamental Research to Practical Application*, Springer Singapore, **2018**.

[32] J. Liang, Z. H. Sun, F. Li, H. M. Cheng, *Energy Storage Mater.* **2016**, *2*, 76.

[33] Y. X. Yin, S. Xin, Y. G. Guo, L. J. Wan, *Angew. Chemie - Int. Ed.* **2013**, *52*, 13186.

[34] A. Manthiram, Y. Fu, Y. S. Su, *Acc. Chem. Res.* **2013**, *46*, 1125.

[35] X. Ji, L. F. Nazar, *J. Mater. Chem.* **2010**, *20*, 9821.

[36] Y. Wang, X. Huang, S. Zhang, Y. Hou, *Small Methods* **2018**, *2*, 1.

[37] D. Aurbach, E. Pollak, R. Elazari, G. Salitra, C. S. Kelley, J. Affinito, *J. Electrochem. Soc.* **2009**, *156*, A694.

[38] S. S. Zhang, *J. Electrochem. Soc.* **2012**, *159*, A920.

[39] A. Rosenman, R. Elazari, G. Salitra, E. Markevich, D. Aurbach, A. Garsuch, *J. Electrochem. Soc.* **2015**, *162*, A470.

[40] S.-E. Cheon, K.-S. Ko, J.-H. Cho, S.-W. Kim, E.-Y. Chin, H.-T. Kim, *J. Electrochem. Soc.* **2003**, *150*, A796.

[41] S. Huang, Z. Wang, Y. Von Lim, Y. Wang, Y. Li, D. Zhang, H. Y. Yang, *Adv. Energy Mater.* **2021**, *11*, 1.

[42] E. Peled, A. Gorenshtein, M. Segal, Y. Sternberg, *J. Power Sources* **1989**, *26*, 269.

[43] M. Du, Q. Li, G. Zhang, F. Wang, H. Pang, *Energy Environ. Mater.* **2022**, *5*, 215.

[44] M. Zheng, Y. Chi, Q. Hu, H. Tang, X. Jiang, L. Zhang, S. Zhang, H. Pang, Q. Xu, *J. Mater. Chem. A* **2019**, *7*, 17204.

[45] J. Janek, W. G. Zeier, *Nat. Energy* **2016**, *1*, 1.

[46] G. Zhou, D. W. Wang, F. Li, P. X. Hou, L. Yin, C. Liu, G. Q. Lu, I. R. Gentle, H. M. Cheng, *Energy Environ. Sci.* **2012**, *5*, 8901.

[47] T. Xu, J. Song, M. L. Gordin, H. Sohn, Z. Yu, S. Chen, D. Wang, *ACS Appl. Mater. Interfaces* **2013**, *5*, 11355.

[48] J. Z. Wang, L. Lu, M. Choucair, J. A. Stride, X. Xu, H. K. Liu, *J. Power Sources* **2011**, *196*, 7030.

[49] H. Sun, G. L. Xu, Y. F. Xu, S. G. Sun, X. Zhang, Y. Qiu, S. Yang, *Nano Res.* **2012**, *5*, 726.

[50] N. Li, M. Zheng, H. Lu, Z. Hu, C. Shen, X. Chang, G. Ji, J. Cao, Y. Shi, *Chem. Commun.* **2012**, *48*, 4106.

[51] C. Hu, H. Chen, Y. Shen, D. Lu, Y. Zhao, A. H. Lu, X. Wu, W. Lu, L. Chen, *Nat. Commun.* **2017**, *8*, 1.

[52] J. Wang, S. Y. Chew, Z. W. Zhao, S. Ashraf, D. Wexler, J. Chen, S. H. Ng, S. L. Chou, H. K. Liu, *Carbon N. Y.* **2008**, *46*, 229.

[53] X. Ji, K. T. Lee, L. F. Nazar, *Nat. Mater.* **2009**, *8*, 500.

[54] J. Schuster, G. He, B. Mandlmeier, T. Yim, K. T. Lee, T. Bein, L. F. Nazar, *Angew. Chemie - Int. Ed.* **2012**, *51*, 3591.

[55] N. Jayaprakash, J. Shen, S. S. Moganty, A. Corona, L. A. Archer, *Angew. Chemie* **2011**, *123*, 6026.

[56] P. T. Dirlam, R. S. Glass, K. Char, J. Pyun, *J. Polym. Sci. Part A Polym. Chem.* **2017**, *55*, 1635.

[57] S. Komaba, N. Yabuuchi, T. Ozeki, Z. J. Han, K. Shimomura, H. Yui, Y. Katayama, T. Miura, *J. Phys. Chem. C* **2012**, *116*, 1380.

[58] W. Chen, T. Lei, T. Qian, W. Lv, W. He, C. Wu, X. Liu, J. Liu, B. Chen, C. Yan, J. Xiong, *Adv. Energy Mater.* **2018**, *8*, 1.

[59] D. B. Babu, K. Giribabu, K. Ramesha, *ACS Appl. Mater. Interfaces* **2018**, *10*, 19721.

[60] X. Liu, J. Q. Huang, Q. Zhang, L. Mai, *Adv. Mater.* **2017**, *29*, DOI 10.1002/adma.201601759.

[61] T. Z. Hou, X. Chen, H. J. Peng, J. Q. Huang, B. Q. Li, Q. Zhang, B. Li, *Small* **2016**, *12*, 3283.

[62] H. Yuan, W. Zhang, J. guo Wang, G. Zhou, Z. Zhuang, J. Luo, H. Huang, Y. Gan, C. Liang, Y. Xia, J. Zhang, X. Tao, *Energy Storage Mater.* **2018**, *10*, 1.

[63] H. J. Peng, T. Z. Hou, Q. Zhang, J. Q. Huang, X. B. Cheng, M. Q. Guo, Z. Yuan, L. Y. He, F. Wei, *Adv. Mater. Interfaces* **2014**, *1*, 1400227.

[64] F. Wu, J. Qian, W. Wu, Y. Ye, Z. Sun, B. Xu, X. Yang, Y. Xu, J. Zhang, R. Chen, *Nano Res.* **2017**, *10*, 426.

[65] L. Du, X. Cheng, F. Gao, Y. Li, Y. Bu, Z. Zhang, Q. Wu, L. Yang, X. Wang, Z. Hu, *Chem. Commun.* **2019**, *55*, 6365.

[66] X. Li, X. Li, M. N. Banis, B. Wang, A. Lushington, X. Cui, R. Li, T. K. Sham, X. Sun, *J. Mater. Chem. A* **2014**, *2*, 12866.

[67] D. Wu, J. Liu, J. Chen, H. Li, R. Cao, W. Zhang, Z. Gao, K. Jiang, *J. Mater. Chem. A* **2021**, *9*, 5497.

[68] S. Evers, T. Yim, L. F. Nazar, *J. Phys. Chem. C* **2012**, *116*, 19653.

[69] S. Rehman, S. Guo, Y. Hou, *Adv. Mater.* **2016**, *28*, 3167.

[70] D. Liu, C. Zhang, G. Zhou, W. Lv, G. Ling, L. Zhi, Q. H. Yang, *Adv. Sci.* **2018**, *5*, DOI 10.1002/advs.201700270.

[71] G. Zhou, H. Tian, Y. Jin, X. Tao, B. Liu, R. Zhang, Z. W. Seh, D. Zhuo, Y. Liu, J. Sun, J. Zhao, C. Zu, D. S. Wu, Q. Zhang, Y. Cui, *Proc. Natl. Acad. Sci. U. S. A.* **2017**, *114*, 840.

[72] W. G. Lim, S. Kim, C. Jo, J. Lee, *Angew. Chemie - Int. Ed.* **2019**, *58*, 18746.

[73] J. Liang, Y. Jiao, M. Jaroniec, S. Z. Qiao, *Angew. Chemie* **2012**, *124*, 11664.

[74] F. Ma, J. Liang, T. Wang, X. Chen, Y. Fan, B. Hultman, H. Xie, J. Han, G. Wu, Q. Li, *Nanoscale* **2018**, *10*, 5634.

[75] D. W. Wang, Q. Zeng, G. Zhou, L. Yin, F. Li, H. M. Cheng, I. R. Gentle, G. Q. M. Lu, *J. Mater. Chem. A* **2013**, *1*, 9382.

[76] W. J. Chung, J. J. Griebel, E. T. Kim, H. Yoon, A. G. Simmonds, H. J. Ji, P. T. Dirlam, R. S. Glass, J. J. Wie, N. A. Nguyen, B. W. Guralnick, J. Park, Á. Somogyi, P. Theato, M. E. Mackay, Y. E. Sung, K. Char, J. Pyun, *Nat. Chem.* **2013**, *5*, 518.

[77] Y. Xu, Y. Wen, Y. Zhu, K. Gaskell, K. A. Cychosz, B. Eichhorn, K. Xu, C. Wang, *Adv. Funct. Mater.* **2015**, *25*, 4312.

[78] J. Wang, J. Yang, J. Xie, xu naixin, *Adv. Mater.* **2002**, *050*, 963.

[79] X. G. Yu, J. Y. Xie, J. Yang, H. jiang Huang, K. Wang, Z. S. Wen, *J. Electroanal. Chem.* **2004**, *573*, 121.

[80] H. Li, H. Yang, X. Ai, *Adv. Mater.* **2023**, *2305038*, 1.

[81] Z. X. Chen, M. Zhao, L. P. Hou, X. Q. Zhang, B. Q. Li, J. Q. Huang, *Adv. Mater.* **2022**, *34*, 1.

[82] M. Zhao, B. Q. Li, H. J. Peng, H. Yuan, J. Y. Wei, J. Q. Huang, *Angew. Chemie - Int. Ed.* **2020**, *59*, 12636.

[83] L. Shi, S. M. Bak, Z. Shadike, C. Wang, C. Niu, P. Northrup, H. Lee, A. Y. Baranovskiy, C. S. Anderson, J. Qin, S. Feng, X. Ren, D. Liu, X. Q. Yang, F. Gao, D. Lu, J. Xiao, J.

Liu, *Energy Environ. Sci.* **2020**, *13*, 3620.

[84] R. Fang, S. Zhao, P. Hou, M. Cheng, S. Wang, H. M. Cheng, C. Liu, F. Li, *Adv. Mater.* **2016**, *28*, 3374.

[85] X. B. Cheng, C. Yan, J. Q. Huang, P. Li, L. Zhu, L. Zhao, Y. Zhang, W. Zhu, S. T. Yang, Q. Zhang, *Energy Storage Mater.* **2017**, *6*, 18.

[86] N. Wang, X. Zhang, Z. Ju, X. Yu, Y. Wang, Y. Du, Z. Bai, S. Dou, G. Yu, *Nat. Commun.* **2021**, *12*, 4519.

[87] Y. Ye, F. Wu, Y. Liu, T. Zhao, J. Qian, Y. Xing, W. Li, J. Huang, L. Li, Q. Huang, X. Bai, R. Chen, *Adv. Mater.* **2017**, *29*, DOI 10.1002/adma.201700598.

[88] C. Zhao, G. L. Xu, Z. Yu, L. Zhang, I. Hwang, Y. X. Mo, Y. Ren, L. Cheng, C. J. Sun, Y. Ren, X. Zuo, J. T. Li, S. G. Sun, K. Amine, T. Zhao, *Nat. Nanotechnol.* **2021**, *16*, 166.

[89] K. Zhu, C. Wang, Z. Chi, F. Ke, Y. Yang, A. Wang, W. Wang, L. Miao, *Front. Energy Res.* **2019**, *7*, 1.

[90] S. Dai, Y. Feng, P. Wang, H. Wang, H. Liang, R. Wang, V. Linkov, S. Ji, **2019**, *321*, 134678.

[91] L. Zhou, D. L. Danilov, R. A. Eichel, P. H. L. Notten, *Adv. Energy Mater.* **2021**, *11*, 2001304.

[92] J. Zhang, Y. Cai, Q. Zhong, D. Lai, J. Yao, *Nanoscale* **2015**, *7*, 17791.

[93] Z. Zhao, W. Yin, H. Li, Y. Jiao, D. Lei, Y. Li, J. Guo, W. Bai, M. Xiang, *Microporous Mesoporous Mater.* **2022**, *337*, 111946.

[94] C.-C. Wu, S.-H. Chung, *J. Power Sources* **2023**, *566*, 232944.

[95] B. Zhang, X. Qin, G. R. Li, X. P. Gao, *Energy Environ. Sci.* **2010**, *3*, 1531.

[96] X. Liang, Z. Wen, Y. Liu, H. Zhang, L. Huang, J. Jin, *J. Power Sources* **2011**, *196*, 3655.

[97] F. Sun, J. Wang, H. Chen, W. Li, W. Qiao, D. Long, L. Ling, *ACS Appl. Mater. Interfaces* **2013**, *5*, 5630.

[98] Y. J. Yen, T. H. Chen, Y. T. Wang, A. Robles, M. Đerić, O. Miljanić, W. Kaveevivitchai, S. H. Chung, *J. Power Sources* **2023**, *565*, 232891.

[99] W. Sun, S. Liu, Y. Li, D. Wang, Q. Guo, X. Hong, K. Xie, Z. Ma, C. Zheng, S. Xiong, *Adv. Funct. Mater.* **2022**, *32*, 1.

[100] J. Song, T. Xu, M. L. Gordin, P. Zhu, D. Lv, Y. B. Jiang, Y. Chen, Y. Duan, D. Wang, *Adv. Funct. Mater.* **2014**, *24*, 1243.

[101] J. Guo, Z. Yang, Y. Yu, H. D. Abruña, L. A. Archer, *J. Am. Chem. Soc.* **2013**, *135*, 763.

[102] H. Yuan, T. Liu, Y. Liu, J. Nai, Y. Wang, W. Zhang, X. Tao, *Chem. Sci.* **2019**, *10*, 7484.

[103] F. Chen, J. Yang, T. Bai, B. Long, X. Zhou, *Electrochim. Acta* **2016**, *192*, 99.

[104] H. Yao, G. Zheng, W. Li, M. T. McDowell, Z. Seh, N. Liu, Z. Lu, Y. Cui, *Nano Lett.* **2013**, *13*, 3385.

[105] S. H. Chung, C. H. Chang, A. Manthiram, *ACS Nano* **2016**, *10*, 10462.

[106] X. Tao, J. Zhang, Y. Xia, H. Huang, J. Du, H. Xiao, W. Zhang, Y. Gan, *J. Mater. Chem. A* **2014**, *2*, 2290.

[107] D. Qiu, X. Zhang, D. Zheng, W. Ji, T. Ding, H. Qu, M. Liu, D. Qu, *ACS Appl. Mater. Interfaces* **2023**, *15*, 36250.

[108] M. Xiang, Y. Wang, J. Wu, Y. Guo, H. Wu, Y. Zhang, H. Liu, *Electrochim. Acta* **2017**, *227*, 7.

[109] M. Kopeć, M. Lamson, R. Yuan, C. Tang, M. Kruk, M. Zhong, K. Matyjaszewski, T. Kowalewski, *Prog. Polym. Sci.* **2019**, *92*, 89.

[110] S. Rastogi, B. Kandasubramanian, *J. Text. Inst.* **2020**, *111*, 1794.

[111] M. Thommes, K. Kaneko, A. V. Neimark, J. P. Olivier, F. Rodriguez-Reinoso, J. Rouquerol, K. S. W. Sing, *Pure Appl. Chem.* **2015**, *87*, 1051.

[112] S. Brunauer, P. H. Emmett, E. Teller, *J. Am. Chem. Soc.* **1938**, *60*, 309.

[113] F. A. Stevie, C. L. Donley, *J. Vac. Sci. Technol. A Vacuum, Surfaces, Film.* **2020**, *38*, DOI 10.1116/6.0000412.

[114] A. M. Venezia, *Catal. Today* **2003**, *77*, 359.

[115] A. Ali, Y. W. Chiang, R. M. Santos, *Minerals* **2022**, *12*, DOI 10.3390/min12020205.

[116] C. C. Zhang, S. Hartlaub, I. Petrovic, B. Yilmaz, *ACS Omega* **2022**, *7*, 2565.

[117] N. Elgrishi, K. J. Rountree, B. D. McCarthy, E. S. Rountree, T. T. Eisenhart, J. L. Dempsey, *J. Chem. Educ.* **2018**, *95*, 197.

[118] L. Yuan, X. Qiu, L. Chen, W. Zhu, *J. Power Sources* **2009**, *189*, 127.

[119] N. Shimodaira, A. Masui, *J. Appl. Phys.* **2002**, *92*, 902.

[120] M. Xie, J. Yang, J. Liang, X. Guo, W. Ding, J. Hu, Y. Xie, M. Yin, Z. Zhang, *J. Energy Chem.* **2020**, *49*, 327.

[121] Y. Xu, C. Zhang, M. Zhou, Q. Fu, C. Zhao, M. Wu, Y. Lei, *Nat. Commun.* **2018**, *9*, 1720.

[122] S. Zhang, S. Tsuzuki, K. Ueno, K. Dokko, M. Watanabe, *Angew. Chemie - Int. Ed.* **2015**, *54*, 1302.

[123] S. S. Zhang, *Inorg. Chem. Front.* **2015**, *2*, 1059.

[124] Y. X. Wang, L. Huang, L. C. Sun, S. Y. Xie, G. L. Xu, S. R. Chen, Y. F. Xu, J. T. Li, S. L. Chou, S. X. Dou, S. G. Sun, *J. Mater. Chem.* **2012**, *22*, 4744.

[125] S. Xin, Y. You, H. Q. Li, W. Zhou, Y. Li, L. Xue, H. P. Cong, *ACS Appl. Mater. Interfaces* **2016**, *8*, 33704.

[126] Q. Tang, Z. Shan, L. Wang, X. Qin, K. Zhu, J. Tian, X. Liu, *J. Power Sources* **2014**, *246*, 253.

[127] S. Dierickx, A. Weber, E. Ivers-Tiffée, *Electrochim. Acta* **2020**, *355*, DOI 10.1016/j.electacta.2020.136764.

[128] M. A. Danzer, *Batteries* **2019**, *5*, 1.

[129] D. S. Wu, F. Shi, G. Zhou, C. Zu, C. Liu, K. Liu, Y. Liu, J. Wang, Y. Peng, Y. Cui, *Energy Storage Mater.* **2018**, *13*, 241.

[130] S. Wang, Z. Wang, F. Chen, B. Peng, J. Xu, J. Li, Y. Lv, Q. Kang, A. Xia, L. Ma, *Nano Res.* **2023**, *16*, 4438.

[131] Z. Yu, Y. Shao, L. Ma, C. Liu, C. Gu, J. Liu, P. He, M. Li, Z. Nie, Z. Peng, Y. Shao, *Adv. Mater.* **2022**, *34*, 1.

[132] Q. Pang, D. Kundu, M. Cuisinier, L. F. Nazar, *Nat. Commun.* **2014**, *5*, DOI 10.1038/ncomms5759.

[133] J. Wu, T. Ye, Y. Wang, P. Yang, Q. Wang, W. Kuang, X. Chen, G. Duan, L. Yu, Z. Jin, J. Qin, Y. Lei, *ACS Nano* **2022**, *16*, 15734.

[134] H. Chen, Z. Wu, M. Zheng, T. Liu, C. Yan, J. Lu, S. Zhang, *Mater. Today* **2022**, *52*, 364.

[135] D. Zheng, X. Zhang, J. Wang, D. Qu, X. Yang, D. Qu, *J. Power Sources* **2016**, *301*, 312.

[136] D. Zheng, D. Liu, J. B. Harris, T. Ding, J. Si, S. Andrew, D. Qu, X. Q. Yang, D. Qu, *ACS Appl. Mater. Interfaces* **2017**, *9*, 4326.

[137] D. Zheng, X. Zhang, C. Li, M. E. McKinnon, R. G. Sadok, D. Qu, X. Yu, H.-S. Lee, X.-Q. Yang, D. Qu, *J. Electrochem. Soc.* **2015**, *162*, A203.

[138] M. U. M. Patel, R. Demir-Cakan, M. Morcrette, J. M. Tarascon, M. Gaberscek, R. Dominko, *ChemSusChem* **2013**, *6*, 1177.

[139] E. Horváth, Csaba, *High-Performance Liquid Chromatography: Advances and Perspectives*, **2013**.

[140] Y. Diao, K. Xie, S. Xiong, X. Hong, *J. Electrochem. Soc.* **2012**, *159*, A421.

[141] D. Zheng, D. Qu, X. Q. Yang, X. Yu, H. S. Lee, D. Qu, *Adv. Energy Mater.* **2015**, *5*, 1401888.

[142] D. Zheng, X. Q. Yang, D. Qu, *ChemSusChem* **2016**, *9*, 2348.

[143] Y. J. Choi, B. S. Jung, D. J. Lee, J. H. Jeong, K. W. Kim, H. J. Ahn, K. K. Cho, H. B. Gu, *Phys. Scr. T* **2007**, *T129*, 62.

[144] X. Tao, J. Wan, C. Liu, H. Wang, H. Yao, G. Zheng, Z. W. Seh, Q. Cai, W. Li, G. Zhou, C. Zu, Y. Cui, *Nat. Commun.* **2016**, *7*, DOI 10.1038/ncomms11203.

[145] Z. Zeng, W. Li, X. Chen, N. Zhang, H. Qi, X. Liu, *ACS Sustain. Chem. Eng.* **2020**, *8*, 3261.

[146] F. Sun, J. Wang, D. Long, W. Qiao, L. Ling, C. Lv, R. Cai, *J. Mater. Chem. A* **2013**, *1*, 13283.

[147] K. Avetisyan, I. Zweig, G. W. Luther, A. Kamyshny, *Geochim. Cosmochim. Acta* **2021**, *313*, 21.

[148] N. Ominde, N. Bartlett, X. Q. Yang, D. Qu, *J. Power Sources* **2010**, *195*, 3984.

[149] Z. Deng, Z. Zhang, Y. Lai, J. Liu, J. Li, Y. Liu, *J. Electrochem. Soc.* **2013**, *160*, A553.

[150] D. Qu, *Electrochem. commun.* **2006**, *8*, 1527.

[151] C. Tran, J. Kafle, X. Q. Yang, D. Qu, *Carbon N. Y.* **2011**, *49*, 1266.

[152] S. S. Zhang, *Energies* **2012**, *5*, 5190.

[153] L. F. Nazar, M. Cuisinier, Q. Pang, *MRS Bull.* **2014**, *39*, 436.

[154] W. Ren, W. Ma, S. Zhang, B. Tang, *Energy Storage Mater.* **2019**, *23*, 707.

[155] P. R. Chinnam, L. Xu, L. Cai, N. L. Cordes, S. Kim, C. M. Efaw, D. J. Murray, E. J. Dufek, H. Xu, B. Li, *Adv. Energy Mater.* **2022**, *12*, 1.

[156] S. Das, M. S. A. Bhuyan, K. N. Gupta, O. Okpowe, A. Choi, J. Sweeny, D. Olawale, V. G. Pol, *Small* **2024**, *2311850*, 1.

[157] M. Hagen, P. Fanz, J. Tübke, *J. Power Sources* **2014**, *264*, 30.

[158] Y. J. Yen, S. H. Chung, *Chem. Commun.* **2021**, *57*, 2009.

[159] O. Salihoglu, R. Demir-Cakan, *J. Electrochem. Soc.* **2017**, *164*, A2948.

[160] L. Qie, C. Zu, A. Manthiram, *Adv. Energy Mater.* **2016**, *6*, 1.